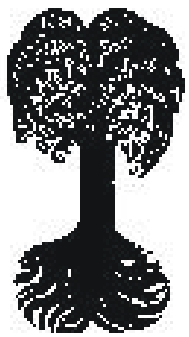




EBERHARD KARLS
UNIVERSITÄT
TÜBINGEN



Zentrum für Angewandte Geowissenschaften (ZAG)

**TÜBINGER
GEOWISSENSCHAFTLICHE
ARBEITEN (TGA)**

Reihe C: Hydro-, Ingenieur- und Umweltgeologie

Schriftleitung: P. Grathwohl, G. Teutsch

Anita Peter

**Assessing natural attenuation at
field scale by stochastic reactive
transport modelling**

TGA, C64, 2002

Assessing natural attenuation at field scale by stochastic reactive transport modelling

Anita Peter

Zentrum für Angewandte Geowissenschaften
Institut für Geologie und Paläontologie
Eberhard-Karls-Universität Tübingen
Sigwartstraße 10
72076 Tübingen
Germany

Herausgeber:
Institut für Geowissenschaften der Universität Tübingen
Sigwartstraße 10, D-72076 Tübingen

Schriftleitung der Reihe C:
Lehrstuhl für Angewandte Geologie
Prof. Dr. Peter Grathwohl & Prof. Dr. Georg Teutsch

Redaktion:
Dipl.-Geol. Björn Sack-Kühner

ISSN 0935-4948
ISSN 1610-4706 (Internet)

TGA	Reihe C	Nr. 64	101 S., 45 Abb., 16 Tab.	Tübingen, 2002
-----	---------	--------	--------------------------	----------------

Assessing natural attenuation at field scale by stochastic reactive transport modelling

Anita Peter¹

Former manufactured gas plants are often difficult to remediate by active *in situ* remediation strategies due to often numerous spilled source zones and due to the low solubility of tar oil constituents, that represent the dominant pollutants at these sites. Thus, natural attenuation might be an alternative remediation approach on condition that the processes contributing to natural attenuation at the specific site are identified and quantified.

Within this thesis, a combined integral measuring and modelling approach is presented and applied, to assess natural attenuation at the former gasworks site in Stuttgart, 'Testfeld Süd'. The approach copes with subsurface heterogeneity by two different means. The integral measuring approach provides mean concentrations and mass flow rates at control planes, that are obtained by enlarging the sample volume and thus constitute values integrated over the heterogeneous subsurface. Within the modelling approach, heterogeneity is accounted for stochastically by a Monte Carlo approach. To describe the heterogeneity at the 'Testfeld Süd', a geostatistical analysis of the categorical variable 'facies', that hydraulic and geochemical parameters are attributed to, was performed. Then, equally likely aquifer realizations were generated, that served as input for the subsequent flow and reactive transport modelling.

For the reactive transport modelling, two different model approaches were considered, the one-dimensional Lagrangian streamtube model SMART and the three-dimensional Eulerian transport model MT3D-IPD, that is based on MT3D. As SMART does not account for geochemical heterogeneity, its applicability was investigated by comparison to MT3D-IPD. It was shown, that SMART is a useful tool to predict the ensemble mean of plume migration, especially for transport distances larger than 2 to 3 correlation lengths of the facies distribution. For shorter transport distances, SMART revealed good results for longer travel times, i.e. after approximately 80 % of the breakthrough occurred.

SMART was then applied to simulate natural attenuation of acenaphthene and p-xylene at the 'Testfeld Süd' by the use of integrally measured mass flow rates at two control planes. For acenaphthene, the initial contaminant mass flow rate and the minimum contamination time were identified by inverse stochastic transport modelling. Furthermore, the dominant impact of kinetic sorption on the transport of acenaphthene was demonstrated. Although acenaphthene retards strongly at the 'Testfeld Süd', natural attenuation as a remediation alternative does not seem favourable, as degradation of acenaphthene does not occur in the absence of naphthalene. Transport and fate of p-xylene was simulated accounting for biodegradation and kinetic sorption. Biodegradation rates were inversely determined and it was found that a second-order decay best described the observed mass flow rate reduction at all control planes. Thus, the contributions of biodegradation and kinetic sorption could be quantified for p-xylene, showing that more than 99 % of the observed mass flow rate reduction is caused by biodegradation. Natural attenuation might thus be an alternative remediation approach for p-xylene.

Results of the combined integral measuring and modelling approach were compared to results obtained from an integrally applied compound-specific isotope analysis (CSIA). Therefore, two additional integral mass flow rate measurements were performed to determine both contaminant mass flow rates and mean isotope ratios at two control planes. Results of the integrally applied CSIA method by using the Rayleigh equation revealed that the complete mass flow rate reduction observed for o-xylene is due to biodegradation, which was confirmed by the stochastic transport modelling for o-xylene.

¹ Dissertation an der Geowissenschaftlichen Fakultät der Universität Tübingen
Anschrift der Autorin: Anita Peter, Galgenbergstraße 70, 72072 Tübingen

Reaktive stochastische Modellierung von Natural Attenuation im Feldmaßstab

Ehemalige Gaswerksgelände stellen häufig schwer zu sanierende Altlastenstandorte dar, da sie meist viele verstreute Schadensherde aufweisen und die dominierenden Teeröle von geringer Löslichkeit sind. Natural Attenuation könnte daher ein alternativer Sanierungsansatz an diesen Standorten sein, unter der Voraussetzung, dass die Prozesse, die zu Natural Attenuation beitragen, standortspezifisch identifiziert und quantifiziert werden können.

Im Rahmen dieser Arbeit wird ein kombinierter integraler Mess- und Modellieransatz vorgestellt und für die Quantifizierung von Natural Attenuation auf dem ehemaligen Gaswerksgelände 'Testfeld Süd', Stuttgart, angewendet. Beide Teile dieses Ansatzes überwinden das Problem der Heterogenität des Aquifers. Bei dem integralen Messansatz wird das Probenahmenvolumen vergrößert und somit über die Heterogenität integriert, so dass mittlere Konzentrationen und Massenflüsse an Kontrollebenen erhalten werden. Die integral ermittelten Massenflüsse dienen als Eingabe für die reaktive Transportmodellierung, die die Aquiferheterogenität stochastisch im Rahmen von Monte-Carlo-Simulationen berücksichtigt. Hierzu wurde die Heterogenität des 'Testfelds Süd' anhand einer geostatistischen Analyse von Faziestypen untersucht, denen hydraulische und geochemische Eigenschaften zugewiesen wurden. Mit der ermittelten räumlichen Korrelation sowie den Häufigkeiten der Faziestypen wurden gleichwahrscheinliche Aquiferrealisationen erzeugt, die als Grundlage für die folgenden Strömungs- und Transportberechnungen dienten.

Für die reaktive Transportmodellierung wurden zwei unterschiedliche Ansätze angewendet, zum einen das eindimensionale Lagrange'sche Stromröhrenmodell SMART und zum anderen das dreidimensionale Euler'sche Transportmodell MT3D-IPD, das auf MT3D basiert. Da geochemische Heterogenitäten in SMART nicht berücksichtigt werden können, wurde die Anwendbarkeit von SMART anhand eines Modellvergleichs mit MT3D-IPD untersucht. Es wurde gezeigt, dass SMART zur Simulation der mittleren Fahnenausbreitung eingesetzt werden kann, insbesondere für Distanzen, die größer sind als zwei bis drei Korrelationslängen der geochemischen Heterogenität. Für kürzere Transportstrecken zeigte SMART gute Ergebnisse für größere Zeiten, d. h. nachdem ein 80 %iger Durchbruch stattgefunden hat.

SMART konnte somit für die Modellierung von Natural Attenuation von Acenaphthen und p-Xylol im 'Testfeld Süd' unter Verwendung der integral gemessenen Massenflüsse an zwei Kontrollebenen angewendet werden. Der initiale Massenfluss sowie die Kontaminationszeit wurden für Acenaphthen invers im Rahmen der stochastischen Transportmodellierung ermittelt. Des Weiteren konnte der dominante Einfluss der kinetischen Sorption auf das Transportverhalten von Acenaphthen gezeigt werden. Obwohl Acenaphthen im 'Testfeld Süd' aufgrund der kinetischen Sorption stark retardiert, scheint Natural Attenuation keine sinnvolle Sanierungsstrategie zu sein, da Acenaphthen in der Abwesenheit von Naphthalin nicht abgebaut wird. Bei der Simulation des Transports von p-Xylol wurde neben kinetischer Sorption auch Bioabbau berücksichtigt. Bioabbauraten wurden invers ermittelt und es wurde gezeigt, dass ein Abbau zweiter Ordnung die beobachtete Massenflussabnahme an allen Kontrollebenen am besten beschreibt. Damit konnte der Anteil des biologischen Abbaus an der gemessenen Reduktion der Massenflüsse mit mehr als 99 % quantifiziert werden, während Sorption nur mit weniger als einem Prozent beiträgt. Im Hinblick auf o-Xylol könnte Natural Attenuation somit ein alternativer Sanierungsansatz für das 'Testfeld Süd' sein.

Die Ergebnisse des kombinierten integralen Mess- und Modellieransatzes wurden des Weiteren mit Ergebnissen aus Isotopenuntersuchungen verglichen, die erstmals in einem integralen Ansatz ermittelt wurden. Hierfür wurden zwei weitere Massenflussbestimmungen durchgeführt, bei denen sowohl Schadstoffmassenflüsse als auch mittlere Kohlenstoffisotopenwerte an zwei Kontrollebenen bestimmt wurden. Die Ergebnisse der Isotopenuntersuchungen unter Anwendung der Rayleigh-Beziehung ergaben, dass die komplette Massenflussabnahme von o-Xylol auf biologischen Abbau zurückzuführen ist. Dies wurde durch Transportsimulationen, die für o-Xylol in dem Teilbereich durchgeführt wurden, bestätigt.

Acknowledgements

Financial support for this work was provided by the Deutsche Forschungsgemeinschaft, Priority Program 546: “Geochemical processes with long-term effects in anthropogenically affected seepage- and groundwater”.

I would like to thank my supervisor Prof. Dr. Georg Teutsch for his continuous support and engagement and for the examination of this work. My special thanks go to Dr. Rudolf Liedl and Dr. Thomas Ptak for the numerous discussions, advices and ideas to support me.

I owe a lot to my colleagues and would like to thank Alexander Bockelmann, Sebastian Bauer, Matthias Piepenbrink, Rudi Jäger, Michael Finkel, Martin Herfort, Thomas Holder, Steffen Bold, Sybille Kleineidam, Hermann Rügner and Rainer Meckenstock for the many discussions and furthermore the complete Applied Geology group for the very agreeable atmosphere.

I appreciated very much the collaboration and interchange with Alfred Steinbach (University of Hamburg) during the planning, implementation and evaluation of the field work. Thanks a lot for reading and commenting the respective chapter of my work.

For the technical support in various respects special thanks deserve the technicians (Klaus Faiß, Wolfgang Kürner) for their important help during the field work, the laboratory crew (Renate Riehle, Renate Seelig, Anne Hartmann-Renz, Holger Martin) for analysing the groundwater samples and thanks a lot to the system administrator team (Guirong Zhu-Hiptmair, Thomas Kalbacher) for helping and keeping alive the computational facilities.

Furthermore, I would like to thank the Center for Computer Sciences of the University of Tübingen (ZDV), especially Fr. Schaarschmidt, for supporting the attempt to parallelize the program code and for providing valuable CPU time on the ZDV’s workstations.

Finally I thank Sebastian Bauer for reading and commenting my work and for the endless encouragement he offered me.

Contents

Symbols and Abbreviations	IV
1 Introduction	1
1.1 Motivation	1
1.2 Objectives	2
1.3 Structure of the thesis	3
2 Field Site 'Testfeld Süd'	5
2.1 Location and history	5
2.2 Geology and hydrogeology	5
2.3 Recent situation of contamination	7
3 Processes of Natural Attenuation	9
3.1 Fundamental principles	10
3.2 Hydrodynamic processes	10
3.3 Sorption of hydrocarbons	11
3.3.1 Equilibrium Sorption	11
3.3.2 Kinetic sorption	12
3.4 Biodegradation of hydrocarbons	13
3.4.1 Aerobic degradation of hydrocarbons	15
3.4.2 Anaerobic degradation of hydrocarbons	15
3.4.3 Methanogenesis	16
3.5 Lines of evidence	16
4 The integral measuring and modelling approach	17
4.1 The integral mass flow rate approach	17
4.2 Stochastic transport modelling using measured mass flow rates	19
4.2.1 Concepts of stochastic transport modelling	19
4.2.2 Determination of biodegradation rates by inverse stochastic transport modelling	21
5 Concepts for modelling Natural Attenuation at field scale	25
5.1 Description of hydraulic and geochemical heterogeneity: the facies approach	25
5.1.1 Background	25
5.1.2 Improved facies approach applied at the 'Testfeld Süd'	26
5.2 Eulerian model approach – MT3D-IPD	28
5.3 Lagrangian model approach - SMART	29

6	Geostatistical analysis at the 'Testfeld Süd'	33
6.1	Introduction	33
6.2	Variogram analysis	34
6.2.1	Development of the indicator database	34
6.2.2	Determination of experimental and theoretical variograms	35
6.3	Generation of aquifer realizations	37
6.4	Flow characterization of the selected realizations	39
6.5	Summary and conclusions	41
7	Comparing model approaches at field scale	43
7.1	Introduction	43
7.2	Two-dimensional case studies	44
7.2.1	Model results for homogeneous geochemical conditions	45
7.2.1.1	Homogeneous hydraulic conditions	45
7.2.1.2	Heterogeneous hydraulic conditions	45
7.2.2	Model results for heterogeneous geochemical conditions	47
7.3	Summary and outlook	54
8	Modelling natural attenuation at the 'Testfeld Süd'	57
8.1	Introduction	57
8.2	Modelling the fate of acenaphthene	57
8.2.1	Model domain and model set-up	58
8.2.2	Model results and discussion	59
8.3	Inverse determination of degradation rates of p-xylene	61
8.3.1	Model domain and model set-up	61
8.3.2	Model results and discussion	62
8.4	Summary and conclusions	64
9	Combination of the Compound-Specific Isotope Analysis with the Integral Mass Flow Rate Approach and comparison to the Integral Modelling Approach	67
9.1	Introduction	67
9.2	Combined integral mass flow rate measurements at the 'Testfeld Süd'	70
9.2.1	Location of pumping wells and pumping test set-up	70
9.2.2	Hydraulic results	70
9.2.3	Chemical results and plume composition	72
9.2.4	Carbon isotope results	74
9.2.5	Mass flow rate determination by analytical inversion	77
9.3	Quantification of biodegradation applying the modelling approach	82
9.3.1	Model domain and model set-up	82
9.3.2	Model results	83

9.4	Summary and conclusions	83
10	Summary and conclusions	87
References		91
Appendix		A1

Symbols and Abbreviations

Symbols

I/n_{fr}	Freundlich exponent	-
a	sill	-
a_0	nugget	-
A_{cp}	area of the control plane	L^2
b_i	radius of isochrone	L
B	aquifer thickness	L
C_{plume}	concentration in the plume	$M L^{-3}$
C_s	concentration in the solid phase	-
$C_{s, max}$	maximum sorbed concentration in the solid phase	-
C_w	concentration in the aqueous phase	$M L^{-3}$
$C_w [^{13}C]$	Concentration of ^{13}C of the specific compound concentration	$M [^{13}C] L^{-3}$
C_{well}	concentration in the well	$M L^{-3}$
d_s	solid density	$M L^{-3}$
\mathbf{D}	dispersion tensor	$L^2 T^{-1}$
D_a	apparent diffusion coefficient	$L^2 T^{-1}$
D_{aq}	aqueous diffusion coefficient	$L^2 T^{-1}$
D_e	effective diffusion coefficient	$L^2 T^{-1}$
\mathbf{e}_{cp}	unit vector normal to the control plane	-
err_k	relative sequential indicator simulation error for the facies k	-
f_{eq}	fraction of equilibrium sorption in comparison to kinetic sorption	-
$f(\mathbf{x}; z)$	probability density function of a random variable $Z(\mathbf{x})$	-
f_k	frequency of the facies k	-
f_k^*	simulated frequency of the facies k	-
$F(\mathbf{x}; z)$	cumulative probability distribution function of a random variable $Z(\mathbf{x})$	-
h	piezometric head	L
H	Heaviside function	-
$I(\mathbf{x}, k)$	indicator variable of the categorical random variable $Z(\mathbf{x})$ with k categories	-
j	index for lithological component	-
k	index for grain size class	-
K_d	distribution coefficient	$L^3 M^{-1}$
\mathbf{K}_f	tensor of hydraulic conductivity	$L T^{-1}$
K_{fr}	Freundlich coefficient	$(L^3 M^{-1})^{1/n_{fr}}$
K_L	Langmuir coefficient	$L^3 M^{-1}$
l	range	L
m	mass flux	$M T^{-1} L^{-2}$
M	mass flow rate	$M T^{-1}$
$\langle M \rangle$	ensemble averaged mass flow rate	$M T^{-1}$
M_{obs}	observed mass flow rate	$M T^{-1}$
$m_{n,t}$	n-th normalized temporal moment	T^n
$M_{n,t}$	n-th temporal moment	$T^n M L^{-3}$
n	total porosity	-
n_d	order of decay	-
n_e	transport effective porosity	-
$O(\mathbf{x}_{cp}, \lambda)$	objective function of the inverse problem	-

pdf-FD	probability density function of travel times obtained from upstream finite difference solver	-
pdf-PT	probability density function of travel times obtained from particle tracking algorithm	-
q	specific discharge vector	$L T^{-1}$
q_s	source/sink term in flow equation	T^{-1}
q_x	x -component of the specific discharge vector	$L T^{-1}$
Q	volumetric discharge in undisturbed aquifer	$L^3 T^{-1}$
Q_p	pumping rate	$L^3 T^{-1}$
r	particle radius	L
R	retardation factor	-
R_t^C	carbon isotope ratio at time t	-
R_{st}^C	carbon isotope ratio of standard	-
R_s	summarized sorption term in transport equation	$M L^{-3} T^{-1}$
S_s	specific storage coefficient	L^{-1}
t	time	T
$T_{0.5}$	half-life of a degradable compound	T
v_a	flow velocity vector	$L T^{-1}$
v_x	x -component of the flow velocity vector	$L T^{-1}$
<i>werr</i>	weighted sequential indicator simulation error	-
x	distance	L
$z(\mathbf{x})$	one realization of the random variable $Z(\mathbf{x})$	-
$Z(\mathbf{x})$	random variable	-
α^C	carbon fractionation factor defined by the Rayleigh equation	-
α_{mac}	macro-dispersivity	L
β	weight fraction of carbon of the total weight of a compound	-
δ_0	$\delta^{13}\text{C}$ value of initial, i.e. undegraded, substrate	\textperthousand
ε	intraparticle porosity	-
ε^C	carbon isotope enrichment factor	\textperthousand
$\gamma(\mathbf{h})$	semivariogram	-
φ	angle in spherical coordinate system	-
λ_{nd}	n_d^{th} -order degradation rate constant	$T^{-1} (L^3 M^{-1})_d^{n-1}$
$\mu(\mathbf{x})$	expected value of a random variable at the location \mathbf{x}	-
$\mu_{2,t}$	second central temporal moment	T^2
ρ	bulk density	$M L^{-3}$
σ	standard deviation	
τ	travel time of a conservative particle	T
τ_{lp}	tortuosity factor of the intraparticle pore	-
Γ	reaction function in SMART	-

Abbreviations of contaminants

1,2,3-TMB	1,2,3-Trimethylbenzene
1,2,4-TMB	1,2,4-Trimethylbenzene
1,3,5-TMB	1,3,5-Trimethylbenzene
1-Me-Nap	1-Methylnaphthalene
2-Me-Nap	2-Methylnaphthalene
Ace	Acenaphthene
Ant	Anthracene
Any	Acenaphthylene
B	Benzene
BaA	Benzo(a)anthracene
BaP	Benzo(a)pyrene

Bbf-BkF	Benzo(b)fluoranthene, Benzo(k)fluoranthene
BF	Benzofuran
BghiP	Benzo(g,h,i)perylene
BTEX	Generic for Benzene, Toluene, Ethylbenzene and Xylenes
Chr	Chrysene
DahA	Dibenzo(a,h)anthracene
Et-B	Ethylbenzene
Fln	Fluorene
Fth	Fluoranthene
Ina	Indane
Indeno	Indeno(1,2,3-cd)pyrene
Ine	Indene
iso-PB	Isopropylbenzene
MTBE	Methyl tert-Butyl Ether
m-X	meta-Xylene
Nap	Naphthalene
o-X	ortho-Xylene
PAH	Polycyclic Aromatic Hydrocarbons
PB	Propylbenzene
Phe	Phenanthrene
p-X	para-Xylene
Py	Pyrene
T	Toluene

Other abbreviations

BESSY	Batch-Experiment-Simulation-System
CSIA	Compound-Specific Isotope Analysis
EA	electron acceptor
ED	electron donor
MNA	Monitored Natural Attenuation
MT3D-IPD	Modular Transport model in 3 Dimensions with Intraparticle Diffusion module
NAPL	Non-aqueous Phase Liquid
SMART	Streamtube Model for Advection and Reactive Transport
US EPA	United States Environmental Protection Agency

1 Introduction

1.1 Motivation

Contamination of soil and groundwater by organic pollutants originating from industrial sites, former manufactured gas plants, landfills or tanks is a widespread problem in urban areas. Common active *in situ* remediation strategies, like pump-and-treat, air sparging and soil vapour extraction, that are applied to contaminated sites, often reveal a high ineffectiveness, as they cause very high costs due to long operation times and often do not achieve the remediation target. Especially former manufactured gas plants constitute difficult sites for remediation. The gasification of coal emerged in Germany during the second half of the 19th century and lasted until the seventies of the 20th century when natural gas replaced the manufactured town gas. Residual products of the gas production are ammonia liquors, ash, clinker and various types of coal tar (LfU, 1990; Zamfirescu, 2000). Typical constituents of coal tars, which represent a highly complex mixture of light, medium and heavy tar oils and pitch, are mono- and polycyclic aromatic hydrocarbons (BTEX and PAH), heterocyclic hydrocarbons and phenols (Pyka, 1994; Zamfirescu, 2000). Due to the low solubility and thus low mobility of coal tar constituents and due to often diffusely spilled source zones that evolved during the long production periods of typically 70-100 years, the aforementioned active remediation strategies often do not apply at these sites.

A cost effective and often more efficient alternative or additional remediation strategy to the mentioned technical remediation approaches is (monitored) natural attenuation. The United

States Environmental Protection Agency (US EPA) defines natural attenuation as “biodegradation, dispersion, dilution, sorption, volatilisation, and/or chemical and biochemical stabilisation of contaminants to effectively reduce contaminant toxicity, mobility, or volume to levels that are protective of human health and the ecosystem” (US EPA, 1999). Among these processes, biodegradation is the only process that in fact reduces the contaminant mass, whereas sorption only retards the transport of the pollutant and volatilisation transports the contaminant to another environmental compartment. Dispersion and dilution cause just a spread of the plume and thus a reduction of the contaminant concentration by enlarging the volume of water occupied by the contaminant. Several studies on plume length characteristics revealed, that natural attenuation is in fact able to stabilize and even reduce the migration of a contaminant plume (Schiedek et al., 1997; Wiedemeier et al., 1999; Rice et al., 1995). Thus, the United States implemented monitored natural attenuation (MNA) for the first time as a remediation strategy for the treatment of contaminated sites (Kremer, 1999; US EPA, 1999). The US EPA refers to MNA as “the reliance on natural attenuation processes (...) to achieve site-specific remediation objectives within a time frame that is reasonable compared to that offered by other more active methods”.

Also in Europe the discussion on natural attenuation and its use in practice as well as the implementation into the legislation as MNA has begun (e.g. NICOLE, 1998; NATO-CCMS, 1999). Although in Germany an implementation into law is not yet foreseeable (Szelinski, 1999; Thoenes, 1999), efforts are made to evolve

criterions to evaluate the effectiveness of MNA as a remediation alternative (Teutsch et al., 1997; Teutsch & Rügner, 1999; Teutsch et al., 2001; Track & Michels, 1999). The ongoing discussion points out, that the lack of a well founded understanding of natural attenuation processes at field scale constitutes one of the major impediments for an implementation of MNA into law. Because natural attenuation processes depend considerably on the hydrogeological, geochemical and microbial conditions at the site, a site specific quantification of natural attenuation processes at field scale is required, which constitutes a major challenge for ongoing research activities.

1.2 Objectives

The aim of this thesis is the quantification of natural attenuation processes at field scale by employing for the first time a combined integral measuring and modelling approach. This approach is applied to the former gasworks site 'Testfeld Süd' to assess the influence of different natural attenuation processes. It comprises two main steps:

- The determination of contaminant mass flow rates at several control planes downgradient of the source by integral pumping tests. This step is partially performed in collaboration with A. Bockelmann (Bockelmann, subm.).
- The identification of natural attenuation processes by a control plane based stochastic transport modelling approach, that uses the measured mass flow rates as input and conditioning data, respectively.

For the implementation of the latter step, special focus is turned to:

- The delineation of subsurface heterogeneity at the 'Testfeld Süd' by a geostatistical description of the facies types, which characterize hydraulic and geochemical properties. Generated aquifer

realizations constitute the basis for the following Monte Carlo simulations.

- The comparison of model approaches in order to investigate the applicability of the control plane based streamtube model SMART. The streamtube model SMART is a favourable tool to assess natural attenuation within the integral approach, as it simulates one-dimensional reactive transport based on control planes in accordance with the measuring approach. Possible limitations of this approach are identified by comparison to a fully three-dimensional reactive transport model tool based on MT3D.
- The application of the streamtube model SMART within a Monte Carlo approach to simulate the relevant natural attenuation processes at the 'Testfeld Süd'. The mathematical description of natural attenuation processes in the transport model is based on physical processes as far as possible, i.e. kinetic sorption is completely characterized by measured parameters, whereas biodegradation is inversely identified by the use of measured mass flow rates as input or conditioning data.

This integral measuring and modelling approach copes with subsurface heterogeneity in two ways. First, the integral measuring approach results in an integration of concentrations over the heterogeneity, i.e. a non-uniform concentration distribution is accounted for in the mass flow rate measurements without spatially resolving subsurface heterogeneity. Secondly, the uncertainty in model predictions due to imperfect information about subsurface heterogeneity is evaluated within the Monte Carlo approach which allows to assess the variance of the results caused by stochastically modelled aquifer heterogeneity.

Besides the quantification of natural attenuation by the combined integral measuring and modelling approach, a further aim of this thesis is to compare the obtained results to the compound-specific isotope analysis (CSIA), that is used to estimate biodegradation *in situ*. To increase the

reliability of the CSIA method, it is applied for the first time within an integral measuring approach. Thus, instead of estimating biodegradation in the field between two single wells, CSIA is used to estimate biodegradation between two control planes.

1.3 Structure of the thesis

This thesis is divided into two main parts. The first part includes the theoretical background of all methods applied in this thesis (Chapter 3 – Chapter 5), whereas the second part comprises the application of the developed combined measuring and modelling approach including all intermediate steps (Chapter 6 – Chapter 9).

Before addressing the theoretical background of natural attenuation, Chapter 2 provides a brief overview of the field site 'Testfeld Süd'. The hydrogeological situation and the contamination history is given as obtained in previous studies.

Chapter 3 elucidates the relevant natural attenuation processes that might occur at the 'Testfeld Süd', i.e. dispersion, sorption and biodegradation.

The theoretical background of the combined integral measuring and modelling approach is presented in Chapter 4. The theory of the quantitative evaluation of pumping tests to obtain contaminant mass flow rates is explained, followed by a section on the background of the applied inverse stochastic transport modelling concept, that uses measured mass flow rates as input and conditioning data.

Chapter 5 describes in detail the tools used to assess and simulate natural attenuation at field scale. This includes the facies approach to delineate subsurface heterogeneity and two transport modelling approaches. One is the expanded Eulerian transport model MT3D-IPD, that is used to investigate the applicability of the second model tool, the Lagrangian streamtube model SMART.

After these theoretical chapters, that provide the base for the following applications, Chapter 6 presents the geostatistical analysis of the facies identified at the 'Testfeld Süd'. It comprises the analysis of the spatial structure and the generation of equally likely aquifer realizations as well as their hydraulic characterization.

In Chapter 7 the comparison of the two transport model approaches, the Eulerian transport model MT3D-IPD and the Lagrangian streamtube model SMART, is performed for different scenarios.

After demonstrating the applicability of the streamtube model SMART, SMART is applied in Chapter 8 to simulate the transport of two compounds at the 'Testfeld Süd', acenaphthene and p-xylene. Thus, for these compounds natural attenuation processes are quantified.

Chapter 9 demonstrates the comparison of the integrally applied compound-specific isotope analysis with the combined measuring and modelling approach. Pumping tests performed for this purpose are presented and the evaluation and comparison of both methods described.

Summary and conclusions of the thesis are given in Chapter 10.

2 Field Site 'Testfeld Süd'

2.1 Location and history

The investigated field site is located in the densely populated Neckar valley in Stuttgart, Southwest Germany. From 1875 to 1969 it served as a gasworks site to produce town gas from coal, later on from heavy oil (Jungbauer + Partner, 1994; Herfort, 2000). During operation, the locations of the various factories involved in the town gas production changed, leading to widespread possible contaminant source zones (Jungbauer + Partner, 1994). During World War II the site was severely attacked and destroyed, which probably caused the main spill of tar oils and other organic by-products of gas production.

In the 1970s natural gas began to replace the produced town gas and from 1974 on, the gasworks site was only used for the storage and distribution of natural gas. In this context, a partially subsurface storage tank for liquid gas was constructed, that reaches the groundwater level. During the excavation, subsurface contamination with NAPLs was found. This lead to a series of risk assessment studies on the site (GLA, 1989, 1992, 1993; Jungbauer + Partner, 1994), in combination with research studies on the fate and transport of organic pollutants (Herfort et al., 1999; Herfort, 2000; Zamfirescu, 2000).

2.2 Geology and hydrogeology

The gasworks site is located in the quaternary Neckar valley, limited by triassic hills in the

West and the river Neckar in the East (Figure 2.1). The contaminated quaternary aquifer consists mainly of fluvial gravel and sand deposits with various embedded sand and silt lenses. This leads to a distinct heterogeneity with respect to hydraulic and geochemical properties. The average thickness of the gravel and sand deposits is 3 to 3.5 m, representing the main aquifer.

The gravel deposits are covered by 1 to 2 m of brown and loamy overbank deposits (Herfort, 2000) of low permeability, which cause confined conditions in the underlying aquifer. Above the alluvial loam, anthropogenic fill (e.g. demolition debris and war rubble) is found, which partially replaces the alluvial loam. In areas, where the alluvial loam is missing, unconfined groundwater conditions prevail.

The aquifer base is formed by the triassic formation „Upper Gipskeuper“, consisting of pelitic rock, marl and originally gypsum rocks (Utrecht, 1999). As the hydraulic gradient between the Gipskeuper and the quaternary aquifer is directed upwards, mineral groundwater emanates locally from the Gipskeuper into the quaternary aquifer (Utrecht, 1999; Utrecht & Harlacher, 1998). Groundwater flow and chemistry in the quaternary aquifer might be strongly affected in these zones.

Approximately 1 km downstream of the site, the mineral water originating from the Gipskeuper is pumped for medical and spa purpose. This situation intensifies the concern about the pollution on the former gasworks site.

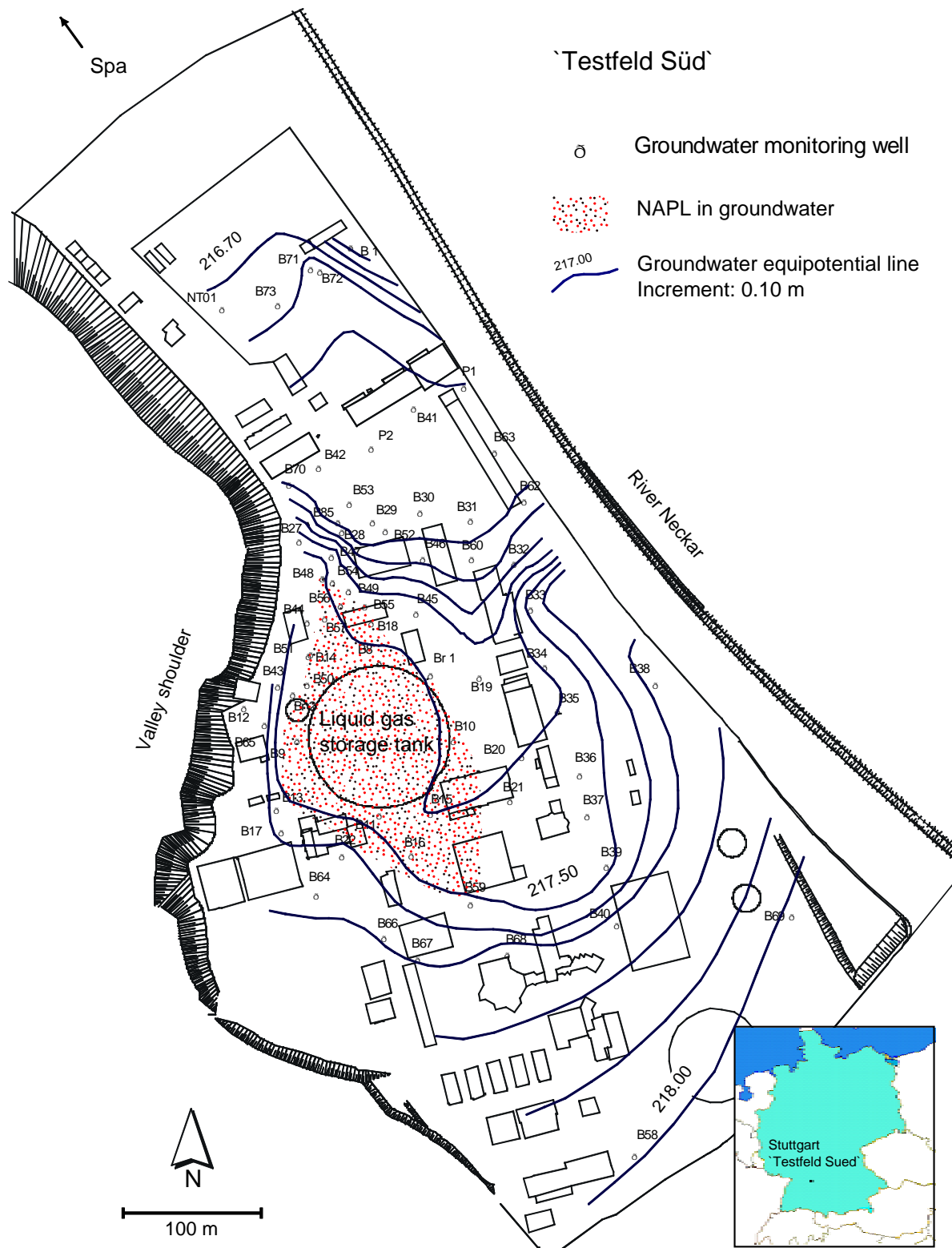


Figure 2.1 Map of the field site 'Testfeld Süd' with monitoring wells in the quaternary aquifer, presumed location of NAPL and observed groundwater heads from March 1999.

The hydraulic situation of the test site was investigated by means of head observations at 68 groundwater monitoring wells, pumping tests, slug tests and flowmeter tests as well as tracer tests (GLA, 1989, 1992; Bösel, 1999; Herfort, 2000). It can be summarised as follows:

- Groundwater flow is directed from South/Southeast to North/Northwest (Figure 2.1).
- Groundwater flow velocity ranges from 1 m d^{-1} to 4.2 m d^{-1} with a mean of 2 m d^{-1} . Transmissivities vary between $5.7 \cdot 10^{-5} \text{ m}^2 \text{ s}^{-1}$ and $3.4 \cdot 10^{-2} \text{ m}^2 \text{ s}^{-1}$.
- Due to the anthropogenic regulation of the river Neckar to a constant water level and due to widespread surface sealing of the test site, the groundwater conditions are almost steady state. Additionally, a leaking sewer drains a considerable amount of the groundwater flow (Holder & Teutsch, 2000), which contributes to the steady state conditions observed at the site. The maximum observed head difference at the site was 0.13 m within three years (Herfort, 2000).
- Groundwater flow is locally affected by mineral water ascending from the Gipskeuper, with poorly known locations and flow rates.

2.3 Recent situation of contamination

The various procedures of town gas production and the accompanying facilities on the site determined the contamination pattern observed today. High-molecular tar oil contaminants were found in the Southern part of the site, where the tar distillation and tar pits were located. North of the liquid gas storage tank (Figure 2.1), benzene distilling plants were situated, where today the highest BTEX concentrations are observed (Jungbauer + Partner, 1994; Zamfirescu, 2000).

Besides the production plants, which have been removed in the 1970s, when production of town gas was stopped, subsurface structures like pipelines might represent additional possible contaminant sources.

The main source zone is located between the former tar distilleries in the South (close to monitoring well B59 in Figure 2.1) and the benzene distilling plants (close to monitoring well B49), covering an area of approximately 20 000 m². In this zone, non-aqueous phase liquids (NAPLs) are found in most monitoring wells. Zamfirescu (2000) analysed the tar oil composition from different boreholes and performed leaching experiments to determine saturation concentrations from the NAPLs. The obtained saturation concentrations, which depend on the NAPL composition according to Raoult's Law, correspond well to the measured concentrations in groundwater determined by multilevel sampling.

The contaminants of greatest concern originating from NAPLs in the source area at the site are aliphatic hydrocarbons, monoaromatic and polycyclic aromatic hydrocarbons (BTEX and PAH) as well as phenols and heterocyclic hydrocarbons (Zamfirescu & Grathwohl, 1998). They constitute, according to the different source areas, a number of plumes of different composition. Due to insufficient information on the exact location of the sources, accurate mapping of the source zones and their corresponding plumes is not possible.

Depending on the saturation concentration, i.e. the tar oil composition, and the geochemical and microbiological properties of the compounds, the plume lengths are specific to the contaminant. Looking at BTEX compounds, highest concentrations near the source (B49) are determined with $1800 \mu\text{g L}^{-1}$ for benzene, $1400 \mu\text{g L}^{-1}$ for the xylenes and $2000 \mu\text{g L}^{-1}$ for indene (Schettler, 1998). Approximately 90 m further downstream (B42), only benzene shows significant concentrations of about $30 \mu\text{g L}^{-1}$

(Ries, 1998). This decrease in concentration might be attributed to biodegradation, as the BTEX compounds are not expected to sorb considerably (Schwarzenbach et al., 1993).

The contamination situation differs for the PAH compounds. Highest PAH concentrations in the northern source area were determined for naphthalene with approximately $2300 \mu\text{g L}^{-1}$, followed by acenaphthene with $750 \mu\text{g L}^{-1}$ (Schettler, 1998; Zamfirescu, 2000). The total concentration of the other 14 PAHs of the 16 US-EPA PAHs is 500 to $600 \mu\text{g L}^{-1}$. Their total concentration decreases within 90 m to a total concentration of less than $20 \mu\text{g L}^{-1}$ (Ries, 1998; Holder, 1999), which still is clearly above the drinking water limit of $0.2 \mu\text{g L}^{-1}$ for the sum of all PAHs. In contrast, naphthalene is found in a monitoring well 110 m downgradient with concentrations of $150 \mu\text{g L}^{-1}$ (Holder, 1999), whereas acenaphthene reveals significant concentrations of 150 to $300 \mu\text{g L}^{-1}$ and $180 \mu\text{g L}^{-1}$ at distances from the source of 100 and 240 m, respectively (Holder, 1999; Bockelmann et al., 2001).

3 Processes of Natural Attenuation

Contamination of aquifers by organic pollutants from sources like industrial sites, landfill sites or gas tanks is widely found in populated areas. Conventional cleanup strategies like pump-and-treat, source excavation, air sparging, soil vapour extraction and *in situ* bioremediation, which are frequently applied to these sites to reach a certain remediation target, often suffer from one or more of the following problems (e.g. Wiedemeier et al., 1999; Brady et al., 1998; Rice et al., 1995):

- The remediation target is not achieved within the planned or within an appropriate time frame.
- Operation times are often very long (tens of years) and thus cost intensive.
- Contaminants cleansed up are transformed into another state and/or transported to another environmental compartment, causing further environmental problems.

Various reasons exist for the inefficiency of the above mentioned remediation techniques:

- The contaminant source often cannot be located with accuracy.
- The processes controlling fate and transport of the contaminants in groundwater occur within large time scales (e.g. NAPL dissolution, sorption/desorption of hydrophobic contaminants).
- Most remediation approaches like air sparging, soil vapour extraction, *in situ* bioremediation and pump-and-treat achieve only small-scale effectiveness and do not cover the scale of the contamination. This effect is caused among other things by aquifer heterogeneity with respect to hydraulic and geochemical

properties and as well by low transverse dispersivities causing only a slight mixing of e.g. added electron acceptors with the contaminated groundwater.

A cost effective and sometimes more efficient alternative or additional remediation approach is monitored natural attenuation. Natural attenuation comprises the naturally occurring processes biodegradation, volatilisation, sorption, dispersion and dilution that reduce the contaminant concentrations at a specific site to an acceptable level.

Studies of plume lengths generally demonstrate the occurrence of natural attenuation (Schiedek et al., 1997; Wiedemeier et al., 1999; Rice et al., 1995). Schiedek et al. (1997) showed that BTEX and PAH plumes are usually less than 210 and 280 m long, respectively. Furthermore, Wiedemeier et al. (1999) collected data from several studies and showed that about 60 % of the analysed plumes were stable, one third was even shrinking and that only 8 % were growing. Thus, natural attenuation in fact may lead to an effective stabilization or even reduction of contaminant plumes, especially of BTEX and PAH plumes. However, natural attenuation processes considerably depend on the hydrogeological, geochemical and microbial conditions of the site. This requires a site specific quantification of the occurring natural attenuation processes.

The following sections provide an overview of the processes of natural attenuation controlling fate and transport of contaminants. As hydrocarbons are the dominating pollutants at the 'Testfeld Süd', the description of the sorption and degradation processes is restricted to them.

Because of the insignificant effect of volatilisation at the 'Testfeld Süd' (Weber et al., 1999) this process is not elucidated in this thesis.

3.1 Fundamental principles

Groundwater flow in a porous medium is described by Darcy's Law, that defines a proportionality between the vector of specific discharge \mathbf{q} and the gradient of piezometric heads ∇h :

$$\mathbf{q} = -\mathbf{K}_f \nabla h \quad (3.1)$$

where \mathbf{K}_f denotes the tensor of hydraulic conductivity. Dividing the specific discharge \mathbf{q} by the transport effective porosity n_e yields the flow velocity \mathbf{v}_a . Combining Darcy's Law with the equation of mass conservation results in the groundwater flow equation (e.g. Wang & Anderson, 1982):

$$S_s \frac{\partial h}{\partial t} = \nabla(\mathbf{K} \nabla h) + q_s \quad (3.2)$$

S_s is the specific storage coefficient and q_s is a source/sink term. The solution of the flow equation provides the velocity field, which is a prerequisite for describing the transport of solute compounds.

A general form of the transport equation (e.g. Wang & Anderson, 1982; Kinzelbach, 1992) is given by:

$$n_e \frac{\partial C_w}{\partial t} = \nabla(n_e \mathbf{D} \nabla C_w) - \nabla(\mathbf{v}_a n_e C_w) - R_s - \lambda_d n_e C_w^{n_d} \quad (3.3)$$

where C_w is the aqueous concentration of the solute compound and n_e is the transport effective porosity. The first term on the right hand side, with \mathbf{D} as dispersion tensor, represents the migration of a compound by local-scale dispersion. Advection (second term on the right hand side) and dispersion constitute the fundamental transport processes that all solute compounds are subject to (see Section 3.2). The term R_s represents loss or gain of solute

compounds by sorption and desorption processes (Section 3.3). The last term in equation (3.3) represents biodegradation (Section 3.4), following an n_d^{th} order decay with the degradation rate constant λ_d .

3.2 Hydrodynamic processes

When considering a conservative, i.e. non-sorbing and non-degrading compound, a decrease in concentration with increasing distance from the contaminant source is observed. Advection and dispersion cause a spreading and dilution of the plume, which results in diminished concentrations, but not in a diminished mass flux. In this sense, the hydrodynamic processes advection and dispersion do not act as intrinsic attenuation processes, although dispersion is listed in the US EPA definition of natural attenuation (see Chapter 1).

Spatial variability of advection caused by varying conductivities, porosities and/or aquifer geometries leads to a spreading of the plume (Figure 3.1 b). This is also referred to as large-scale dispersion or macro-dispersion (e.g. Dagan, 1988; Dagan, 1990; Cirpka & Kitanidis, 2000b). Besides the spreading of a plume, Kitanidis (1994) defines dilution as the increase of volume occupied by a compound, caused by local-scale dispersion (Figure 3.1 c). Considering a conservative compound, dilution is then the only process that allows mixing between two plumes, i.e. different flow paths. The local-scale dispersion is caused by varying pore size, tortuosity and varying local velocities in a pore due to friction in the pore throat as well as molecular diffusion (Wiedemeier et al., 1999). Cirpka & Kitanidis (2000b) show, that the second central moment of a locally measured breakthrough curve gives a measure for the dilution, i.e. local-scale dispersion, that is not affected by macro-dispersion.

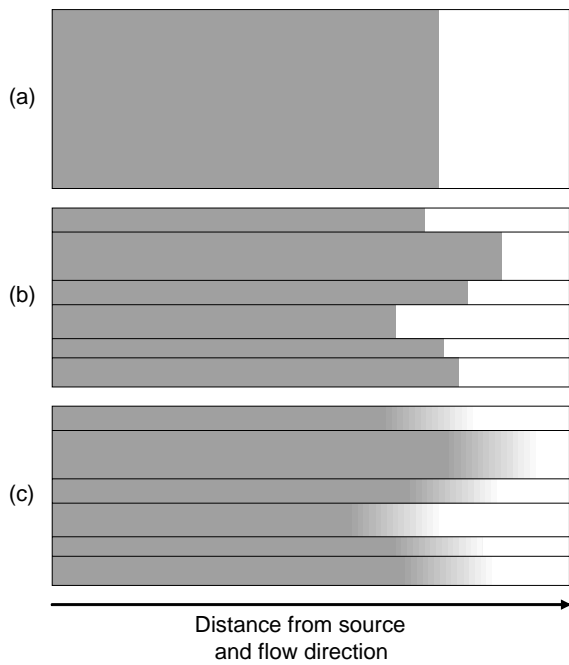


Figure 3.1 Schematic illustration of the effects of macro-dispersion and local-scale dispersion on plume migration. (a) advective transport in a hydraulically homogeneous aquifer. (b) advective transport in a hydraulically heterogeneous aquifer causing macro-dispersion. (c) advective-dispersive transport in a hydraulically heterogeneous aquifer (neglecting transverse dispersion).

As mentioned before, dilution and spreading do not contribute to a decrease of the contaminant mass flux. Assuming groundwater flow parallel to the x -axis and the contaminant source at $x = 0$, the mass flux m of a compound at any point of a control plane at a distance x_{cp} from the source is given by

$$\begin{aligned} m(x_{cp}, y, z) &= q_x(x_{cp}, y, z) \cdot C_w(x_{cp}, y, z) \\ &= v_x(x_{cp}, y, z) \cdot n_e \cdot C_w(x_{cp}, y, z) \end{aligned} \quad (3.4)$$

where q_x and v_x denote the component of the specific discharge and of the flow velocity in flow (x -) direction, respectively, and n_e is the effective porosity. The total contaminant mass flow rate M is then defined as

$$\begin{aligned} M(x_{cp}) &= \int \int m(x_{cp}, y, z) dy dz \\ &= \int \int C_w(x_{cp}, y, z) \cdot q_x(x_{cp}, y, z) dy dz \end{aligned} \quad (3.5)$$

3.3 Sorption of hydrocarbons

The saturated zone of an aquifer represents a two-phase system with the porous medium as solid phase and the flowing groundwater as aqueous phase. The interactions of the organic contaminant and these two phases depend on the physico-chemical properties of the compound, i.e. water solubility and vapour pressure, as well as on the geochemical characteristics of the aquifer material.

The dominant sorption mechanism of non-ionic organic compounds is the relatively weak “hydrophobic bonding” (Pignatello, 1989; Grathwohl, 1998). Dissolved hydrophobic organic compounds are surrounded by structured water. Bonding onto the solid phase requires less structured water, i.e. entropy increases. Sorbing on the solid phase is thus the thermodynamically favourable process.

The hydrophobic bonding of organic compounds depends directly on the content of soil organic matter (Karickhoff et al., 1979; Karickhoff, 1984; Grathwohl, 1990; Kleineidam et al., 1999; Karapanagioti et al., 2000). The relationship between the concentration of the sorbed compound in the organic matter and the concentration in the solute phase is referred to as partitioning. The partition coefficient is often expressed as a function of the content of organic carbon, which can be measured directly (e.g. Schwarzenbach et al., 1993; Grathwohl, 1998). Generally, the partition coefficient increases with decreasing solubility of the considered compound.

3.3.1 Equilibrium Sorption

The sorptive uptake of a compound by the solid phase depends on the contaminant concentration in the aqueous phase. In the simplest case, the relationship between sorbed and solute concentration, the so-called isotherm, is linear (Figure 3.2):

$$C_s = K_d \cdot C_w \quad (3.6)$$

where C_s and K_d are the concentration in the solid phase and the distribution coefficient, respectively. However, often a decrease in the sorptive uptake with increasing solute concentrations is observed. Various non-linear isotherm models have been established (Figure 3.2), like the Freundlich isotherm (Schwarzenbach et al., 1993):

$$C_s = K_{fr} \cdot C_w^{\frac{1}{n_{fr}}} \quad (3.7)$$

or the Langmuir isotherm:

$$C_s = \frac{K_L \cdot C_{s,max} \cdot C_w}{1 + K_L \cdot C_w} \quad (3.8)$$

where K_{fr} and $1/n_{fr}$ denote the Freundlich coefficient and Freundlich exponent, respectively. Correspondingly, K_L is the Langmuir coefficient and $C_{s,max}$ the maximum sorbed concentration in the solid phase.

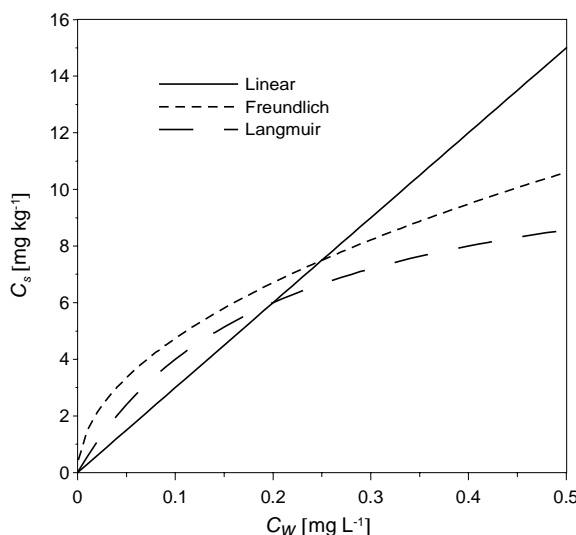


Figure 3.2 Examples of different sorption isotherm models. (Linear: $K_d=30 \text{ L kg}^{-1}$; Freundlich: $K_{fr}=15 (\text{L kg}^{-1})^{0.5}$ and $1/n_{fr}=0.5$; Langmuir: $K_L=5 \text{ L kg}^{-1}$ and $C_{s,max}=12 \text{ mg kg}^{-1}$).

All isotherm models assume an instantaneous sorptive uptake of the solvent by the sorbent. Therefore, the solute concentration C_w in equations (3.6) to (3.8) is assumed to be in equilibrium with the sorbed concentration in the solid phase.

As a consequence, the retardation factor R does not explicitly depend on time and is given by (e.g. Zheng & Wang, 1998):

$$R = 1 + \frac{\rho}{n_e} \frac{\partial C_s}{\partial C_w} \quad (3.9)$$

with

$$\rho = (1-n) d_s \quad (3.10)$$

where ρ and d_s denote the bulk density and the density of the solid, respectively. n represents the total porosity. In the case of a linear isotherm, $\partial C_s / \partial C_w$ in equation (3.9) equals K_d . Assuming the non-linear Freundlich isotherm, R is given by:

$$R = 1 + \frac{\rho}{n_e} \cdot \frac{1}{n_{fr}} K_{fr} C_w^{\frac{1}{n_{fr}}-1} \quad (3.11)$$

3.3.2 Kinetic sorption

Depending on the properties of the organic contaminant and the aquifer material, it might take days to years until (de)sorption equilibrium between the aqueous and the solid phase is reached. Due to this effect, sorption might seem irreversible, caused by very slow kinetics of the entire desorption process.

Experiments by Wu & Gschwend (1986), as well as e.g. Ball & Roberts (1991) and Schüth & Grathwohl (1994) showed, that diffusive transport of the contaminant to the sorbing surfaces causes the observed sorption kinetics. As the majority of the sorbing surfaces is located in the intraparticle pore volume and not on the particle surface, diffusion depends on the particle size and the pore structure (Barber et al., 1992; Kleineidam et al., 1999). After diffusive transport into the intraparticle pore volume, sorption is considered to be fast (Pignatello, 1989).

The diffusion of solute compounds into intra-particle pores is mathematically described by Fick's Second Law (Grathwohl, 1998):

$$\frac{\partial C_w}{\partial t} = D_a \left[\frac{\partial^2 C_w}{\partial r^2} + \frac{2}{r} \frac{\partial C_w}{\partial r} \right] \quad (3.12)$$

where r denotes the radius of the idealized spherical particle and D_a the apparent diffusion coefficient. The apparent diffusion coefficient D_a takes into account the effect of an increased mass storage in the pore due to sorbing solvents. It is defined as (Grathwohl, 1998):

$$D_a = \frac{D_{aq}\varepsilon}{(\varepsilon + K_d\rho)\tau_{ip}} = \frac{D_e}{\alpha} \quad (3.13)$$

with

$$\alpha = \varepsilon + K_d\rho \quad (3.14)$$

and

$$D_e = \frac{D_{aq}\varepsilon}{\tau_{ip}} \quad (3.15)$$

where D_{aq} is the diffusion coefficient in water, ε the intraparticle porosity, ρ the bulk density and τ_{ip} the tortuosity of the intraparticle pore. As indicated in equation (3.13), D_a is also expressed as the ratio of the effective diffusion coefficient D_e and the sorption capacity α . In the case of non-linear sorption, K_d in equation (3.13) and (3.14) is replaced by the derivative of a non-linear isotherm and D_a becomes concentration dependent.

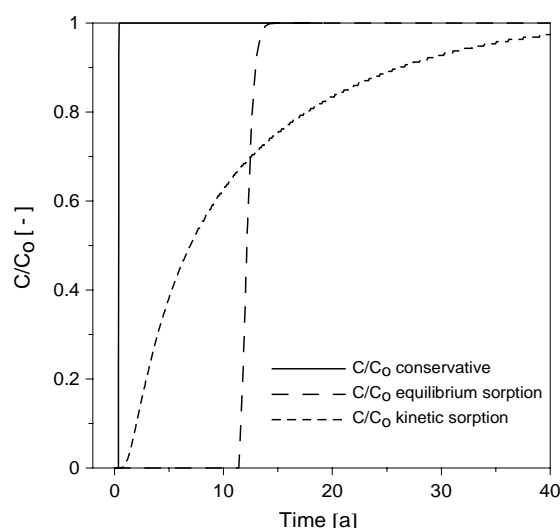


Figure 3.3 Modelled breakthrough curves for conservative transport, reactive transport assuming equilibrium sorption and reactive transport assuming kinetic sorption. C_0 denotes the input concentration.

Figure 3.3 compares breakthrough curves of a solute contaminant assuming (i) one-dimensional conservative transport (advection and dispersion), (ii) equilibrium sorption and (iii) kinetic sorption. The following general observations can be made:

- Both, equilibrium and kinetic sorption lead to a retarded contaminant arrival compared to conservative transport.
- First and mean arrival times are smaller in the case of kinetic sorption than in the case of equilibrium sorption (Figure 3.3). This is caused by a slower immobilisation of contaminants by kinetic sorption and thus a reduced retardation in the beginning. This temporary reduction of the retardation factor has also been observed in laboratory experiments (Schüth & Grathwohl, 1994; Rügner et al., 1999).
- The complete breakthrough of the contaminant takes longer assuming kinetic sorption than assuming equilibrium sorption.

These described characteristics of kinetic sorption might have a great impact on the dimensioning of remediation strategies and on risk assessment.

3.4 Biodegradation of hydrocarbons

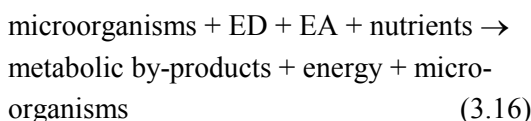
Biological degradation of organic compounds is the only of the above mentioned natural attenuation processes, that in fact eliminates contaminants. Several studies have demonstrated the evidence of biodegradation of hydrocarbons in laboratory experiments (e.g. Grbic-Galic & Vogel, 1987; Edwards & Grbic-Galic, 1992; Beller et al., 1992; Nielsen & Christensen, 1994; Kelly et al., 1996; Salanitro et al., 1997) as well as at field scale (e.g. Acton & Barker, 1992; Borden et al., 1997; Lahvis et al., 1999; Davis et al., 1999; Gieg et al., 1999). According to these authors biodegradability depends on several factors:

- the type of contaminant and its biochemical properties. It appears, that those compounds that have been available for microorganisms in large quantities and for the longest period of time are the most readily degradable. This explains e.g. the decreasing degradability from BTEX (naturally occurring hydrocarbon in crude oil) to chlorinated hydrocarbons (anthropogenically produced since approximately one hundred years) and further to MTBE (methyl tert-butyl ether; produced and distributed since approximately 15 years) (Wiedemeier et al., 1999; Salanitro et al., 1997).
- the bioavailability of the compound. Only dissolved and, to a limited extent, sorbed compounds are subject to biodegradation (Alexander, 1999; Wiedemeier et al., 1999)

- the geochemical conditions in the aquifer, like redox conditions, availability of electron acceptors and pH (Christensen et al., 2000; Alexander, 1999; Mormile et al., 1994; Edwards & Grbic-Galic, 1992; Beller et al., 1992).

Salanitro et al. (1997) showed, that biodegradation is less dependent on nutrient growth stimulants (like NH_3 and PO_4^{3-}), soil properties and microbial populations than on the aforementioned factors.

Biodegradation proceeds the following generalized reaction pathway, if the organic compound serves as primary growth substrate (Wiedemeier et al., 1999):



where ED and EA denote electron donor and electron acceptor, respectively.

Based on equation (3.16), three main types of degradation mechanisms can be distinguished (e.g. Alexander, 1999; Wiedemeier et al., 1999):

- biological reduction of organic compounds that act as EA, also referred to as halorespira-

tion. It is the main mechanism active in the degradation of chlorinated solvents.

- biological oxidation of organic compounds that serve as ED, which most of (not-chlorinated) hydrocarbons are subjected to, like mono-aromatic and aliphatic hydrocarbons.
- methanogenesis as a fermentation process, where organic compounds act as both EA and ED.

The simplest way to mathematically characterize biodegradation, is by describing the decrease of substrate, i.e. contaminant, by an n_d^{th} -order decay as already given in equation (3.3):

$$\frac{\partial C_w}{\partial t} = \lambda_{nd} C_w^{n_d} \quad (3.17)$$

where λ_{nd} denotes the degradation rate of n_d^{th} -order. Following a first order decay, C_w is given by:

$$C_w(t) = C_{w0} e^{-\lambda_1 t} \quad (3.18)$$

C_{w0} is the concentration at time $t=t_0$. The half-life $T_{0.5}$ is given by:

$$T_{0.5} = \frac{\ln 2}{\lambda_1} \quad (3.19)$$

and denotes the time, after which the concentration has decreased to half of the initial concentration.

The solution of equation (3.17) with $n_d=2$, i.e. for second order decay, is given by:

$$C_w(t) = \frac{C_{w0}}{C_{w0}\lambda_2 t + 1} \quad (3.20)$$

In this case, half-life at a given location is dependent on the initial concentration at the same location:

$$T_{0.5} = \frac{1}{C_{w0}\lambda_2} \quad (3.21)$$

As concentration decreases according to equation (3.20) along a considered flow path in x -direction, the half-life along the flow path increases linearly:

$$T_{0.5}(x) = \frac{x}{v_x} + \frac{1}{C_{w0}\lambda_2} \quad (3.22)$$

where v_x denotes the flow velocity in x -direction.

Other mathematical models exist to describe biodegradation kinetics. One of the most used models besides first-order decay is the Monod model that accounts for growth of the microbial populations (e.g. Alexander, 1999). However, this more sophisticated way of describing biodegradation suffers from the larger number of parameters needed, which cannot be determined directly by laboratory experiments and thus have to be determined by fitting model results to experimental data (Schirmer et al., 1999).

In the following three sub-chapters, biological oxidation of hydrocarbons under aerobic (3.4.1) and anaerobic conditions (3.4.2) and the process of methanogenesis (3.4.3) are elucidated. As chlorinated hydrocarbons do not occur in the test site considered, the interested reader is referred to the literature with respect to the process of halorespiration (Wiedemeier et al., 1999; Alexander, 1999).

3.4.1 Aerobic degradation of hydrocarbons

During aerobic degradation, microorganisms use free dissolved oxygen as electron acceptor for the pathway described in equation (3.16). Studies have shown, that almost all petroleum hydrocarbons biodegrade under aerobic conditions (e.g. Alvarez & Vogel, 1991; Nielsen & Christensen, 1994; Kelly et al., 1996; Borden et al., 1997). Unless the oxygen is not consumed, the reaction is observed to be very fast. Howard et al. (1991) collected and estimated aerobic half-lives of environmental pollutants, that range from 3 to 28 days for the BTEX compounds, with ethyl-benzene being the most degradable compound and the xylenes the most recalcitrant ones. Nielsen & Christensen (1994) investigated the variability of aerobic degra-

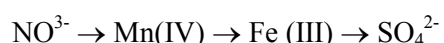
tion in laboratory experiments. They studied biodegradation in microcosms from different sampling locations within the same aquifer. Degradation rates for BTEX compounds varied within a factor of six for the individual sampling locations.

Due to the low solubility of oxygen in water and the only modest oxygen supply to a plume due to diffusion, the degradation capacity based on oxygen is often not high. Wiedemeier et al. (1999) collected data from 38 sites, where the biodegradation capacities for all terminal electron-accepting processes were determined. The average degradation capacity for oxygen related degradation was quantified to 3 % of the total degradation capacity.

3.4.2 Anaerobic degradation of hydrocarbons

After oxygen depletion, anaerobic conditions determine the microbial activities. For long times, anaerobic degradation of aromatic hydrocarbons was regarded as non-existent, very slow or incomplete (Wiedemeier et al., 1999). During the last ten to fifteen years, anaerobic degradation of aromatic compounds became an important research area, and several studies revealed complete mineralization mainly of BTEX compounds under various anaerobic conditions (e.g. Zeyer et al., 1986; Grbic-Galic & Vogel, 1987; Acton & Barker, 1992; Edwards & Grbic-Galic, 1992; Beller et al., 1992; Lovley et al., 1996). A general review on anaerobic transformation processes is given by Berry et al. (1987).

Environmental conditions and microbial competition determine, which anaerobic degradation process dominates. Typically, after oxygen depletion, the following sequence of electron acceptors is observed to degrade hydrocarbons:



Half-lives of BTEX compounds under anaerobic conditions are reported to be higher than under

aerobic conditions, and show a high variability (Howard et al., 1991; Edwards & Grbic-Galic, 1992; Davis et al., 1999; Schirmer et al., 1999; Wiedemeier et al., 1999). Some authors also observed benzene remaining recalcitrant under certain conditions (Acton & Barker, 1992; Davis et al., 1999; Thornton et al., 2000).

Even though anaerobic degradation occurs slower than aerobic degradation, at most sites anaerobic degradation plays the major role due to the larger occurrence of nitrate, iron and sulphate in comparison to oxygen. The average anaerobic degradation capacity of 38 sites was determined by Wiedemeier et al. (1999) with 81 % of the overall degradation capacity. Sulphate reduction contributes with 86 % the major part to the total anaerobic degradation capacity, followed by denitrification (11 %) and iron reduction (3 %).

3.4.3 Methanogenesis

If all electron acceptors mentioned in Sections 3.4.1 and 3.4.2 are depleted, methanogenesis can take place. Then, hydrocarbons act as both electron acceptor and donor (Wiedemeier et al., 1999; Acton & Barker, 1992; Grbic-Galic & Vogel, 1987). Methanogenesis is a two-step process: first, hydrocarbons are fermented to by-products like acetate and hydrogen. In the second step, acetate and hydrogen together with carbon dioxide are utilized by different micro-organisms to produce methane, carbon dioxide, and water (Chapelle, 1993).

The described reactions only occur under strongly reducing conditions (hydrogen concentrations greater than 5 nmol L^{-1}) and if carbon dioxide is present. Even though the process of methanogenesis is thermodynamically not as favourable as the above mentioned reactions, its contribution to the overall degradation capacity was quantified to 16 % (Wiedemeier et al., 1999).

3.5 Lines of evidence

In order to evaluate site-specific natural attenuation, “lines of evidence” have been developed by the US EPA (US EPA, 1999; Wiedemeier et al., 1999). According to these, the proof of occurring biodegradation at a specific site is given, if:

- historical contaminant data demonstrate a clear trend of decreasing contaminant mass over time
- analytical data show that geochemical conditions are suitable for biodegradation and that active biodegradation occurs. These data have to include evidence of:
 - decreasing concentrations of electron acceptors and donors,
 - increasing concentrations of metabolic by-products and daughter compounds.
- microbiological data support the occurrence of biodegradation.

To supply the last mentioned evidence, the US EPA suggests microcosm studies to demonstrate directly the occurrence of biodegradation. Hunkeler et al. (1999b; 2001b), Ahad et al. (2000) as well as Meckenstock et al. (1999) showed, that also changes in compound specific stable isotopes might indicate biodegradation. A more detailed description of the compound specific stable isotope analysis is given in Chapter 9.

4 The integral measuring and modelling approach

With respect to the growing importance of integrating natural attenuation as an alternative or additional remediation strategy into legislation, it is necessary to develop tools that adduce the proof of natural attenuation occurring at a specific site. One of the demanded “lines of evidence” by the US EPA (see Chapter 3) comprises the proof of decreasing concentrations and mass over time. Proving decreasing contaminant masses is best realized by determining contaminant mass flow rates, i.e. the mobile mass per time. From decreasing mass flow rates over time a decrease in the total, i.e. mobile and immobile, mass may then be inferred. Besides this evidence of mass reduction, a quantification of the dominating natural attenuation processes contributing to the contaminant reduction is of major importance.

Due to the heterogeneity of the subsurface, plume investigation at a contaminated site is often difficult and subject to high uncertainty. Thus, a decrease of concentration along an apparent flow path might be the result of an erroneous idea of the flow direction instead of natural attenuation.

To overcome the problem of heterogeneity when pursuing the two aims of

- (a) determining mass flow rates and
- (b) quantifying the contributions of natural attenuation processes

two approaches are followed. First, for the determination of mass flow rates, the sample volume is significantly enlarged to reduce the

influence of heterogeneity. This integral mass flow rate approach allows for an estimation of mass flow rates at a control plane and abandons the concept of concentrations measured at single points. Secondly, with the measured contaminant mass flow rates as input, the processes of natural attenuation are quantified by stochastic reactive transport modelling, accounting for the variability and uncertainty of flow and transport parameters.

Thus, the outline of this chapter is to elucidate the theory of the integral mass flow rate approach (Section 4.1) combined with stochastic transport modelling (Section 4.2). Together with Chapters 3 and 5 it represents the theoretical frame of this thesis.

4.1 The integral mass flow rate approach

In a heterogeneous system, numerous point measurements are necessary to describe a spatially varying parameter, like the concentration of a dissolved contaminant. Instead of increasing the number of single point measurements, which would require a dense network of cost-intensive boreholes, the idea of the mass flow rate approach is to increase the sample volume. This leads to a spatial integration and thus an averaging of the considered parameter in space.

This idea, which has been developed and firstly implemented at the Center for Applied Geo-

sciences of the University of Tübingen (Schwarz et al., 1998; Teutsch et al., 2000), is realized by pumping in one or several wells, that are positioned downgradient of the presumed contaminant source and perpendicular to the groundwater flow direction. During pumping, concentrations are measured in the withdrawn groundwater, that comprises water from increasing distances to the well. The position of the wells as well as the pumping rate and period are adjusted in a way, that the capture zones of the different wells touch or overlap. The sum of the well capture zones should then cover the whole width of the suspected plume.

The measured concentration time series in each well depends on the spatial distribution of the contaminant within the undisturbed aquifer, i.e. the plume concentration and plume position (Figure 4.1). Neglecting groundwater flow, the concentration in the pumping well, $C_{well}(t)$, is given by (Schwarz et al., 1998; Schwarz, subm.):

$$C_{well}(t) = \frac{1}{2\pi} \int_0^{2\pi} C_w(r(t), \varphi) d\varphi \quad (4.23)$$

with

$$r(t) = \sqrt{\frac{Q_p t}{\pi B n_e}} \quad (4.24)$$

$C_w(r, \varphi)$ describes the spatial distribution of the solute contaminant in spherical coordinates, where r denotes the radius of the isochrone at time t , Q_p the pumping rate, B the aquifer thickness and n_e the effective porosity.

Assuming an idealized plume of the concentration C_{plume} in a homogeneous aquifer (Figure 4.1a), the concentration distribution in the aquifer $C_w(r, \varphi)$ can be described by:

$$C_w(r, \varphi) = C_{plume} (H(r \cos \varphi - b_1) - H(r \cos \varphi - b_2)) \quad (4.25)$$

H represents the Heaviside function and b_1 and b_2 the distances from the well, that limit the plume (Figure 4.1a).

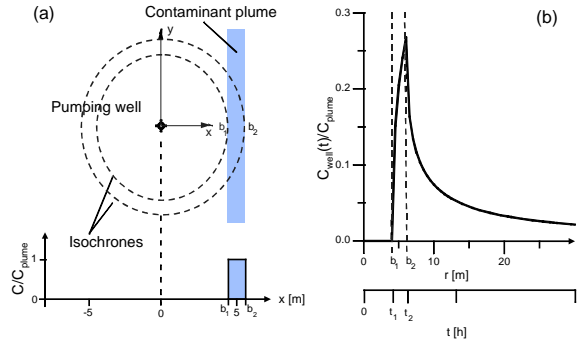


Figure 4.1 (a) Idealized plume and pumping well with two isochrones at a radius of b_1 and b_2 . The relative spatial concentration distribution perpendicular to the groundwater flow is plotted below. (b) Concentrations over time measured in the pumping well, normalized to the concentration in the plume (Schwarz, subm.).

Schwarz (subm.) developed an analytical solution for equation (4.23) where $C_w(r, \varphi)$ is substituted from equation (4.25). Thus, the spatial distribution of the concentration in the undisturbed aquifer can be determined from the measured concentration time series in the well, $C_{well}(t)$ (Figure 4.1b), when no concentration gradient within the plume is assumed. The solution is not unique, as the concentration distribution could be found at either side or both sides of the pumping well. Thus, $\hat{C}_{w,i}$ ($= \hat{C}_w(r(t_i))$) denotes the average concentration of both streamtubes of the undisturbed groundwater flow field positioned left and right from the pumping well at a distance r with $r_{i-1} < r < r_i$ (Schwarz, subm.):

$$\hat{C}_w(r(t_i)) = \frac{C_{well,i} \frac{\pi}{2} - \sum_{k=1}^{i-1} \hat{C}_{w,k} \left(\arccos \frac{r_{k-1}}{r_i} - \arccos \frac{r_k}{r_i} \right)}{\arccos \left(\frac{r_{i-1}}{r_i} \right)} \quad (4.26)$$

with $C_{well,i}$ and r_i representing the concentration measured at the well at time t_i and the radius of the isochrone at time t_i , respectively. The mass flow rate M perpendicular to the control plane in the undisturbed aquifer is then given by (Schwarz, subm.):

$$M = 2 \sum_{i=1}^n \hat{C}_{w,i} Q_i \quad (4.27)$$

with

$$Q_i = K_f |\nabla h| B (r_{i-1} - r_i) \quad (4.28)$$

where n denotes the total number of concentration measurements at the well, Q_i the volumetric discharge perpendicular to the control plane at both left and right streamtubes and $|\nabla h|$ the hydraulic gradient of the undisturbed aquifer. The radius r_i is defined by equation (4.24). With the obtained mass flow rate at the control plane (equation 3.5), also a mean concentration at the control plane can be determined by dividing the mass flow rate by the volumetric discharge of the whole control plane.

As mentioned before, the calculated concentration distribution is not unique. Especially if the well capture zones do not overlap, the exact position of the plume cannot be determined. Ptak et al. (2000) presented a numerical solution of the above mentioned problem, so that overlapping well capture zones as well as heterogeneous aquifer conditions can be accounted for.

Holder et al. (1998), Ptak & Teutsch (2000) and Bockelmann et al. (2001) applied the presented approach at different field sites and determined contaminant mass flow rates and mean concentrations across the considered control planes. Bockelmann et al. (2001) demonstrated an effective contaminant reduction of BTEX and PAHs at the 'Testfeld Süd' between two control planes at distances of 140 and 280 m downgradient of the source.

4.2 Stochastic transport modelling using measured mass flow rates

Processes in nature are subject to a considerable variability, resulting in both heterogeneity of naturally formed materials (e.g. sedimentary

structures) and temporal variability of ongoing processes (e.g. rainfall). As a consequence, describing processes occurring in nature, like e.g. flow and transport in the subsurface, requires knowledge of the spatial and temporal distribution of the parameters involved.

Two major lines of research have evolved in order to deal with the heterogeneity of subsurface parameters. One research goal has been to characterize the structures of the subsurface as concise as possible, mostly followed by a deterministic description of flow and transport processes. Considerable insight has been gained by improved measurement facilities at laboratory and field scale on the one hand and by a better understanding of the dominating sedimentological processes leading to heterogeneous formations on the other hand. Nevertheless, an exact deterministic description of naturally occurring materials is not possible.

The second line of research emerged from the assumption that uncertainty will always remain when describing flow and transport processes. This uncertainty stems from the fact, that a spatially distributed parameter can be measured only at relatively few locations of the investigated domain, i.e. exact information about parameter values between the measurement locations is not available, and that the measurement itself is subject to uncertainty. Thus, the development of both geostatistical methods that account for incomplete spatial information and models that are able to incorporate uncertainty of spatially varying parameters has been the second major research goal during the past 25 years.

In the following, a brief introduction into stochastic transport modelling is given (Section 4.2.1). The notion of combining integral mass flow rate measurements with stochastic transport modelling is presented in Section 4.2.2.

4.2.1 Concepts of stochastic transport modelling

Spatially varying parameters of naturally occurring materials often exhibit two important characteristics (Journel & Huijbregts, 1978): they show a high degree of variability but nevertheless reveal a certain spatial structure. Matheron (1971) termed them *regionalized variables*. They can be described by means of random variables that account for the spatial structure.

According to the stochastic notion (e.g. Journel & Huijbregts, 1978; de Marsily, 1986; Gelhar, 1993; Dagan & Neuman, 1997), the spatial distribution of a parameter observed in the domain U is the result of a random process, that can be described by a random function (RF). The observed distribution represents therefore *one* possible realization of the random function. The random function represents all random variables (RV) $Z(\mathbf{x})$ with $\mathbf{x} \in U$. Note, that in this section random variables are denoted with capital letters whereas their realizations are denoted with the corresponding lower case letters. Bold letters represent vectors.

A continuous random variable $Z(\mathbf{x})$ is defined by its cumulative probability distribution function (cdf), that describes the cumulative probability of the occurrence of the value z at a given point \mathbf{x} :

$$F(\mathbf{x}; z) = \text{Prob}(Z(\mathbf{x}) \leq z) \in [0, 1] \quad (4.29)$$

The definition of the cdf of a categorical random variable, that can take $k=1, \dots, K$ different states, is given by:

$$F(\mathbf{x}; k) = \sum_{i=1}^k \text{Prob}(Z(\mathbf{x}) \in \text{state } i) \in [0, 1] \quad (4.30)$$

The probability, that the value z of the continuous random variable $Z(\mathbf{x})$ lies in the interval of $[z; z+dz]$, is defined by the probability density function (pdf):

$$f(\mathbf{x}; z) = \frac{dF(\mathbf{x}; z)}{dz} \quad (4.31)$$

A random variable is often characterized by its first two central moments, the expected value $E[Z(\mathbf{x})]$ and the variance $VAR[Z(\mathbf{x})]$.

$$E[Z(\mathbf{x})] = \int_{-\infty}^{\infty} z f(\mathbf{x}; z) dz = \mu(\mathbf{x}) \quad (4.32)$$

$$\begin{aligned} VAR[Z(\mathbf{x})] &= \int_{-\infty}^{\infty} (z - \mu(\mathbf{x}))^2 f(\mathbf{x}; z) dz \\ &= E[(Z(\mathbf{x}) - \mu(\mathbf{x}))^2] \end{aligned} \quad (4.33)$$

The second important characteristic of a regionalized variable is its spatial structure (Journel & Huijbregts, 1978). The spatial correlation between two random variables at the locations \mathbf{x} and $\mathbf{x}+\mathbf{h}$, where \mathbf{h} is the distance vector, is described by the covariance $C(\mathbf{x}, \mathbf{x}+\mathbf{h})$:

$$\begin{aligned} C(\mathbf{x}, \mathbf{x}+\mathbf{h}) &= \\ E[(Z(\mathbf{x}) - \mu(\mathbf{x})) \cdot (Z(\mathbf{x}+\mathbf{h}) - \mu(\mathbf{x}+\mathbf{h}))] &= \\ E[Z(\mathbf{x}) \cdot Z(\mathbf{x}+\mathbf{h})] - \mu(\mathbf{x}) \cdot \mu(\mathbf{x}+\mathbf{h}) \end{aligned} \quad (4.34)$$

Also the semivariogram $\gamma(\mathbf{x}, \mathbf{x}+\mathbf{h})$, often just referred to as variogram, may be used to characterize the spatial relationship and is given by:

$$\gamma(\mathbf{x}, \mathbf{x}+\mathbf{h}) = \frac{1}{2} VAR[Z(\mathbf{x}) - Z(\mathbf{x}+\mathbf{h})] \quad (4.35)$$

With the presented concept of random functions, spatially varying parameters appearing in the flow and transport equations can be described, leading thus to a stochastic description of the dependent variables, e.g. head and concentration. In practice however, two important assumptions on the used random functions are made.

One is the *stationarity* of the random function, which calls for the spatial stationarity of its statistical properties, i.e. equations (4.32) through (4.35) become independent of \mathbf{x} . As a consequence, the statistical characteristics like the first two moments of a random variable can be obtained from pooling together observations taken at different locations in space.

The second important assumption is that of *ergodicity* that is defined as follows according to de Marsily (1986):

“Ergodicity implies that the unique realization available behaves in space with the same pdf as the ensemble of possible realizations. In other words, by observing the variation in space of the property, it is possible to determine the pdf of the random function for all realizations.”

As ergodicity is a characteristic of the random function and not of a single realization observed in the field, it is difficult to prove ergodicity in a given domain. Nevertheless, for most applications both stationarity and ergodicity are assumed.

Considering parameters of the flow and transport equation as random functions, these equations and their dependent variables become stochastic as well. Different approaches exist to solve stochastic differential equations, which are described in detail e.g. by de Marsily (1986) and Gelhar (1993). Analytical methods to obtain the first moments of the dependent variable are the perturbation method, e.g. applied by Gelhar & Axness (1983), Hoeksma & Kitanidis (1984), Reichle et al. (1998), Hassan et al. (1998) or the spectral method (e.g. Gelhar & Axness, 1983; Gelhar, 1986). Another widely used method to determine the uncertainty of the solution is the Monte Carlo method. Here, a large number of realizations of the considered random function are generated according to its probability density function and covariance or variogram. Solving the flow and transport equation numerically for each realization allows for a statistical analysis of the results, i.e. expected values and variances can be determined from the ensemble of calculated solutions. This method has been applied in numerous modelling studies (e.g. Freeze, 1975; Smith & Freeze, 1979; Burr et al., 1994; Selroos, 1995; Hassan et al., 1998).

In most applications, hydraulic conductivity is the parameter that is considered as a random function, thus leading to a stochastic flow field which is further used for transport simulations. Numerous studies in the 70s and 80s of the 20th century have been performed on the stochastic

description of flow and non-reactive transport (Freeze, 1975; Gelhar & Axness, 1983; Sposito et al., 1986; Dagan, 1984, 1986; Hoeksma & Kitanidis, 1984; Gelhar, 1986). Later, also transport parameters, like sorption and biodegradation parameters were treated as stochastic processes (e.g. Bosma & van der Zee, 1993; Burr et al., 1994; Simmons et al., 1995; Ginn et al., 1995, 2001; Miralles-Wilhelm et al., 1997; Reichle et al., 1998).

4.2.2 Determination of biodegradation rates by inverse stochastic transport modelling

Most of the aforementioned studies do not deal with transport problems at field scale or if they do so, synthetic scenarios are considered. Difficulties arise when simulating real field sites, where the dominating processes and their parameters have to be identified. Estimating the spatially varying parameters of the flow and transport problem on the basis of measured values of the dependent variable(s) (head and/or concentration) is referred to as the inverse problem. As in many cases a deterministic solution of the inverse problem did not reveal realistic or reliable outputs, stochastic parameter identification has been developed treating the spatially varying parameters as random functions (e.g. Kitanidis & Vomvoris, 1983; Hoeksema & Kitanidis, 1984; Rubin & Dagan, 1987a, b; Kuiper, 1986). These stochastic methods have been applied in case studies mainly to identify flow parameters. Measured heads and conductivities served then to condition the objective function of the inverse problem (Dagan & Rubin, 1988; Rubin et al., 1990; Vassolo et al., 1998; Capilla et al., 1998).

Although some authors have used concentration data to inversely determine transport or flow parameters, no study has been conducted, in which reactive transport parameters were estimated within a stochastic framework. Hendricks Franssen et al. (2001) used concentration data to

condition both the deterministic flow and transport equation, resulting in a complex coupled solution of both equations. Within a deterministic framework, conservative tracer test data have widely been used to estimate flow parameters (e.g. Wagner et al., 1999; Zechner et al., 1999). Furthermore, contaminant concentration data served to deterministically estimate reactive transport parameters like degradation coefficients (e.g. Hetterschijt et al., 1999; Schirmer et al., 1999; Suna et al., 2001).

In the present thesis, the biodegradation rate is estimated within a stochastic framework on the basis of contaminant concentration data or mass flow rates, respectively (Figure 4.2).

Flow is simulated in a Monte Carlo approach with stochastically generated aquifer realizations that account for hydraulic and, depending on the model approach used, also geochemical heterogeneity (Sections 5.1 and 6.3) (Figure 4.2, left hand side). The results of the Monte Carlo flow simulations represent an ensemble of flow fields with quantified first and second central moments of arrival times of an inert tracer.

Also the inverse reactive transport modelling is carried out within a Monte Carlo approach. The following five-step procedure is performed to inversely estimate the biodegradation rate (Figure 4.2, right hand side):

- (1) A degradation rate λ_d is guessed.
- (2) For each realization, consisting of a random flow field and a geochemical parameter field, reactive transport is simulated with the a priori estimated degradation rate λ_d .

Kinetic sorption is simulated forward as intra-particle diffusion.

The simulated concentration C_w^i at a point \mathbf{x}_{cp} on the control plane A_{cp} ($\mathbf{x}_{cp} \in A_{cp}$) for each realization i can be written as

$$C_w^i(\mathbf{x}_{cp}, \lambda_d, t) = \frac{1}{n_e} \int_t (\nabla(n_e \mathbf{D} \nabla C_w^i) - \nabla(\mathbf{v}_a^i n_e C_w^i) - R_s^i - n_e \lambda_d C_w^{i,n_d}) dt \quad (4.36)$$

where R_s^i denotes generally the term for kinetic sorption in realization i , \mathbf{v}_a^i the vector of flow velocities in realization i and n_d the order of the decay.

- (3) With the simulated concentrations for each realization $C_w^i(\mathbf{x}_{cp}, \lambda_d, t)$, the mass flow rate $M_{cp}^i(\lambda_d, t)$ for each realization at the control plane A_{cp} is calculated:

$$M_{cp}^i(\lambda_d, t) = \int_{A_{cp}} C_w^i(\mathbf{x}_{cp}, \lambda_d, t) \cdot \mathbf{e}_{cp} \mathbf{q}^i(\mathbf{x}_{cp}) dA \quad (4.37)$$

where \mathbf{e}_{cp} represents the unit vector normal to the control plane and $\mathbf{q}^i(\mathbf{x}_{cp})$ the vector of the specific discharge of realization i at the control plane. A_{cp} denotes the area of the control plane.

- (4) If the plume has reached steady state conditions, M_{cp}^i becomes independent of time t . The ensemble averaged mass flow rate $\langle M_{cp}^i \rangle$ for steady state conditions is given by:

$$\langle M_{cp}^i(\lambda_d) \rangle = E[M_{cp}^i(\lambda_d)] \quad (4.38)$$

- (5) In the last step, the simulated ensemble averaged mass flow rate $\langle M_{cp}^i \rangle$ is compared to the observed mass flow rate $M_{observed}$ at the control plane. The objective function $O_{cp}(\lambda_d)$ is defined as the absolute difference of the above mentioned mass flow rates:

$$O_{cp}(\lambda_d) = |\langle M_{cp}^i(\lambda_d) \rangle - M_{observed}| \quad (4.39)$$

The objective function is then minimized by trial and error, i.e. a new degradation rate λ_d' is estimated and the described procedure is started again from step (2), until the minimum of $O_{cp}(\lambda_d)$ is found.

The presented approach to identify the mean biodegradation behaviour comprises several striking advantages:

- Instead of point concentration measurements, that are subject to great uncertainty due to hydraulic and geochemical heterogeneity,

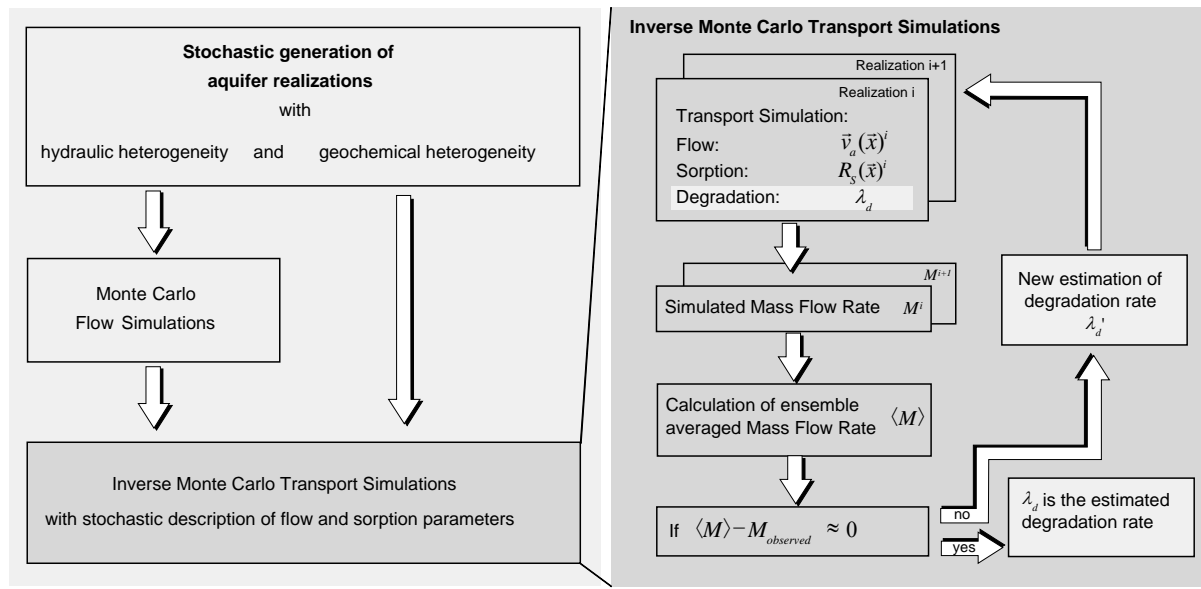


Figure 4.2 Flow diagram of the stochastic modelling approach to inversely estimate biodegradation rates.

measured integral mass flow rates are used to condition the inverse transport problem. If measured mass flow rates exist at several control planes, a better conditioning and thus a higher reliability of the estimated degradation rate is obtained.

- Hydraulic and, depending on the used model approach, also geochemical heterogeneity can be accounted for in a Monte Carlo approach, i.e. besides the mean transport behaviour, the variance due to the uncertainty of the flow field and the geochemical parameter field can be quantified.
- The degree of freedom of the inverse problem is reduced by forward modelling of the kinetic sorption as intraparticle diffusion with experimentally measured parameters.

The main drawbacks of this approach are, that only integrated process parameters are estimated, i.e. a spatial resolution of the identified process is not possible. Furthermore, when considering transport distances that are small in relation to the integral scale, non-ergodic conditions might arise and question the use and meaning of mean concentrations or mean mass flow rates, as $\langle C_w \rangle$ or $\langle M \rangle$ become purely

statistical but not measurable parameters (Dagan, 1997).

5 Concepts for modelling Natural Attenuation at field scale

Modelling natural attenuation at field scale within a stochastic framework requires reliable tools to first describe and quantify the variability, i.e. heterogeneity, of the input parameter(s) and then to simulate transport of the considered contaminants in the heterogeneous field by describing the relevant processes in a physically based approach as best as possible.

This chapter provides a description of the tools that are used for the reactive transport modelling within this thesis. It comprises the facies approach, that was developed and applied by Herfort (2000) to delineate hydraulic and geochemical heterogeneity at the 'Testfeld Süd' (Section 5.1). Furthermore, the two model approaches used are presented, the fully three-dimensional Eulerian model MT3D-IPD (Section 5.2) and the control plane based one-dimensional Lagrangian model SMART (Section 5.3). The comparison of the two modelling tools in order to determine the applicability of SMART is given in Chapter 7, after the geostatistical analysis of the facies in Chapter 6.

5.1 Description of hydraulic and geochemical heterogeneity: the facies approach

5.1.1 Background

Originally stemming from sedimentology, sedimentary facies were used to delineate "three-dimensional bodies of sediment whose differen-

tiation provides a useful conceptual framework within which to characterize the heterogeneous properties of sedimentary deposits" (Allen-King et al., 1998). Sedimentary facies are usually distinguished by their different structural and textural features, grain sizes and lithologies, that allow for an inference of the sediment transport and the depositional conditions (Miall, 1992, 1996).

In hydrogeologic facies models, the differentiating factors are hydrogeologic properties, often hydraulic conductivity and porosity (Anderson, 1989). For instance, Davis et al. (1993), Ritzi et al. (1994) and Jussel et al. (1994a) used facies to describe hydraulic conductivities in aquifers. Besides the sole description of facies, Jussel et al. (1994a, b), Rauber et al. (1998), de Marsily et al. (1998), Ritzi et al. (1995) and Ritzi (2000) used geostatistical means to quantify the spatial structure of the facies and thus of the correlated hydraulic attributes. Koltermann & Gorelick (1996) gave a broad review on describing heterogeneities in sedimentary deposits.

Although a dependence between hydraulic and geochemical properties has been observed before (e.g. Robin et al., 1991), Allen-King et al. (1998) were the first to describe the spatial variability of K_d coefficients using a facies approach. They investigated the correlation between K_f and K_d within the same facies by measuring both coefficients for numerous core samples. They showed that the correlation between K_f and K_d is significant within a facies, but varies between the different facies. Further-

more, they found that the correlation is not significant for undifferentiated samples, i.e. for bulk samples consisting of all facies. Thus they concluded, that the facies approach is appropriate to describe geochemical and hydraulic heterogeneity.

5.1.2 Improved facies approach applied at the 'Testfeld Süd'

Allen-King et al. (1998) observed, that geochemical and hydraulic properties, i.e. K_d and K_f , correlate if the samples are differentiated according to a facies approach. But they did not differentiate the facies itself into its lithological or mineralogical components. Robin et al. (1991), who were first to investigate the correlation between K_d and K_f but without any facies or lithological decomposition of the samples, concluded that the observed variability of the correlation coefficients probably stems from the mineralogical characteristics of the aquifer material. Results from Rügner et al. (1997) support these findings. They furthermore demonstrated experimentally that sorption characteristics of different lithological components cannot be represented by effective sorption parameters of the bulk sample. Recently, Zhu & Burden (2001) showed by means of numerical simulations the significant impact of the mineralogical composition of the aquifer material on reactive transport.

Including the above mentioned findings, a new improved facies approach, that includes information on the lithological components of each facies, was developed at the Center for Applied Geosciences and applied at the 'Testfeld Süd' (Herfort, 2000). Herfort (2000) differentiated three facies types by grain size analysis as well as by soft information from drilling profiles:

- Facies G: Gravel with a small fraction of fine material showing a unimodal grain size distribution (Figure 5.1a)
- Facies Gm: Gravel with notable fraction of fine material showing a bimodal grain size dis-

tribution, denoted as 'Gravel with matrix' (Figure 5.1b)

- Facies S: well sorted sand with a unimodal grain size distribution (Figure 5.1c)

Herfort (2000) analysed the lithological composition of each grain size fraction within each facies, resulting in a detailed lithological description of the three facies (Figure 5.1). He attributed to each facies a hydraulic conductivity and to each lithological component a set of geochemical parameters.

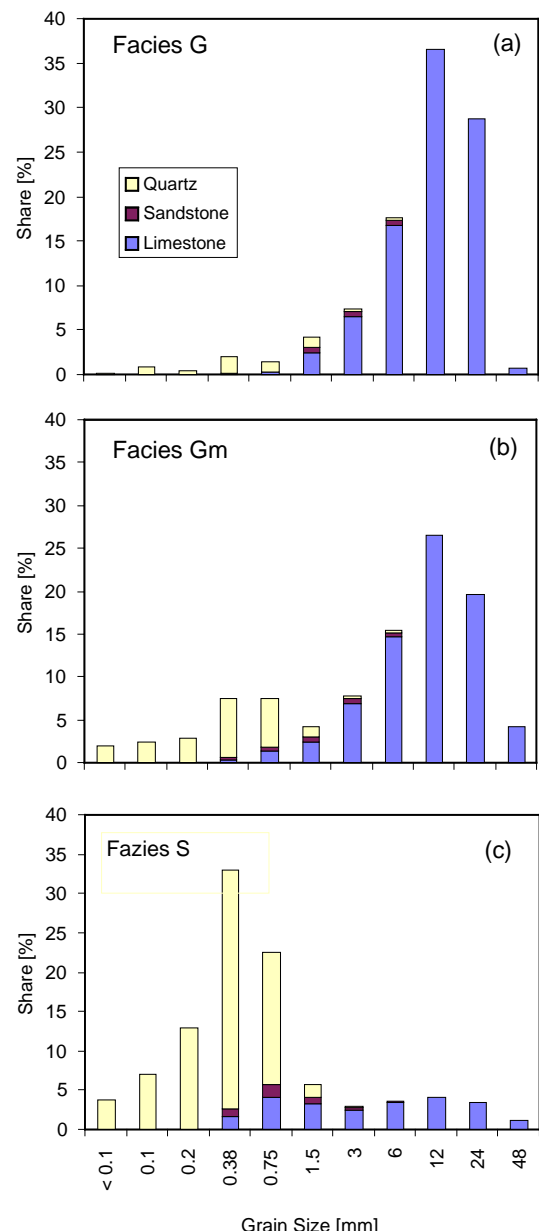


Figure 5.1 Grain size distribution and lithological composition of the original facies types at the 'Testfeld Süd' (Herfort, 2000).

Table 5.1 Hydraulic conductivities of the facies types, determined from sieve analysis (Herfort, 2000).

	Facies G	Facies Gm	Facies S
K_f [m s ⁻¹]	1.6 E-2	1.1 E-4	7.2 E-5

Hydraulic conductivities were determined from sieve analysis for the three facies types and are listed in Table 5.1.

Sorption parameters necessary to describe kinetic sorption were experimentally determined for phenanthrene for each lithological component (Rügner et al., 1997; Grathwohl & Kleineidam, 1995). For acenaphthene, isotherm measurements were performed within this thesis and are listed in Table 5.3.

Herfort (2000) simulated kinetic sorption in batch experiments for each facies type consisting of the above mentioned lithological composition, using the measured data as input. In order to reduce the enormous computational effort with regard to field-scale simulations, he determined effective facies types, consisting of two grain size classes and the dominating lithological components (Figure 5.2). As the facies G consists mainly of limestone, it was possible to represent the effective facies type G just by one lithological component, called artificial component, with similar characteristics as limestone. Herfort (2000) proved that for certain concentration and time ranges (10-10000 µg L⁻¹ and 0-100 years) the effective facies types show a similar sorption behaviour as the original facies types.

Table 5.2 summarizes the lithological composition of the effective facies types and Table 5.3 shows the physico-chemical parameters of the lithological components.

Table 5.2 Lithological composition of effective facies types at the 'Testfeld Süd'.

	Effect. Facies G	Effect. Facies Gm	Effect. Facies S
Total frequency [%]	33.7	59.0	7.3
Artificial component G_{eff} [%]	100	0	0
Limestone [%]	0	67.3	14.7
Quartz [%]	0	32.7	85.3

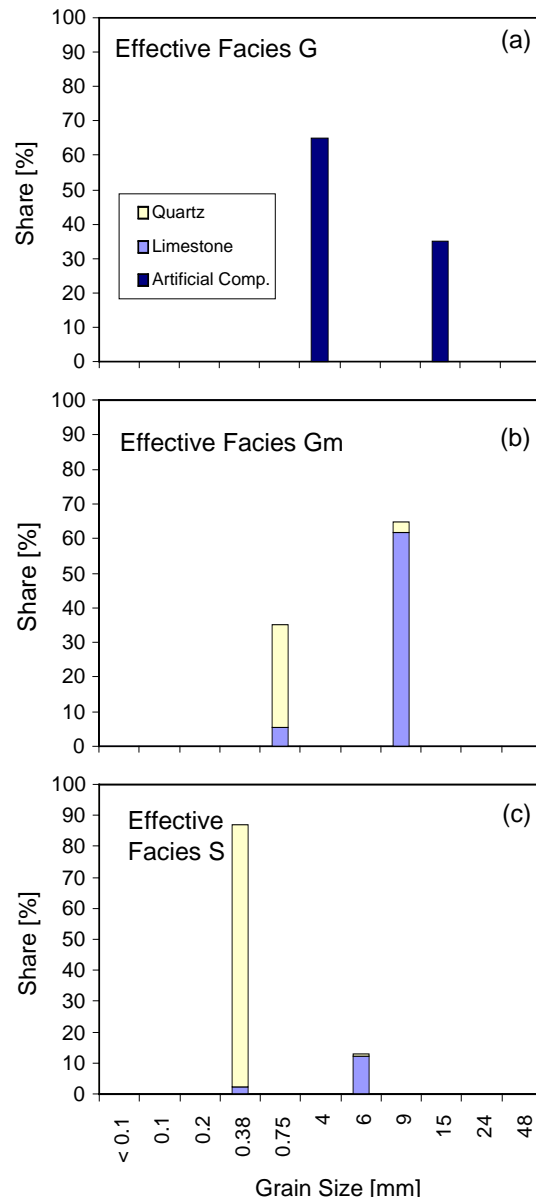


Figure 5.2 Effective facies types, their grain size distribution and their lithological composition (Herfort, 2000).

Table 5.3 Physical and chemical parameters of the lithological components (ε : intraparticle porosity; τ : tortuosity; d_s : solid density). Isotherm parameters are valid for acenaphthene (K_{fr} : Freundlich coefficient determined for concentrations in mg L⁻¹; $1/n_{fr}$: Freundlich exponent).

Lithology	ε [-]	τ [-]	d_s [kg·L ⁻¹]	K_{fr} [L·kg ⁻¹]	$1/n_{fr}$ [-]
G_{eff}^1	0.013	61.8	2.72	5.75	0.83
Limestone ²	0.012	59.0	2.73	3.29	0.83
Quartz ³	0.0005	9.0	2.65	0.07	1

Data origin: ¹ Herfort, 2000. ² Rügner et al., 1997.

³ Grathwohl & Kleineidam, 1995.

Based on the results of Herfort (2000), all further work and simulations in this thesis were performed using the effective facies approach. Applying this improved facies approach, hydraulic and geochemical heterogeneity can be accounted for by deterministically or stochastically obtained facies distributions.

5.2 Eulerian model approach – MT3D-IPD

Within the Eulerian model approach, the transport equation (3.3) is solved, yielding the concentration C_w at any location for any time. In this thesis, the basic transport model tool MT3D (Zheng, 1990; Zheng & Wang, 1998) is used, that numerically solves equation (3.3) according to a finite difference solver.

The modular structured code MT3D allows for an easy integration of new model packages. After the successful verification of the model tool BESSY (Batch-Experiment-Simulation-System), that simulates intraparticle diffusion in

closed systems (Jäger, 1996; Jäger & Liedl, 2000), a new module IPD (intraparticle diffusion module) based on BESSY was introduced into MT3D (Liedl & Ptak, subm.). This model package was developed at the Center for Applied Geosciences of the University of Tübingen to realistically integrate the improved facies approach as described in Section 5.1.2. Figure 5.3 schematically depicts the concept of the coupled transport model MT3D-IPD.

The code MT3D provides the basic framework, within which advection and dispersion is solved by spatially and temporally discretising the model domain and the simulation period. Each model cell in MT3D represents a single facies, that hydraulic properties are attributed to (Figure 5.3, upper part). After each advective and dispersive time step, the calculated solute concentration in each model cell is used as boundary condition for the calculation of the sorption processes.

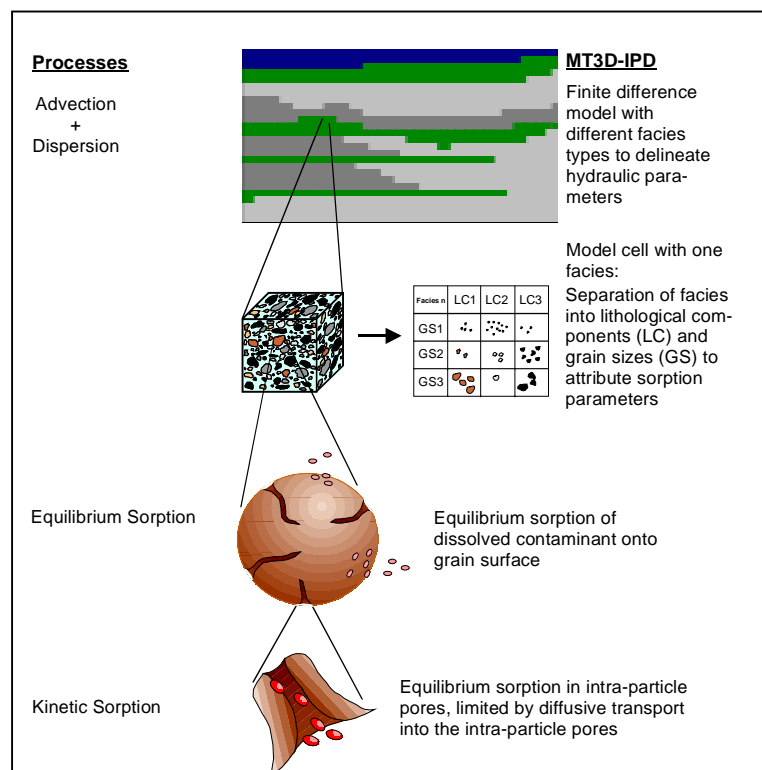


Figure 5.3 Model concept of the finite difference model MT3D combined with the module IPD for the simulation of intraparticle diffusion.

Equilibrium sorption (see also Section 3.3.1) is accounted for by applying the concept of isotherms, that relate solute and sorbed concentrations. In the simplest case the isotherm is linear (equation 3.6). Non-linear isotherms are for instance the Freundlich or Langmuir isotherms, equations (3.7) and (3.8).

The simulation of intraparticle diffusion (see Section 3.3.2) is performed separately for each lithological component and grain size. Thus, according to the presented facies approach, a lithological decomposition of each facies has to be carried out (Figure 5.3, middle). For each component of aquifer material (defined by a lithology j and grain size k), the diffusion equation, that describes the migration of solute compounds into the intraparticle pores, has to be solved (Jäger & Liedl, 2000):

$$\frac{\partial}{\partial t} (\varepsilon_j C_{w,jk} + \rho_j C_{s,jk}) = -\frac{1}{r^2} \frac{\partial}{\partial r} (r^2 m_{jk}) \quad (5.40)$$

where m_{jk} is the mass flux according to Fick's Law:

$$m_{jk} = -D_{e,j} \frac{\partial C_{w,jk}}{\partial r} \quad (5.41)$$

with $D_{e,j}$ representing the effective diffusion coefficient, ε_j the intraparticle porosity, ρ_j the bulk density of the lithological component j , r the radial coordinate, $C_{w,jk}$ and $C_{s,jk}$ the solute and sorbed concentration of the lithological component j and grain size k , respectively. Equation (5.40) is valid under the assumption of spherical grains.

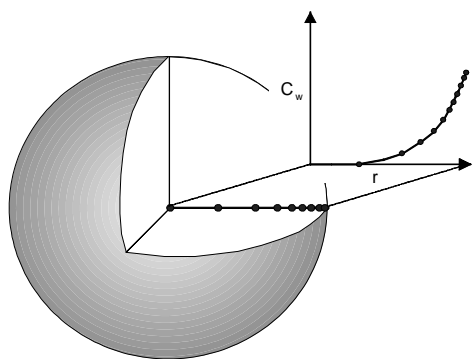


Figure 5.4 Schematic illustration of spatial discretisation within a grain along the radius r (after Jäger & Liedl, 2000).

The relationship between $C_{w,jk}$ and $C_{s,jk}$ in (5.40) has to be specified by an isotherm, e.g. the often used Freundlich isotherm (3.7). Together with equations (5.40) and (5.41) it represents the system of differential equations, that is non-linear in the case of a non-linear isotherm. By introducing a radial and temporal discretisation of each grain (Figure 5.4), the differential equations are solved using a finite difference scheme (Jäger, 1996).

Apart from a few preliminary simulations done by Herfort (2000), the model tool MT3D-IPD was used for the first time within the framework of this thesis. Extensive testing and verifying of the code was carried out, before the program was applied for the simulations shown in this thesis.

5.3 Lagrangian model approach - SMART

The transport model SMART (Streamtube Model for Advective and Reactive Transport) was developed at the Center for Applied Geosciences of the University of Tübingen (Finkel et al., 1998; Finkel, 1999) and is based on the Lagrangian approach after Cvetkovic & Dagan (1994) and Dagan & Cvetkovic (1996).

In contrast to the Eulerian approach, the idea of the Lagrangian approach is to describe transport by the motion of conservative particles along trajectories in a Eulerian steady state flow field. Each particle's trajectory can be interpreted as a streamtube of infinitesimal cross sectional area. The time dependent particle position is calculated by solving the advection equation. The spatial discretisation along the streamtube is expressed by the travel time τ of an inert tracer:

$$\Delta x_{cell} = v_x \cdot \Delta \tau \quad (5.42)$$

where $\Delta \tau$ is the cell discretisation by travel time, v_x the average flow velocity and Δx_{cell} the cell

length corresponding to the travel distance of a particle with mean flow velocity. Within a stochastic framework, conservative transport along the ensemble of streamtubes is considered by a probability density function (pdf) of travel times, that accounts for the uncertainty of hydraulic properties along the particle's trajectory. Deterministically, the pdf of travel times might be interpreted as the travel time distribution due to hydraulic heterogeneity in a larger flow domain that is represented by a single streamtube. The one-dimensional model domain is limited by an upgradient and a downgradient control plane (Figure 5.5). Due to the control plane based description of the flow and transport processes, mass flow rates measured at control planes by the integral mass flow rate approach (see Section 4.1) can directly serve as model input.

A great advantage of Lagrangian transport models is the possibility of a mathematical separation of advection and reactive transport processes. In SMART, each model cell represents a separate reactor, within which the reactive processes are simulated (Figure 5.5). The following processes, relevant for this thesis, are considered in SMART:

- (a) equilibrium sorption of organic contaminants on the outer surfaces of the aquifer material
- (b) intraparticle diffusion of organic contaminants
- (c) biodegradation of organic contaminants

Concerning the sorption processes, a factor f_{eq} ($0 \leq f_{eq} \leq 1$) defines the fraction of 'fast' (equilibrium) sorption in comparison to 'slow' (kinetic) sorption, i.e. intraparticle diffusion. Equilibrium sorption is accounted for by sorption isotherm models, according to equations (3.6) to (3.8). To simulate intraparticle diffusion, the module BESSY (Jäger, 1996; compare Section 5.2) was recently integrated into SMART (Liedl & Bold, 2001) allowing non-linear sorption in the intraparticle pores.

Both, equilibrium and kinetic sorption are simulated according to the lithological characteristics of the aquifer material, that consists of a heterogeneous composition of lithologies and grain sizes. Due to the Lagrangian idea of a temporal discretisation along the streamtube, a spatially varying composition of aquifer material cannot be accounted for. Thus, the facies approach presented in Section 5.1.2 is only restrictedly realizable using the modelling tool SMART.

Biodegradation is accounted for in SMART as a decay of n^{th} -order, as described in detail in Section 3.4 by equations (3.17) through (3.22).

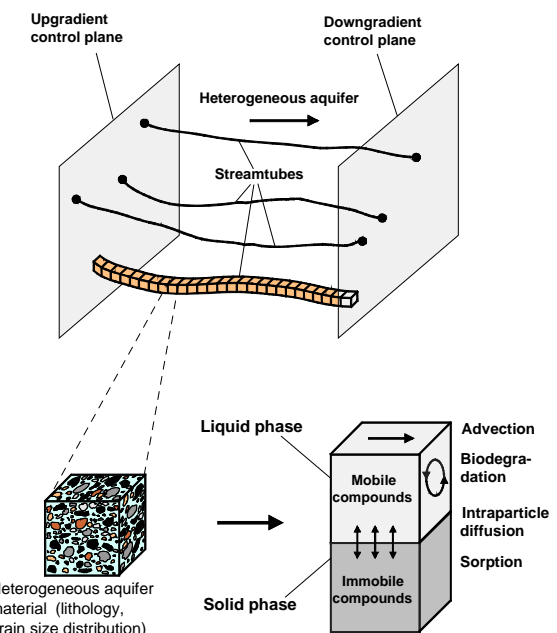


Figure 5.5 Schematic illustration of the streamtube model SMART (Finkel, 1999).

All described reaction processes in SMART constitute the reaction function Γ . Γ represents the simulated concentration profiles along the streamtube for each simulation time step.

After the reaction function is determined, advection and reaction processes are coupled. The breakthrough curve of the reactive compound at the downgradient control plane is then calculated by convolution of the pdf of travel times

and the reaction function (Finkel, 1999; Finkel et al., 1998):

$$C_w(t_i, x_{cp}) = \sum_m f(\tau_m, x_{cp}) \cdot \Gamma(\tau_m, t_i) \cdot \Delta \tau_m \quad (5.43)$$

$f(\tau_m, x_{cp})$ denotes the pdf of travel time at the location x_{cp} , $\Delta \tau_m$ is the discretisation of the m^{th} cell.

The following general assumptions have to be made when applying the streamtube model SMART:

- The flow field is steady state, i.e. the particles' trajectories are time independent.
- The heterogeneity of the hydraulic conductivity can be described by the variability of flow velocities.
- Macro-dispersion due to the variability of flow velocities is large in comparison to local-scale dispersion.
- Geochemical and biodegradation parameters can be assumed constant within the model domain.

6 Geostatistical analysis at the 'Testfeld Süd'

6.1 Introduction

One of the major challenges in hydrogeology is to assess the heterogeneity of aquifer parameters. Koltermann & Gorelick (1996) gave a broad overview on concepts of assessing and delineating spatial sediment variability and the connected aquifer parameters like hydraulic conductivity. They distinguished between three major categories of image producing approaches. Structure-imitating methods are based on spatial statistics and probabilistic rules to determine and depict the spatial relations within an aquifer. Process-imitating approaches solve equations which represent either the processes through which sedimentary deposits are formed or describe subsurface flow and transport. The third category comprises descriptive methods that divide the aquifer into different zones using hydraulic measurements and geologic observations to constitute a conceptual depositional model.

The basic aim of geostatistical analysis, constituting a structure-imitating method (Koltermann & Gorelick, 1996), is to quantify the spatial structure of an aquifer parameter that is described as a regionalized variable (Matheron, 1971; see also Section 4.2.1). The spatial relationship of a regionalized variable is quantified by variogram analysis providing the input either for a best estimation of the spatial parameter distribution (kriging) or for the simulation of equally likely aquifer realizations.

Variogram analysis (equation 4.13) of continuous variables like hydraulic conductivity has been performed by e.g. Rehfeldt et al. (1992),

Hess et al. (1992), Sanchez-Vila et al. (1995), Troisi et al. (2000) and Vereecken et al. (2000). In all these studies, either hydraulic conductivity/transmissivity or their logarithms were used to analyse the spatial relationship by two- or three-dimensional variograms. Problems arise, when the considered hydraulic property underlies systematic spatial variations due to its structural nature, e.g. the spatial relationship of hydraulic conductivity within sand lenses might be different than within gravel deposits. Furthermore, variogram analysis becomes difficult when applied to variables that vary over several orders of magnitude, like hydraulic conductivity.

Thus, Journel (1983) introduced an indicator approach, that classifies a continuous variable into $n+1$ categories by defining n threshold values. Transforming the continuous variable into $n+1$ indicator variables then allows for a separate description of the spatial structure by indicator variogram analysis within each class. This approach also enables the use of non-continuous, i.e. categorical variables like lithofacies or hydrofacies (Section 5.1). Besides the advantage of correlating not only hydraulic but also geochemical properties to a facies (Section 5.1.2), another striking feature of the indicator approach using categorical variables is the possibility of incorporating soft information into the geostatistical analysis. Thus, lithologic data from drilling profiles (Herfort, 2000) and geophysical measurements (Cotyp & Robin, 1995; Hubbard et al., 1999; Huggenberger & Aigner, 1999) have been accounted for in facies classifications. Indicator variogram analysis using facies types as categorical variable has been

done e.g. by Schad (1993), Ritzi et al. (1995), de Marsily et al. (1998), Ritzi (2000).

The aim of this chapter is to provide equally likely aquifer realizations of facies distributions for the 'Testfeld Süd' as basis for the subsequent Monte Carlo flow and transport simulations in Chapters 7, 8 and 9. By applying the indicator based approach, it is possible to incorporate the improved facies approach developed by Herfort (2000). According to the classification of Koltermann & Gorelick (1996) this approach results in a hybrid approach of structure-imitating and descriptive methods, as the described facies types are analysed by geostatistical means. Section 6.2 presents the performed indicator variogram analysis for the 'Testfeld Süd'. Section 6.3 describes the generation of aquifer realizations and Section 6.4 their characterization with respect to flow and conservative transport.

6.2 Variogram analysis

The indicator variogram analysis performed within this thesis involves two major steps (Figure 6.1): Firstly, the development of an indicator database, including the classification of appropriate facies types and their transformation into indicator variables; and secondly, the ana-

lysis of the spatial relationship of the indicator variables, resulting in experimental and fitted theoretical variograms for the beforehand determined main directions of anisotropy.

6.2.1 Development of the indicator database

From 122 sieve analyses and lithological decompositions, Herfort (2000) classified three facies types (Section 5.1.2): the facies 'gravel' (G), the bimodal facies 'gravel with matrix' (Gm) and the facies 'sand' (S). Together with borehole information of 85 observation wells, a three-dimensional data set of facies types is developed, using a 0.2 m grid to define the vertical spacing (Figure 6.1, left).

The categorical random variable $Z(\mathbf{x})$, representing the facies type, is transformed into the corresponding indicator variable $I(\mathbf{x}, k)$ that defines the mutually exclusive spatial occurrence of the facies k (Figure 6.1, left):

$$I(\mathbf{x}, k) = \begin{cases} 1 & \text{if } Z(\mathbf{x}) \in \text{category } k \\ 0 & \text{otherwise} \end{cases} \quad (6.44)$$

The obtained three-dimensional indicator database comprises 1415 data points for each of the three facies types.

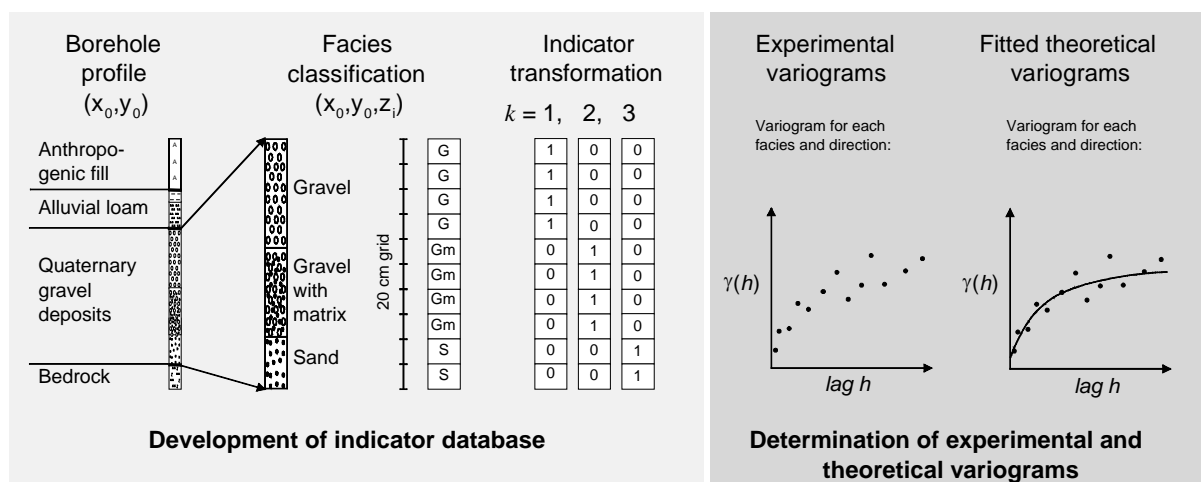


Figure 6.1 Schematic illustration of the indicator variogram analysis using the categorical variable 'facies'.

6.2.2 Determination of experimental and theoretical variograms

The geostatistical software library GSLIB by Deutsch & Journel (1992) is used for the determination of experimental variograms. The variogram analysis implies the investigation of the spatial continuity of all pairs of the considered variable that are separated by the distance vector \mathbf{h} . Anisotropy of the considered variable as well as the scale of the spatial variability often causes a high sensitivity of the outcome of the variogram analysis on the variogram parameters. Thus, Isaaks & Srivastava (1989) suggested to evaluate first the main variogram parameters that characterize anisotropy and the scale of spatial variability of the considered variable by determining the main directions of anisotropy and the lag distance. Then, three-dimensional directed variograms according to the determined characteristics can be calculated.

Using omnidirectional variogram analysis, the best suited lag distance and lag tolerance is determined for each facies (Figure 6.2 and Table 6.1). The main axes of horizontal anisotropy are determined for each facies as described in Isaaks & Srivastava (1989) by evaluating rose diagrams of the ranges determined from eight directional horizontal variograms. All three facies show correspondingly a main axis of horizontal anisotropy or direction of large range at 112.5° eastern deviation from north. This approximately corresponds to the flow direction of the river Neckar, indicating the strong correlation between sedimentary structure and the depositional transport direction. The direction of small range is determined by 22.5° eastern deviation from north.

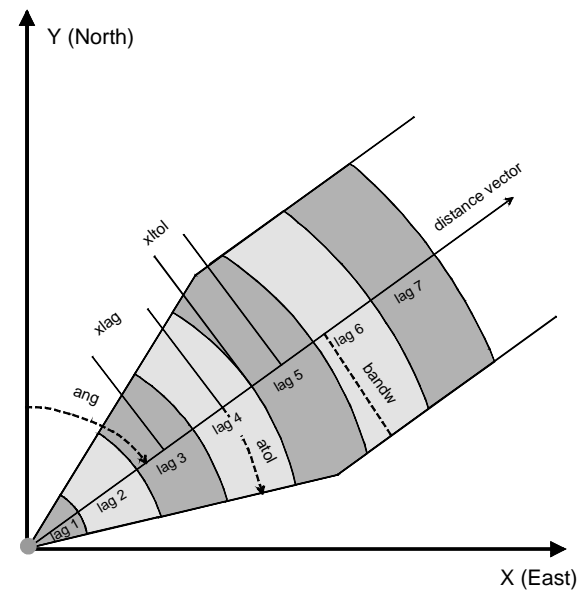


Figure 6.2 General definitions of variogram parameters needed for the determination of experimental variograms. The notation is according to the GSLIB program gamv3m. (ang: angle of distance vector; xlag: lag distance; xtol: lag tolerance; atol: angle tolerance; bandw: bandwidth) (after Deutsch & Journel, 1992).

Based on these a priori evaluated variogram parameters listed in Table 6.1, three-dimensional experimental indicator variograms (equation 4.13) for each facies are calculated according to the determined horizontal directions of large and small anisotropy and for the vertical direction (Figure 6.3). For all three facies and all directions a clear increase of γ is observed with increasing distance h . This finding states a spatial continuity within each facies for distances smaller than the range, that is characterized when $\gamma(h)$ reaches the sill.

Table 6.1 Parameters used for the determination of the experimental variograms. Directions: 1. Horizontal 112.5° , 2. Horizontal 22.5° , 3. Vertical. (For the definition of the abbreviations see Figure 6.2).

Direction	Facies G				Facies Gm / Facies S			
	xlag [m]	xtol [m]	atol [°]	bandw [m]	xlag [m]	xtol [m]	atol [°]	bandw [m]
1	25	12.5	30	25	20	10	30	25
2	25	12.5	30	25	20	10	30	25
3	0.2	0.1	45	1	0.2	0.1	45	1

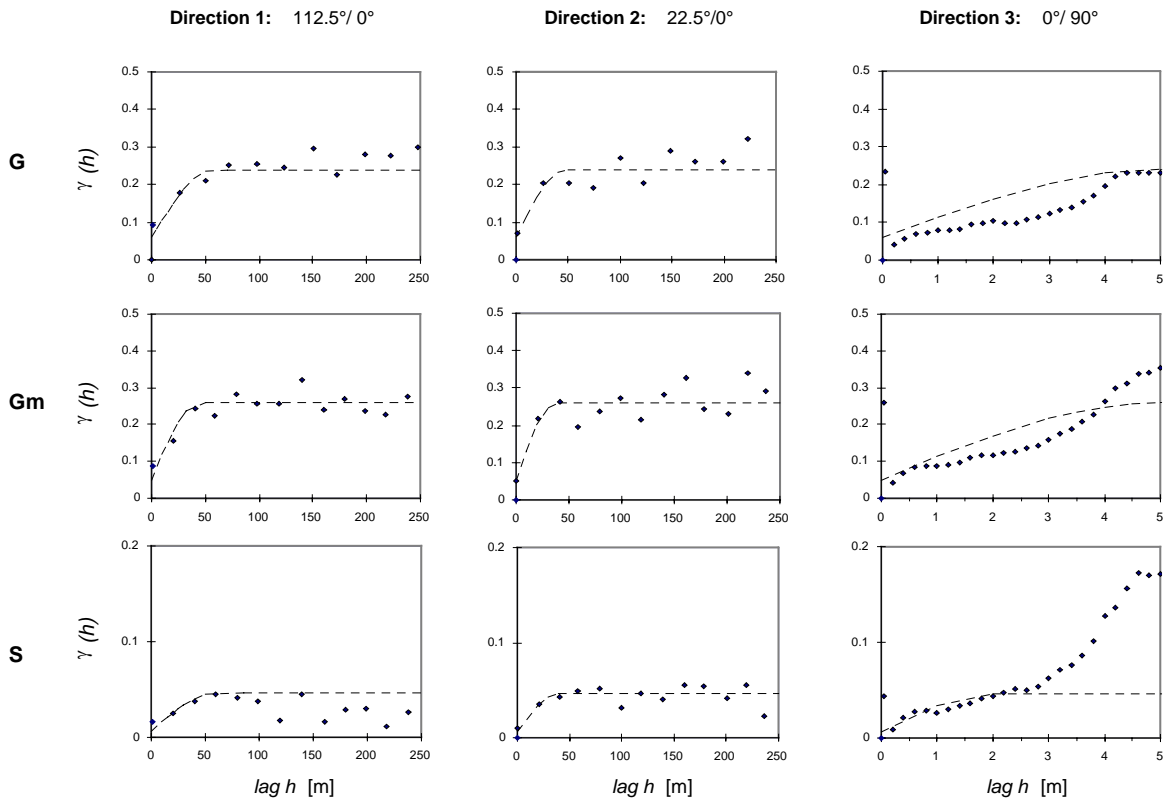


Figure 6.3 Three-dimensional experimental and theoretical indicator variograms of the categorical variable 'facies' with its three states 'gravel', 'gravel with matrix' and 'sand'. The directions are defined by two angles: (1) the horizontal deviation from north and (2) the vertical deviation. Diamonds represent the experimental variograms, dashed lines the theoretical variograms.

Three-dimensional spherical variogram models are fitted to the experimental variograms of each facies type, defining the same nugget and sill for all directions (Figure 6.3 and Table 6.2b). The facies 'gravel' and the facies 'gravel with matrix' show a similar behaviour for the two horizontal directions: the values of $\gamma(h)$ increase with increasing h , reaching a sill of 0.22 and 0.26, respectively. Facies G reveals a little bit higher values for both ranges in comparison to facies Gm: 58 and 48 m for the large and small range, respectively, compared to 45 and 38 m. Facies S shows large and small horizontal ranges in the same order of magnitude with 60 and 40 m, respectively. Due to the lower occurrence of the facies S (7.3 %, see also Section 5.1.2), the indicator variogram values reach only a sill of 0.046.

The vertical variograms of all three facies do not reveal a clear vertical range: values of 2 to 5 m may be suggested, emphasizing the difficulty of determining a vertical length scale in a thin

and stratified aquifer. Desbarats & Bachu (1994) stress the fact, that reliable variogram results can only be obtained for lags up to one half of the considered aquifer thickness. In this case the aquifer thickness reaches a maximum of 5.7 m with a mean of 2.7 m (Herfort, 2000). In comparison to the horizontal variation of facies and in awareness of the large horizontal aquifer extension compared to the small vertical extension, the vertical range is in this case of minor importance.

Table 6.2 Parameters of theoretical variogram models. (a) Values of large and small horizontal range and vertical range. (b) Values of nugget a_0 and sill a .

(a)		G	Gm	S
	Direction	l [m]	l [m]	l [m]
	1	58	45	60
	2	48	38	40
	3	5	5	2

(b)		G	Gm	S
	a_0 [-]	0.06	0.05	0.006
	a [-]	0.22	0.26	0.046

6.3 Generation of aquifer realizations

Using the indicator variograms and the overall frequency of each facies as input, equally likely aquifer realizations are generated. The program code sisimpdf (sequential indicator simulation of categorical variables) of the software package GSLIB (Deutsch & Journel, 1992) is applied to generate realizations of facies distributions. The algorithm of the sequential indicator simulation can be described as follows (e.g. Deutsch & Journel, 1992):

The conditional cumulative distribution function (ccdf) of the categorical variable *facies* Z_j at N nodes of a dense grid is denoted with

$$F_{(N)}(z_1, \dots, z_N | (n)) = \sum_{i=1}^k \text{Prob}(Z_j \in \text{state } i, j = 1, \dots, N | (n)) \quad (6.45)$$

where $| (n)$ represents the conditioning by a set of n original data points in the first step and/or previously simulated data points in the following steps.

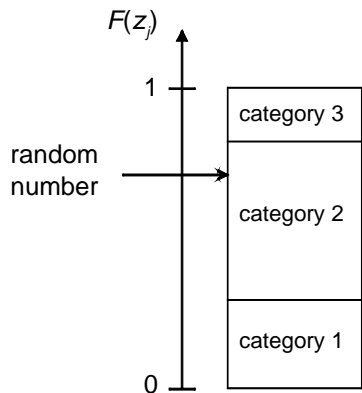


Figure 6.4 Determination of the simulated category from a random number and the conditional probabilities of the categorical variable (after Schad, 1997).

Then the simulation principle is applied repeatedly along a random path over the grid:

- From the original data and/or previously simulated data, that lie within a defined search area, the ccdf is determined by ap-

plying indicator kriging (Deutsch & Journel, 1992).

- A random number within $[0;1]$ is drawn and according to the ccdf the value z_j is determined (Figure 6.4). z_j is then considered as a conditioning data point for the subsequent drawings. After the random determination of the next grid point, the procedure is repeated starting at step 1.

The extension, orientation, conditioning and grid size of the realizations to be generated depend on the purpose pursued by the subsequent flow and transport modelling. In the present case, the two major aims are:

- Investigation of the applicability of the one-dimensional streamtube model SMART at the 'Testfeld Süd' by comparison with MT3D-IPD. As in most risk assessment analyses the longitudinal migration of contaminant plumes is sought, the applicability of SMART to simulate the short- or long-term behaviour of a plume, i.e. plume migration over short and long distances, is investigated (Chapter 7).
- Reactive transport modelling and transport process identification of degradable and non-degradable contaminants at the 'Testfeld Süd'. In contrast to degradable compounds, non-degradable contaminants migrated considerable distances at the 'Testfeld Süd', thus the simulation of plume development over short as well as long distances is important (Chapter 8).

These aims for the transport modelling imply the following requirements for the aquifer realizations to be generated:

- The longitudinal extension of the realizations should be large enough to account for long-term transport of non-degradable compounds.
- The orientation of the realizations should be according to the main groundwater flow direction in the 'Testfeld Süd'.

- The grid size should be fine enough to ensure a good resolution of the spatial heterogeneity of the facies distribution according to the determined correlation lengths. On the other hand, computation time should be kept within reasonable bounds, thus demanding for a not too fine grid size.

Therefore, the generated aquifer realizations have an extension of 800 m in y -direction (South-North), representing the mean groundwater flow direction. Due to the enormous computational effort required by the following MT3D-IPD transport simulations, the transversal extension (x -direction) is only 50 m and the third dimension is neglected. Grid sizes are chosen with 2 m in x -direction and 4 m in y -direction, resulting in 5000 cells in total.

As the extent of the aquifer realizations is 16-20 times the horizontal ranges (Table 6.2) in flow (y)-direction, but only 0.8-1.1 times the ranges in x -direction, many realizations fail to fulfil the given statistics. Therefore, a criterion for selecting realizations is required. The relative error of the simulated facies frequency f_k^* compared to the given, i.e. measured, facies frequency f_k is determined for each facies k .

$$err_k = \frac{f_k^* - f_k}{f_k} \cdot 100\% \quad (6.46)$$

From 200 generated realizations, only 8 realizations show a relative error below 5.5 % for each facies, another 7 had errors between 5.5 % and 10 % and further 9 realisations have errors of up to 15 %.

The weighted relative error is determined with

$$werr = \sum_{k=1}^3 f_k \cdot |err_k| \quad (6.47)$$

Only the 8 realizations (Table 6.3), that fulfil the error criterion of $|err_k| < 5.5\%$ for each facies, are used for the following flow and transport modelling.

In addition to the simulated frequency f^* , the spatial statistics of the eight selected realizations are determined by means of variogram analysis using the same variogram parameters as defined in Table 6.1. In contrast to the simulated frequency f^* , the quality of the variograms of the simulated realizations (referred to as 'simulated variograms') compared to the given variograms does not serve as a selection criterion, as the variogram analysis of 200 realizations, implying six variograms per realization, would be too time consuming.

Table 6.3 Statistics of the eight selected realizations that fulfil the error criterion of $|err_k| < 5.5\%$ (Given facies frequencies f_k : Facies G: 0.337, Facies Gm: 0.590, Facies S: 0.073).

Realiza- tion number	Simulated facies frequency $f^* [-]$			Relative facies error $err_k [\%]$			Weigh- ted error $werr$ [%]
	G	Gm	S	G	Gm	S	
n354	0.325	0.598	0.077	-3.56	1.39	5.21	2.40
n416	0.338	0.592	0.070	0.24	0.34	-3.84	0.56
n432	0.322	0.602	0.076	-4.39	2.07	3.56	2.96
n457	0.330	0.596	0.075	-2.20	0.98	2.19	1.48
n469	0.347	0.578	0.075	2.85	-2.03	3.29	2.40
n484	0.354	0.574	0.073	4.93	-2.75	-0.55	3.32
n508	0.323	0.607	0.071	-4.27	2.85	-3.29	3.36
n526	0.345	0.583	0.072	2.43	-1.25	-1.10	1.64
Mean	0.335	0.591	0.074	-0.50	0.20	0.68	2.27
St.dev.	0.012	0.012	0.002	3.61	2.01	3.35	0.98

St.dev.: standard deviation

The results of the variogram analysis of the eight selected realizations together with the input theoretical variograms are depicted in Figure 6.5. The spatial correlation of the facies 'G' is represented well by the eight realizations for both horizontal directions. Note, that the extension of the realization, that is orientated in south-north direction, is only 54 m in the direction of large range (112.5°, direction 1). Concerning direction 2, the variance of γ increases for larger values of h , probably due to the relatively small realization extension, which causes a small number of data pairs for large h and thus a relatively poor statistics. The variograms

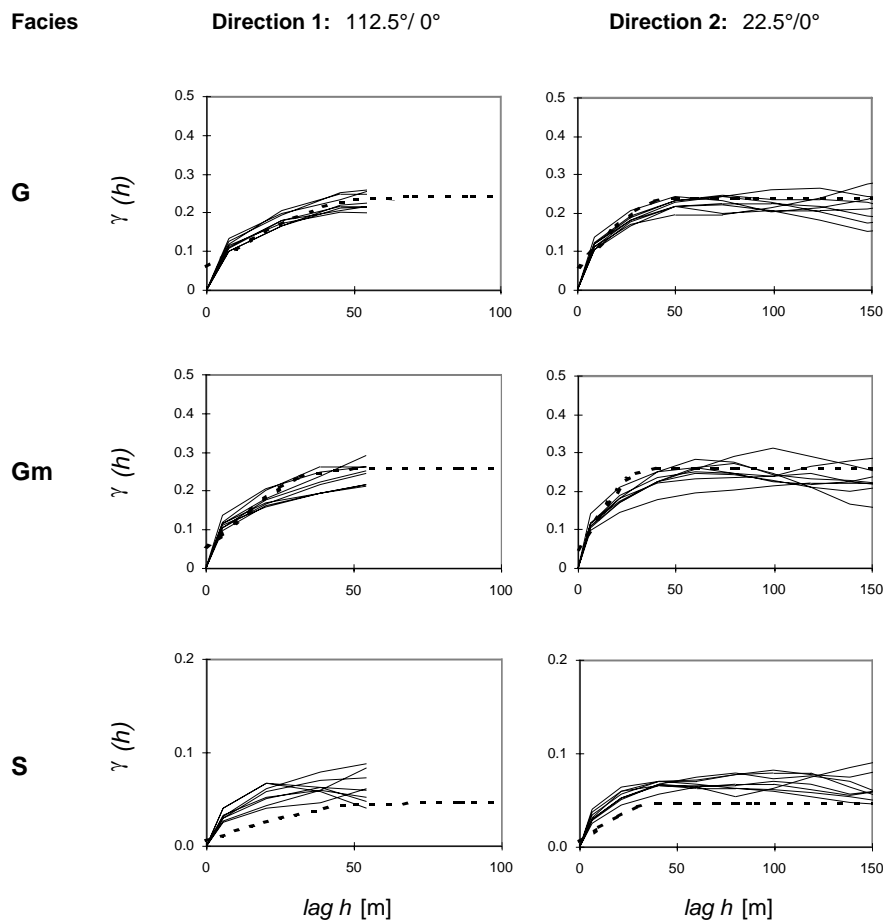


Figure 6.5 Variograms of the eight selected realizations ('simulated variograms', solid lines) compared to the given theoretical variograms (dashed lines) that served as input for the generation of the realizations.

of the facies 'Gm' of the eight realizations behave similar to those of facies 'G', however showing a slight decrease of the simulated variograms compared to the given ones. In contrast to facies 'Gm', the variograms of facies 'S' of the eight realizations indicate higher values of γ compared to the input variograms.

Summarizing, the selected realizations represent the frequencies and the spatial statistics of the facies types in the 'Testfeld Süd'. Other studies either neglect a control of the simulated realizations (Ruud et al. 2000) or allow relative errors of the simulated frequencies f^* of up to 12 % (Vert et al., 1999).

6.4 Flow characterization of the selected realizations

This section presents the flow modelling performed on the base of the selected eight realizations, which is the prerequisite for the following reactive transport simulations. Additionally, the ensemble variability of the heterogeneous flow fields is characterized by the breakthrough curves of a conservative compound. These are the base for the discussion of the variability of reactive breakthrough curves considering transport processes like kinetic sorption and biodegradation (Chapters 7 and 8).

MODFLOW (McDonald & Harbaugh, 1988) is used for the flow modelling of each realization. Figure 6.6 depicts the model set up with the flow and transport boundary conditions for one

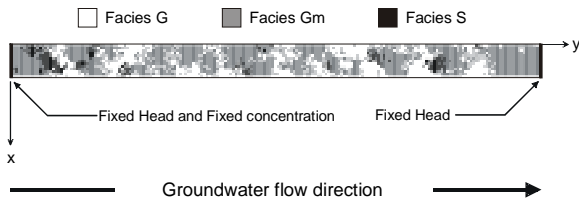


Figure 6.6 Set up of the flow and conservative transport modelling with boundary conditions. Shown is realization n432.

realization. On the southern and northern end (left and right side in Figure 6.6) of the model domain fixed head boundary conditions are set (218.2 m and 216.6 m), resulting in a mean groundwater gradient of 2 %. This corresponds to the observed groundwater gradient at the field site (Herfort, 2000).

As described in Section 5.1.2, for each facies the hydraulic conductivity was determined at a small scale by sieve analysis (Table 5.1). As the observed gradient as well as the flow velocity of 2 m d^{-1} determined by tracer tests (Bösel, 1999; Herfort, 2000) are regarded as more reliable than the small scale hydraulic conductivities, the hydraulic conductivities are fitted for each realization in a way, that (1) the ratios of K_f between the facies types remains constant for all realizations and (2) that the resulting flow velocity equals 2 m d^{-1} in all realizations. Based on these assumptions, flow is calculated for steady state conditions for each realizations.

For the simulation of conservative transport, the finite difference transport model MT3D (Zheng, 1990; Zheng & Wang, 1998) is used. To solve the governing transport equation, the upstream finite difference solver is used, that inevitably results in numerical dispersion. For the homogeneous case ($K_f = 1.356 \cdot 10^{-3} \text{ m s}^{-1}$), numerical dispersion is quantified by fitting an analytical solution to the conservative breakthrough curve at a distance of 800 m, yielding a dispersivity α_L of 0.9 m. Heterogeneous distributions of K_f are expected to lead to an even higher numerical dispersion. The dispersion-free method of characteristics (MOC) requires unjustifiable computational times and capacities and therefore is

not applied. Numerical dispersion induced by the upstream finite difference solver is thus accepted and dispersivities specified in MT3D are set to zero for all further transport simulations.

Conservative breakthrough curves are simulated assuming a contaminant source of constant concentration (fixed concentration condition) at the southern end of the model domain (Figure 6.6). At distances of 50, 100, 200, 400, 600 and 800 m breakthrough curves are calculated by applying equation (3.5) to calculate the mass flow rate at each considered control plane. Dividing by the volumetric discharge, the mean concentration at the control plane is obtained. Figure 6.7 depicts the breakthrough curves of the selected eight realizations at the aforementioned control planes.

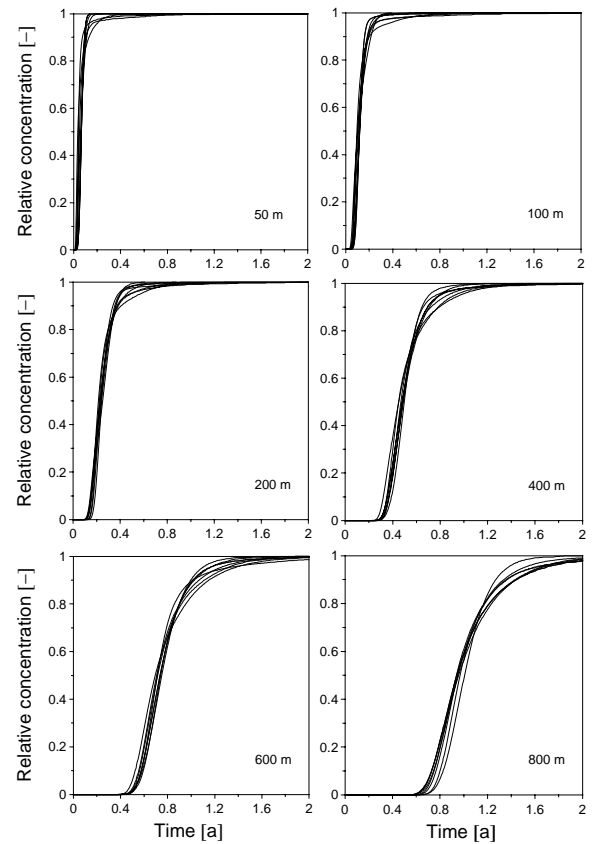


Figure 6.7 Conservative breakthrough curves of the selected realizations at different distances applying the upstream finite difference solver of MT3D.

It can be observed that due to the increasing hydraulic heterogeneity that is experienced by the migrating contaminant plume, the spread of the breakthrough curves increases. A measure

for the plume spreading and thus for macro-dispersion (see also Section 3.2) is the second central temporal moment $\mu_{2,t}$ which is given by (e.g. Ptak, 1993):

$$\mu_{2,t} = \frac{M_{2,t} - 2m_{1,t} \cdot M_{1,t} + m_{1,t}^2 \cdot M_{0,t}}{M_{0,t}} = m_{2,t} - m_{1,t}^2 \quad (6.48)$$

where $M_{n,t}$ is the n-th temporal moment and $m_{n,t}$ the n-th normalized temporal moment, defined as:

$$m_{n,t} = \frac{M_{n,t}}{M_{0,t}} = \frac{\int_0^\infty t^n C_w'(x, t) dt}{M_{0,t}} \quad (6.49)$$

where C_w' denotes the temporal derivation of C_w , as a continuous concentration input instead of a Dirac pulse is set as boundary condition.

Temporal moments are a common means to characterize transport of solutes (e.g. Kreft & Zuber, 1978; Valocchi, 1985; Selroos, 1995; Cirpka & Kitanidis, 2000b; Vanderborght & Vereecken, 2001). The second central temporal moment that is obtained from the breakthrough curves at the control planes (Figure 6.7) yields an estimate for the macro-dispersivity α_{mac} (Cirpka & Kitanidis, 2000b):

$$\alpha_{mac} = \frac{\mu_{2,t} v_x^2}{2x} \quad (6.50)$$

where v_x denotes the mean groundwater velocity in x -direction and x the travel distance. This macro-dispersion is an apparent quantity, as it is defined by an equation derived from the one-dimensional transport equation although the actual transport is multi-dimensional (Cirpka & Kitanidis, 2000b).

For the selected realizations, the second central temporal moment $\mu_{2,t}$ and the macro-dispersivity α_{mac} are calculated from the breakthrough curves at the different distances and the ensemble means are determined (Figure 6.8 and Figure 6.9). As the ensemble mean of $\mu_{2,t}$ increases with increasing distance, the mean macro-dispersivity α_{mac} also increases from

20 m to 33 m at distances of 50 and 800 m, respectively. However, the increase of α_{mac} is not as pronounced as the increase of $\mu_{2,t}$, because α_{mac} includes the transport distance. The standard deviation of $\mu_{2,t}$ (depicted as error bars in Figure 6.8) increases with increasing distance, which is not reflected by the standard deviations of the macro-dispersivity. The standard deviation of α_{mac} decreases to a transport distance of 400 m and is more or less constant from then on. The coefficient of variation, i.e. the standard deviation divided by the mean, is identical for $\mu_{2,t}$ and α_{mac} and decreases with increasing distance. These findings state an increase of macro-dispersion whereby the variances decrease with increasing transport distance. The

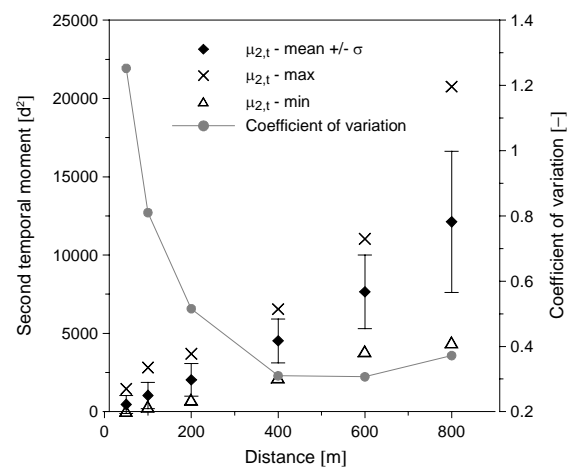


Figure 6.8 Ensemble mean of the second central temporal moment $\mu_{2,t}$ and its statistical parameters versus distance.

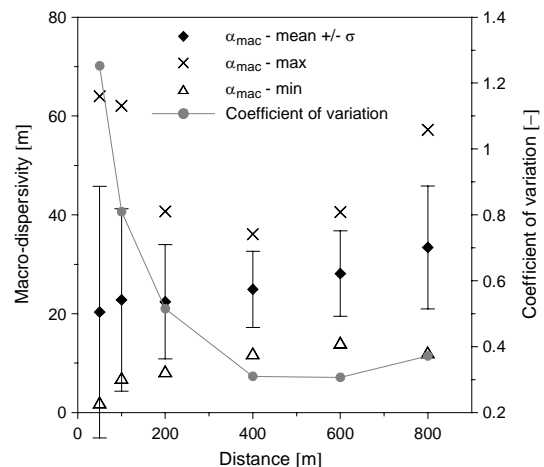


Figure 6.9 Ensemble mean and statistical parameters of the macro-dispersivity, as obtained from second central temporal moments.

slight increase of the variation coefficient at 800 m is probably caused by the small number of realizations considered.

6.5 Summary and conclusions

The geostatistical analysis at the 'Testfeld Süd' comprised the investigation of the spatial continuity of the variable 'facies', that is correlated to hydraulic and geochemical properties according to the improved facies approach (see Section 5.1.2).

An indicator based approach was performed to characterize the spatial correlation of the categorical variable 'facies'. Therefore, an indicator transformation of the facies data has been performed that were obtained from sieve analysis and also from soft information, i.e. drilling profiles. Three-dimensional directed experimental and theoretical variograms were determined for the three facies types, yielding horizontal ranges of 38 through 60 m and vertical ranges of 2 to 5 m. The vertical ranges are of reduced reliability, as they are difficult to determine in thin and stratified aquifers like the quaternary Neckar valley aquifer considered, that has a mean thickness of 2.7 m.

Based on the information of the variogram analysis, equally likely two-dimensional aquifer realizations were generated to provide the input for the subsequent Monte Carlo flow and transport simulations. The sequential indicator simulation algorithm for categorical variables (sisimpdf) by Deutsch & Journel (1992) was used for the generation of realizations. Due to the high computational effort required by the following transport simulations, high restrictions resulted with respect to the size of the realizations. The limited transversal extension of the realizations (50 m) leads to a high failure of the sisimpdf algorithm, requiring a criterion to select realizations. The relative error of the simulated frequency f_k^* of each facies k was

chosen as selection criterion. Demanding an error of $< 5.5\%$ for each facies, only eight of 200 realizations satisfied the criterion. For these eight realizations, the reproduced variograms were determined, showing a good agreement with the given input variograms.

The eight equally likely realizations provide the input for all further flow and transport simulations. As a basis for the following transport simulations, flow and conservative transport modelling was performed. Conservative breakthrough curves of the eight realizations were determined at different distances from a continuously emitting source. The breakthrough curves show an increase in the spread with increasing transport distance, resulting from an increase in macro-dispersion caused by the hydraulic heterogeneity. As a measure for plume spreading the second central temporal moments were determined for all realizations at different distances, showing an increase of the ensemble averaged moment with increasing transport distance. Macro-dispersivities were obtained from the second central temporal moments, based on the one-dimensional transport equation. Also the ensemble averaged macro-dispersivity increases with increasing transport distance. The variability between the realizations, i.e. the variation coefficient, of both the second central temporal moment and of the macro-dispersivity decreases with increasing transport distance. This means, that the longer the contaminant has experienced the heterogeneity of a realization (that has the same statistics as the other realizations) the more similar becomes the observed transport behaviour.

7 Comparing model approaches at field scale

7.1 Introduction

The quantification of natural attenuation at field scale and thus the identification of the dominating processes is the major aim of this thesis. To achieve this aim, a combined measuring and modelling approach (Chapter 4) is developed that tries to overcome the uncertainty due to aquifer heterogeneity in two ways: with respect to measuring by enlarging the sample volume (integrated mass flow rate approach) and in terms of modelling by stochastic approaches trying to determine the mean system behaviour and its variance. For the latter, a reliable and powerful transport modelling tool is necessary, that accounts for the relevant processes in a physically based way.

The aim of this chapter is the investigation of the applicability of the one-dimensional Lagrangian streamtube model SMART by comparing it to the three-dimensional Eulerian model MT3D-IPD. SMART provides a control plane based approach, as measured mass flow rates can serve directly as input for the one-dimensional model set up. Furthermore, it requires far less computational effort due to its one-dimensionality, which makes it favourable for the use in field applications. However, the one-dimensionality of SMART also brings about simplifications, which have to be investigated by comparison to a fully three-dimensional transport model. With respect to the considered transport processes, both model approaches account for kinetic sorption as diffusion limited transport of solutes into intraparticle pores.

The main differences between the two model approaches lie in the description and implementation of hydraulic and geochemical heterogeneity (for a detailed description of both approaches see Sections 5.2 and 5.3):

- Hydraulic heterogeneity:

In MT3D-IPD, hydraulic heterogeneity is accounted for by a non-uniform flow velocity field, obtained from flow simulations with MODFLOW. Heterogeneity is characterized by a spatially variable facies distribution, where a distinct hydraulic conductivity is assigned to each facies (see Section 5.1.2 and 6.4).

In SMART, hydraulic heterogeneity is accounted for by a heterogeneous distribution of travel times, i.e. the probability density function (pdf) of travel times. Flow simulations with MODFLOW and subsequent conservative transport simulations with MT3D are used to obtain the travel time distributions.

- Geochemical heterogeneity:

MT3D-IPD accounts for geochemical heterogeneity also by a spatially variable facies distribution. Each facies is characterized by a composition of different lithological components and grain size classes. For each combination of lithological component and grain size class, sorption parameters are assigned (see Section 5.1.2).

SMART does not allow for a spatial variation of facies types due to the Lagrangian idea of discretising the transport distance by travel time. Thus, a summarized facies type is used in SMART, that consists of all facies types weighted by their occurrence. The summarized facies

itself is described in SMART by several lithological components and grain size classes, just as in MT3D-IPD.

Potential differences of the model results of the two approaches emerge from the different descriptions of geochemical heterogeneity. Thus, main attention when comparing SMART with MT3D-IPD is paid to the following two questions:

1. How do results from SMART relate to results obtained by MT3D-IPD? Does the simplification with respect to the single effective facies lead to generally erroneous results?
2. Is there a distance from that on SMART is applicable? I.e., how many correlation lengths, that describe the geochemical heterogeneity, are necessary to achieve an average reactive transport behaviour?

In the following Section 7.2 the two model approaches will be compared using two-dimensional scenarios. After first considering geochemical homogeneous conditions, the influence of geochemical heterogeneity is investigated.

7.2 Two-dimensional case studies

Acenaphthene is chosen as model compound, as it is the dominant contaminant at the 'Testfeld Süd', with very high concentrations at the source and forming the longest plume detected at the site of at least 240 m length. Acenaphthene ($C_{12}H_{10}$) is a two-ring PAH with a solubility of 3.47 mg L^{-1} (at 25°C) and a K_{ow} of 4.33 (Verschueren, 1983). For hydrophobic contaminants of low solubility, sorption is expected to be an important process influencing transport. Sorption parameters have been determined in batch experiments using the lithological components found at the 'Testfeld Süd' and are summarized in Table 5.3. Acenaphthene is assumed to be recalcitrant (Zamfirescu, 2000), thus bio-

degradation is not included in the reactive transport simulations presented in this section. The constant concentration boundary of acenaphthene is set to $200 \mu\text{g L}^{-1}$ for all scenarios and is located at the upstream inflow boundary across the complete width of the realizations, i.e. 50 m (also compare Figure 6.6).

Three different scenarios are considered to compare the two models SMART and MT3D-IPD by simulating the reactive transport of acenaphthene:

1. For the simplest case, homogeneous conditions are defined for both, hydraulic and geochemical parameters (Section 7.2.1.1). Due to the homogeneous conditions, this scenario is identically defined in both model approaches, thus results should be equal.
2. Heterogeneous flow conditions are assumed, based on one generated aquifer realization of facies types (see Chapter 6). Geochemical properties are constant in space. Also for this type of scenario (Section 7.2.1.2) results of both approaches should not differ, as the hydraulic heterogeneity is considered in SMART by the pdf of travel times.

Additionally, the influence of two differently generated pdfs of travel times on the SMART results is investigated. On the one hand, the pdf of travel time is generated by using the upstream finite difference solver in MT3D (referred to as pdf-FD), thus the pdf is subject to numerical dispersion. On the other hand, the pdf of travel times is obtained from the dispersion-free particle tracking method in MPATH (referred to as pdf-PT).

3. In addition to hydraulic parameters, also geochemical properties vary in space, according to the facies approach (see Section 5.1.2). This is explicitly accounted for by MT3D-IPD. However, geochemical heterogeneity cannot be considered in SMART, thus one summarized facies has to be used to represent the geochemical heterogeneity. For this

scenario (Section 7.2.2) all eight realizations (see also Sections 6.3 and 6.4) are used to evaluate not only the behaviour of a single realization but also the ensemble averaged behaviour.

7.2.1 Model results for homogeneous geochemical conditions

7.2.1.1 Homogeneous hydraulic conditions

A simple scenario is chosen to demonstrate the accordance between the two model approaches. Therefore, the model set up is defined as simple as possible, while data from the 'Testfeld Süd' are used as far as possible. The extension of the model domain corresponds to that of the aquifer realizations used in the following sections, i.e. 800 m of longitudinal transport distance, 50 m width and 3.5 m aquifer thickness. The source width extends over the complete transverse realization extension, i.e. 50 m.

Consistent for both model approaches, hydraulic conductivity is set to $1.581 \cdot 10^{-3} \text{ m s}^{-1}$, the gradient is 0.002, the cross sectional area 175 m^2 , resulting in a volumetric discharge of approximately $5.6 \cdot 10^{-4} \text{ m}^3 \text{ s}^{-1}$. The effective porosity is set to 0.13, which corresponds to the results of the tracer test (Bösel, 1999) and drainage experiments conducted by Herfort (2000). The geo-chemical parameters are defined constant in space as follows: rock density is $2.73 \cdot 10^6 \text{ g m}^{-3}$, intraparticle porosity is 0.012, tortuosity factor is 59.0, K_{fr} is set to $3.29 \cdot 10^{-6} \text{ m}^3 \text{ g}^{-1}$, $1/n_{fr}$ to 1.0 and the grain radius of the single grain size class used is 0.015 m. A constant input concentration of 0.2 mg L^{-1} is assumed at the upgradient boundary.

The pdf of travel times required for SMART is obtained by simulating flow and conservative transport using MODFLOW and the upstream finite difference solver of MT3D, respectively.

The simulation period is 20 years, which does not yield a complete reactive breakthrough even

at short distances (Figure 7.1). Nevertheless, excellent correspondence of the SMART and MT3D-IPD results is observed for all distances and for all times. This finding is essential for all following simulations, as it confirms an equivalent implementation of the flow and transport processes in both approaches.

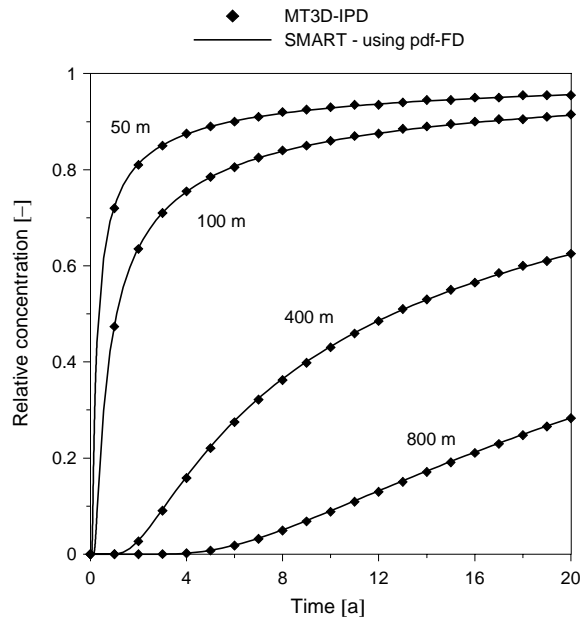


Figure 7.1 Reactive breakthrough curves of MT3D-IPD (diamonds) and SMART (solid line) for homogeneous conditions of both hydraulic and geochemical parameters.

7.2.1.2 Heterogeneous hydraulic conditions

Within this section, the influence of a heterogeneous flow field on the model results of SMART and MT3D-IPD is investigated. Geochemical parameters are again assumed constant in space.

Hydraulic heterogeneity will enhance (numerical) dispersion, as the upstream finite difference solver is used for MT3D-IPD. Using the alternative dispersion-free method of characteristics for MT3D-IPD would cause tremendously high computational times as already seen for conservative transport (see Section 6.4), thus results from MT3D-IPD will always be influenced by numerical dispersion. Quantifying the influence of the numerical dispersion due to hydraulic heterogeneity will help to understand the influence

of dispersion caused by geochemical heterogeneity (Section 7.2.2). Therefore, two different pdfs of travel time are used to simulate reactive transport with SMART: Firstly, the pdf obtained from simulating conservative transport with the upstream finite difference solver (pdf-FD), that incorporates (numerical) dispersion. Consequently, model results of both MT3D-IPD and SMART using the pdf-FD are influenced by numerical dispersion in the same way. Secondly, a pdf obtained from particle tracking (MPATH) is applied (pdf-PT), that is not subject to numerical dispersion.

Both SMART simulations are compared to MT3D-IPD (upstream finite difference solver), that is subject to numerical dispersion.

To assess the changing influence of numerical dispersion due to the hydraulic heterogeneity, the degree of heterogeneity is varied, as an increase of dispersion is expected when heterogeneity increases. Heterogeneity of hydraulic properties is described using one realization of the facies distribution (realization n354, see also Sections 6.3 and 6.4) and by assigning hydraulic conductivity values to each facies. Two scenarios are considered, representing “weaker” and “stronger” heterogeneity. For both scenarios mean hydraulic conductivities and thus flow rates are identical. For the first scenario, conductivity values of the facies ‘G’, ‘Gm’ and ‘S’ are set to $2.35 \cdot 10^{-2} \text{ m s}^{-1}$, $7.37 \cdot 10^{-4} \text{ m s}^{-1}$ and $4.82 \cdot 10^{-4} \text{ m s}^{-1}$, respectively. Assuming the same flow boundary conditions as in Section 7.2.1.1 yields a volumetric discharge of approximately $5.1 \cdot 10^{-4} \text{ m}^3 \text{ s}^{-1}$ and an effective K_f value of $1.44 \cdot 10^{-3} \text{ m s}^{-1}$. The standard deviation σ of the logarithm of K_f as a measure of heterogeneity is determined to 1.65.

For the second scenario, conductivity values of the facies ‘G’, ‘Gm’ and ‘S’ are set to $2.79 \cdot 10^{-1} \text{ m s}^{-1}$, $7.67 \cdot 10^{-4} \text{ m s}^{-1}$ and $6.97 \cdot 10^{-5} \text{ m s}^{-1}$, respectively. The same boundary conditions as for the first scenario are assumed, and a volumetric discharge of $5.1 \cdot 10^{-4} \text{ m}^3 \text{ s}^{-1}$ and

an effective K_f value of $1.44 \cdot 10^{-3} \text{ m s}^{-1}$ are obtained. σ of $\ln K_f$ is 2.96, indicating the higher degree of heterogeneity.

These two heterogeneous flow fields serve as model input directly for MT3D-IPD and for SMART by generating the two different types of pdfs of travel times obtained from MT3D (upstream finite difference solver; with numerical dispersion) and MPATH (particle tracking; no dispersion).

Geochemical parameters are constant in space and are the same as in Section 7.2.1.1. Again, a constant input concentration of 0.2 mg L^{-1} is assumed at the upgradient head boundary.

Figure 7.2 depicts the results for the first scenario considering “weaker” heterogeneity. Besides the breakthrough curves of MT3D-IPD, the breakthrough curves of both SMART simulations are plotted, using the pdf-FD and the pdf-PT. Breakthrough curves of MT3D-IPD and SMART using the pdf-FD show a perfect agreement for all distances and all times of the simulation period of 30 years. Both sets of breakthrough curves incorporate numerical dispersion, as for both the upstream finite difference solver was used. The excellent correspondence of the results confirms, that hydraulic heterogeneity is accounted for in both approaches in an equivalent way. The results of the SMART simulations using the pdf-PT emphasize this statement. For small distances (50 and 100 m), the accordance between SMART and MT3D-IPD is good, but with increasing distance a decreasing agreement of the breakthrough curves is observed. First breakthrough of MT3D-IPD at 400 and 800 m is earlier than the SMART breakthrough (not visible in the resolution of Figure 7.2), but for times larger than 0.6 and 1.9 years SMART breakthrough becomes faster compared to MT3D-IPD at distances of 400 and 800 m, respectively. The largest deviation between SMART and MT3D-IPD is observed at 800 m after 30 years, showing a relative difference of 4.2 %.

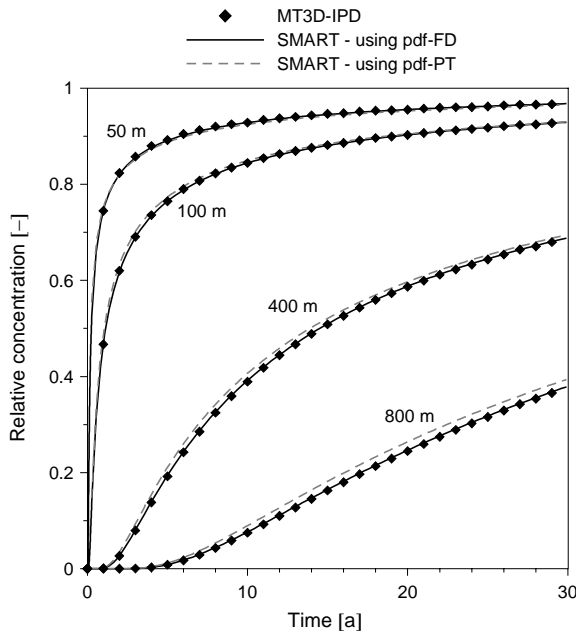


Figure 7.2 Reactive breakthrough curves of MT3D-IPD and SMART for weak heterogeneous flow conditions ($\sigma_{ln K_f}$: 1.65) and homogeneous geochemical conditions.

As the results of SMART using the pdf-FD are in perfect agreement to those of MT3D-IPD, it can be stated, that the differences between SMART (using the pdf-PT) and MT3D-IPD are caused by numerical dispersion, which MT3D-IPD is subject to.

These findings are confirmed by the results of the second scenario, considering a strong hydraulic heterogeneity (Figure 7.3). Again, breakthrough curves of MT3D-IPD and SMART, using the pdf-FD, correspond perfectly well for all distances and times. However, differences between MT3D-IPD and SMART, using the pdf-PT, increase compared to the first scenario. Generally, the same behaviour as in the first scenario can be observed when comparing these two sets of breakthrough curves. For small distances (50 and 100 m), a good agreement of the two breakthrough curves is observed. For larger distances (400 and 800 m), MT3D-IPD breakthrough is earlier than SMART breakthrough (again not visible in the resolution of Figure 7.3), but SMART breakthrough becomes faster at times larger than 1 and 1.5 years for distances of 400 and 800 m, respectively. The largest difference between SMART and MT3D-IPD is

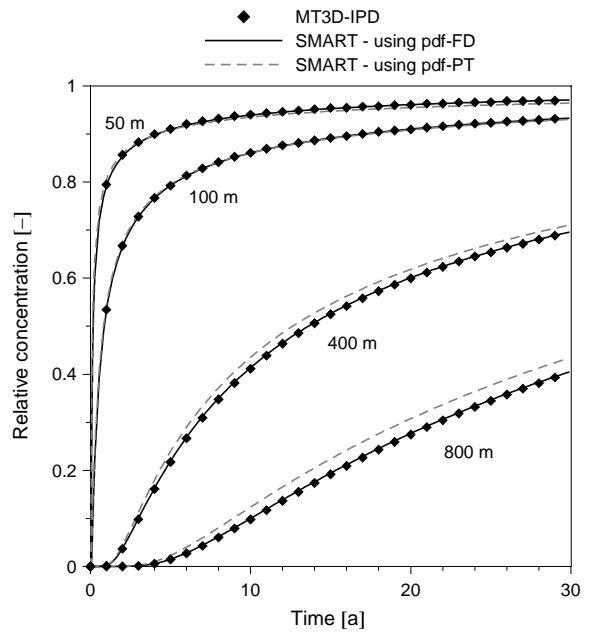


Figure 7.3 Reactive breakthrough curves of MT3D-IPD and SMART for strong heterogeneous flow conditions ($\sigma_{ln K_f}$: 2.96) and homogeneous geochemical conditions.

again observed at 800 m after 30 years with 7.2 %. As it is assumed, that the deviation between SMART using the pdf-PT and MT3D-IPD is caused by numerical dispersion, the increase of numerical dispersion in scenario 2 as compared to scenario 1 is due to the stronger hydraulic heterogeneity of scenario 2.

In the following, the transport simulations in SMART will be performed using the pdf obtained by the upstream finite difference solver of MT3D (pdf-FD, with dispersion), as it is then fully comparable to the results of MT3D-IPD. However, with respect to numerical dispersion, the pdf obtained from particle tracking is the correct one. Thus, for the sake of model comparison, numerical dispersion is accepted here.

7.2.2 Model results for heterogeneous geochemical conditions

Besides a heterogeneous flow field, also a heterogeneous distribution of geochemical parameters is assumed in the transport simulations presented in this section. Generated aquifer realizations, representing the geostatistical charac-

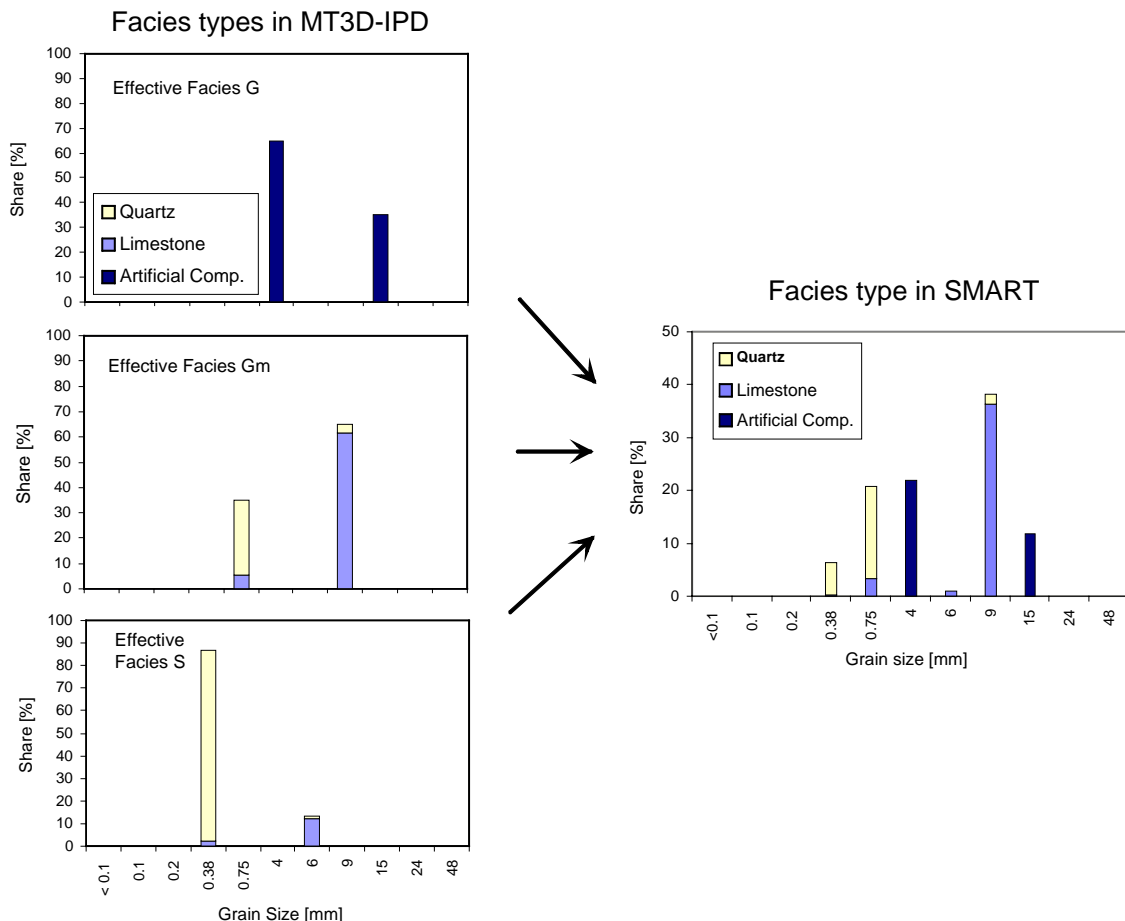


Figure 7.4 The three facies types 'G', 'Gm' and 'S' used in MT3D-IPD with their lithological composition (left hand side) and the summarized facies with lithological composition used in SMART (right hand side).

teristics of the facies distribution at the 'Testfeld Süd', are used to assign both hydraulic and geochemical parameters (see Section 5.1.2 and 6.3).

Eight aquifer realizations are used for the Monte Carlo simulations with parameter values measured at the 'Testfeld Süd'. The flow simulations are performed as described in Section 6.4. A mean groundwater flow velocity of 2 m d^{-1} results from the flow simulations for each realization, which corresponds to the observed flow velocity measured by the tracer test (Bösel, 1999; Herfort, 2000).

In MT3D-IPD, geochemical parameters are assigned to each lithological component of each of the three facies types, as they were determined in laboratory experiments and summarized in Table 5.3. Thus, geochemical heterogeneity is introduced by spatially varying facies types. In contrast to that, SMART accounts only for one

facies type that consists of all three facies according to their occurrence found at the site. In SMART, sorption parameters are then assigned to the lithological components. The three facies types used in MT3D-IPD and the summarized facies used in SMART are shown in Figure 7.4.

For eight realizations, reactive transport ofacenaphthene is simulated with MT3D-IPD and SMART (Peter et al., in print) assuming a source width of 50 m, according to the transverse extension of the realizations. Due to the enormous computational effort of MT3D-IPD (8-17 days of CPU time on a workstation HP J5000 for a simulation period of 30 years for one realization), the amount of realizations is kept small and the simulation period is limited to 30 years.

Looking at a single realization, differences between simulation results of MT3D-IPD and SMART are expected to be high, especially at

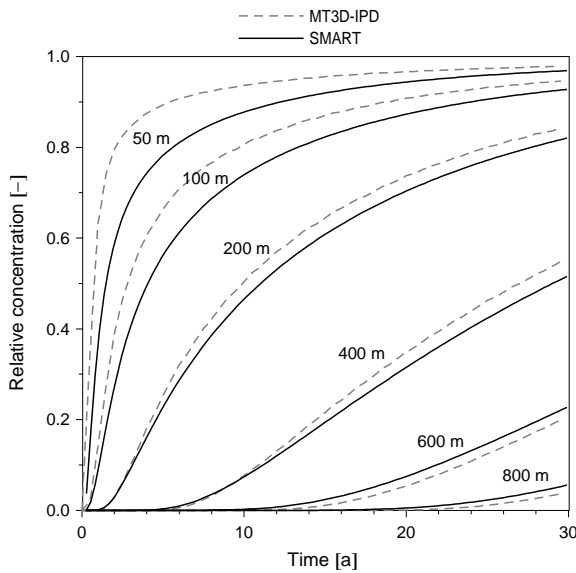


Figure 7.5 Comparison of model results for a single realization (*n*432): Reactive breakthrough curves at different distances using MT3D-IPD (dashed lines) and SMART (solid lines) (Peter et al., *in print*).

small transport distances, i.e. distances that are less than the correlation length of geochemical properties. In Figure 7.5 relative breakthrough curves of both model approaches are shown at different transport distances for one realization.

For transport distances of 50 m and 100 m, SMART leads to a higher retardation of acenaphthene than MT3D-IPD. This is due to the spatial distribution of the different facies types, which is considered in MT3D-IPD but not in SMART. Figure 7.6 shows the cumulative proportions of facies types with travel distance for this realization. In comparison to the mean

facies proportion, which is taken into account in SMART (horizontal lines in Figure 7.6), the spatially varying proportion of the highly sorptive facies type 'G' (light grey in Figure 7.6) is significantly smaller than the mean share at distances up to 200 m. This causes the lower retardation in MT3D-IPD compared to SMART in the first 200 m. With increasing transport distance and consequently decreasing deviations between the facies proportions of both model approaches, the differences in the simulated breakthrough curves decrease.

However, at larger distances (600 and 800 m), acenaphthene shows a stronger retardation using MT3D-IPD compared to SMART. This might be due to numerical dispersion, that is caused by geochemical heterogeneity and that is thus not considered in SMART. Numerical dispersion leads to an earlier first arrival of the MT3D-IPD breakthrough curve (not visible in the resolution of Figure 7.5) and to an increased retardation for later arrival times.

To compare the results of both model approaches in a stochastic way, ensemble averaged breakthrough curves and their standard deviations are determined. The ensemble averaged breakthrough curves are obtained by simulating the reactive transport for each realization and subsequently averaging over all realizations. This is performed for both model approaches.

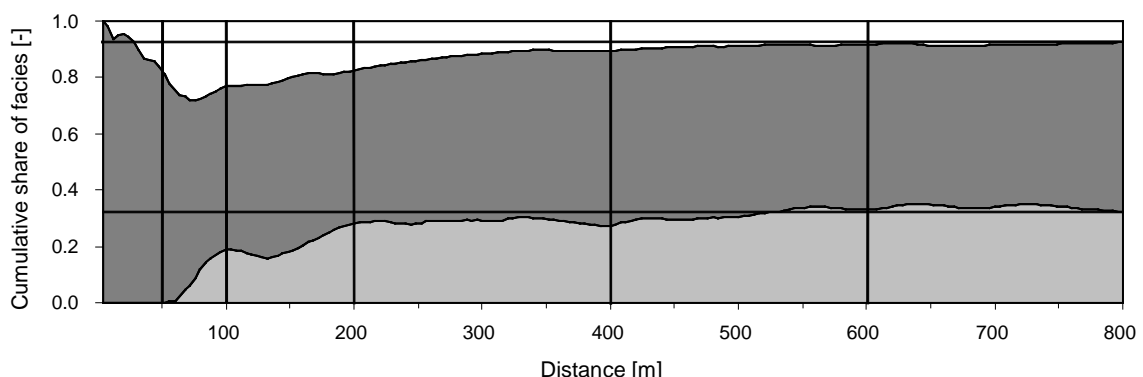


Figure 7.6 Cumulative proportions of facies types with travel distance for realization *n*432. The horizontal lines mark the constant share of facies types in SMART, while the vertical lines denote the distances at which the breakthrough curves are shown in Figure 7.5. (white = facies 'S'; dark grey = facies 'Gm'; light grey = facies 'G') (Peter et al., *in print*).

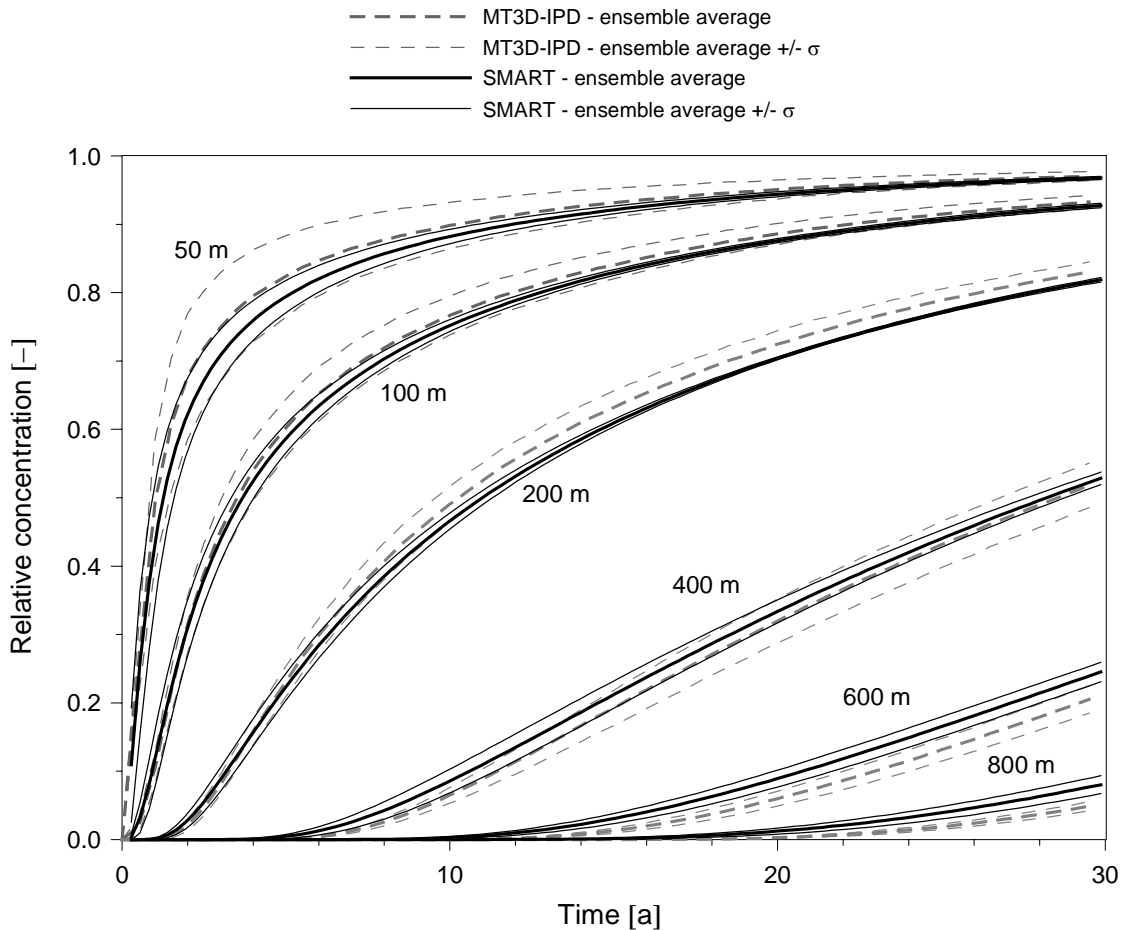


Figure 7.7 Comparison of model results for all realizations: dashed lines represent the breakthrough curves at different distances simulated with MT3D-IPD, solid lines show the corresponding SMART results. Bold lines denote the ensemble average over all realizations, thin lines denote the ensemble average \pm one standard deviation of relative concentration (Peter et al., in print).

Model results for the realization ensemble (Figure 7.7) show some different characteristics than the results of a single realization. Two major observations can be made:

- (1) The differences between the mean breakthrough curves (bold lines in Figure 7.7) decrease with increasing travel distance. This is caused by the same effect as already observed for the single realization. The longer acenaphthene has migrated through the aquifer, the more it experiences the mean aquifer composition. When averaging over all realizations, this effect is intensified, as in the ensemble average the mean aquifer composition is experienced even for short transport distances. This is valid for distances of up to 400 m. From then on

the differences seem to increase again. There are two possible explanations:

- (a) Due to the high computational effort, complete breakthrough curves were not simulated. It could be presumed, that with increasing time the breakthrough curves might become more similar, like the 400 m breakthrough curve at 30 years.
- (b) As discussed before, the upstream finite difference solver, used in MT3D-IPD, produces numerical dispersion. Whereas numerical dispersion due to hydraulic heterogeneity is accounted for in both approaches (if the pdf-FD for SMART is used), numerical dispersion caused by geochemical heterogeneity occurs only in MT3D-IPD. Again, numerical dispersion

leads to an earlier first arrival of the MT3D-IPD breakthrough curve (not visible in the resolution of Figure 7.7) and to an increased retardation for later arrival times.

- (2) The maximum standard deviation of the realization ensemble shows a decreasing tendency with increasing travel distances for both model approaches. This is expected, as with increasing travel distance the contaminant plume has increasingly experienced the mean aquifer composition in each realization. Because MT3D-IPD also considers the geochemical heterogeneity, the variance of the realization ensemble is higher in this case than the variance of the SMART ensemble.

These findings show, that the one-dimensional streamtube model SMART is able to appropriately represent the mean transport behaviour for travel distances larger than 100 m, which corresponds to approximately two to three correlation lengths at the 'Testfeld Süd'. The effect of not considering (numerical) dispersion caused by geochemical heterogeneity leads to deviations in comparison to MT3D-IPD for large transport distances. However the SMART results are conservative with respect to risk assessment, i.e. breakthrough is faster in SMART than in MT3D-IPD.

For transport distances less than 100 m, SMART shows a good correspondence with the MT3D-IPD results for large travel times. After nine years, the relative deviation between SMART and MT3D-IPD results is $\leq 2\%$ at distances of 50 and 100 m. After 17 and 21 years, the relative error is below 1 % at transport distances of 50 and 100 m, respectively. Also the first part of the rising limb up to a relative concentration of 0.5 is in good agreement comparing both model approaches. Thus, SMART is capable to simulate mean plume migration even at short distances, especially when the first arrival or the long-term plume behaviour is of interest.

The results discussed apply for the conditions assumed in the presented scenarios. Besides the correlation lengths of the facies types, that characterize the hydraulic and geochemical heterogeneity, the extent of the source zone is of major importance when investigating the characteristic length from that on SMART is applicable for simulating reactive transport in heterogeneous geochemical media. This is related to the question of ergodicity of transport parameters. Non-ergodic conditions are assumed to prevail if the source zone is small, i.e. of the same order of magnitude as the correlation length. Dagan (1989) states, that ergodicity of a variable u can generally be proven by analysing the space average \bar{u} over a volume or area and its variance σ_u^2 . The assumption of ergodicity holds, if σ_u^2 tends to zero, i.e. the space average \bar{u} approaches the expected value and ensemble average $\langle u \rangle$.

Several authors investigated conservative transport (e.g. Kitanidis, 1988; Dagan, 1991; Zhang et al., 1996; Zhang, 1997) and reactive transport (e.g. Selroos & Cvetkovic, 1994; Selroos, 1995; Fiori & Bellin, 1999) under non-ergodic conditions by deriving analytical expressions for the first and second spatial and/or temporal moments of concentration or mass flux and their ensemble variances. All analytical expressions were derived for instantaneous injections and weak heterogeneous hydraulic conditions, i.e. $\sigma_{\ln K_f}^2 \leq 1.0$. For larger variances of $\ln K_f$ the first-order approximation used to derive the analytical formulae for the first and second moments was demonstrated to deviate from the solutions obtained by numerical Monte Carlo simulations (e.g. Selroos & Cvetkovic, 1994; Selroos, 1995; Zhang, 1997).

Generally, the following observations were made concerning the relevance of the source size for the ergodicity of concentration or mass flux. Dagan (1991) and Zhang et al. (1996) investigated the influence of dispersivity under non-ergodic conditions by the aid of the second

spatial moment of concentration and stated, that dispersivities reach the ergodic value, if the initial lateral extension of the source is at least about two orders of magnitude larger than the correlation length. In contrast to the mentioned studies on conservative transport, Fiori & Bellin (1999) and Selroos (1995) investigated the influence of sorption reactions on the ergodicity of transport. They found that both equilibrium and kinetic sorption reduces the size of the initial source required to meet ergodic conditions. With increasing strength of the sorption reaction, ergodic conditions are achieved for progressively smaller source sizes. Fiori & Bellin (1999) stated, that for a kinetically sorbing solute the initial source size required to obtain ergodic conditions is about one order of magnitude smaller than that required for conservative solutes.

For the scenarios presented here, analytical expressions for the first and second temporal or spatial moments for non-ergodic conditions, that would be comparable with the numerical Monte Carlo simulations, are not available. This is due to several reasons: in contrast to the studies presented, a continuous contaminant release into the aquifer was assumed that is heterogeneous in both respects, hydraulically and geochemically. These heterogeneities that are described by a facies approach showing different and anisotropic correlation lengths for the individual facies types cannot be represented by a single covariance function as required by the first-order approximations to derive analytical solutions for the moments. Furthermore, in the presented scenarios the variance of $\ln K_f$ exceeds 1.0 which is the required limit for the applicability of the first-order approximation. Additionally, all analytical formulations in the literature that include sorption processes do not consider non-linear kinetic sorption in general, and intra-particle diffusion in particular. Therefore, the investigation of ergodicity by the means of analytically derived spatial or temporal moments of concentration or mass flux is not possible for the scenarios presented in this work.

Thus, instead of analysing the moments of the dependent variable concentration, the moments of facies frequencies are analysed in the following for different source sizes. As the hydraulic and geochemical parameters are directly correlated to the facies distribution, ergodicity of hydraulic and geochemical parameters is connected to ergodicity of facies frequencies. This might give further evidence to ergodic conditions with respect to concentration and thus plume development.

To analyse ergodicity of facies frequencies, the spatial average of the frequency of each facies is compared to the expected frequency of the respective facies as suggested by Dagan (1989). This is performed for different source sizes, i.e. different realization extents, as the source width equals the lateral extent of the realization. Besides the realizations with a lateral extent of 50 m that are used for the Monte Carlo simulations presented above, four further realization ensembles are generated with lateral realization extensions and thus source extensions of 20 m, 100 m, 200 m and 800 m. Each realization ensemble consists of eight realizations which is consistent with the realization ensemble for 50 m used above.

In Figure 7.8 the space averaged facies frequencies \bar{f} normalized by the expected facies frequencies $\langle f \rangle$ are plotted versus travel distance, i.e. versus an increasing averaging area, for the five different source widths. The standard deviation of the space average is indicated by error bars in Figure 7.8. It can be generally observed that for all source widths the space average approaches the expected value with increasing travel distance. Thus, the standard deviations tends towards zero and ergodic conditions prevail. With increasing source width progressively less travel distance is required for $\bar{f}/\langle f \rangle$ to equal unity. For a source width of 20 m, which corresponds to approximately half a correlation length, ergodicity is obtained after 700 m of travel distance. Assuming a lateral source extent

of 100 m, $\bar{f}/\langle f \rangle$ tends to unity for travel distances of approximately 400 m. For a large source of 800 m width, ergodicity would prevail almost from the first meters of travel distance.

In Figure 7.9 the variance of f for the facies Gm is depicted versus source width for different travel distances x . It can be seen that travel distances of at least 300 m are necessary to obtain ergodic conditions for source widths that are smaller than 200 m.

Comparing the facies frequencies for a source width of 50 m in Figure 7.8 with the ensemble

results of the reactive transport modelling in Figure 7.7, it is observed, that the simulation results of the model approaches SMART and MT3D-IPD converge at approximately 100 m of travel distance. Ergodicity of facies frequencies prevails however for transport distances larger than 400 m, which supports the statement from Fiori & Bellin (1999) that reactive transport leads to ergodic conditions earlier than conservative transport.

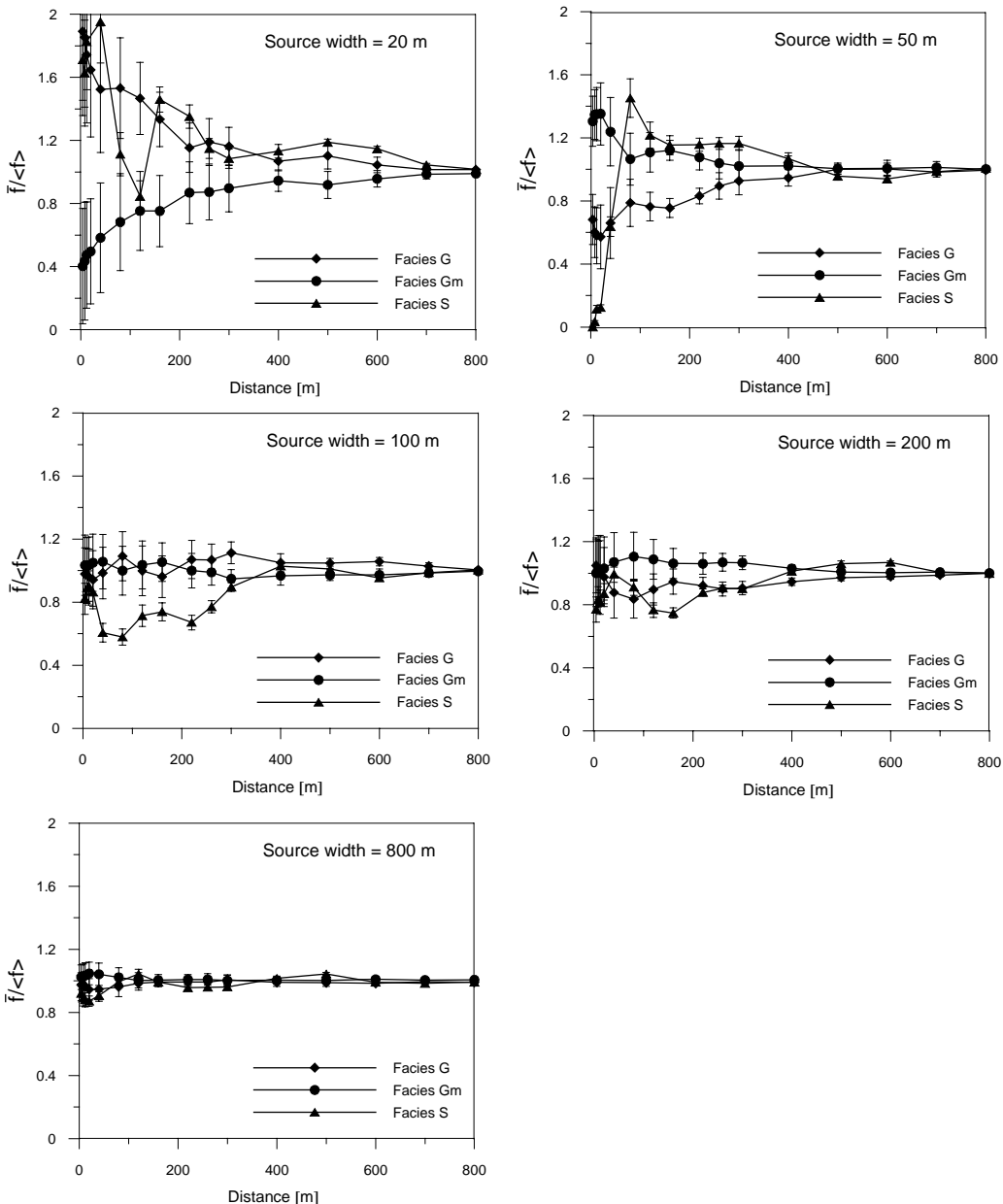


Figure 7.8 Space averaged facies frequencies normalized by the expected facies frequencies versus travel distance for different source widths. Error bars indicate one standard deviation of the space averaged facies frequencies.

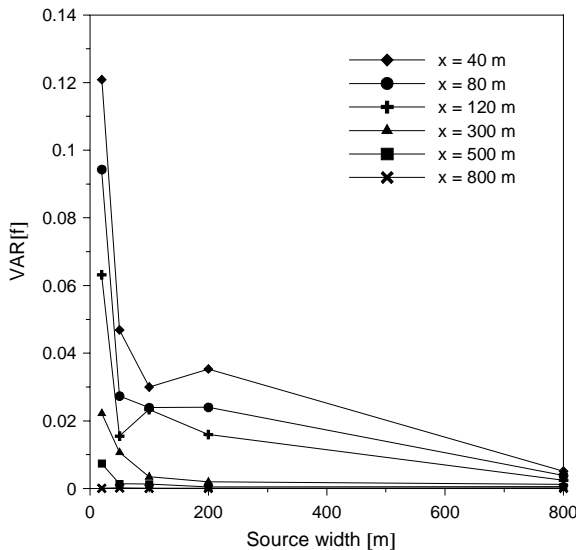


Figure 7.9 Variance of space averaged facies frequency for facies Gm versus source width for different travel distances.

The studies presented show the importance of the source size relative to the correlation length and its influence on the transport of reactive compounds.

7.3 Summary and outlook

In this chapter the applicability of the one-dimensional Lagrangian streamtube model SMART was investigated by comparing it to the three-dimensional Eulerian model MT3D-IPD. Reactive transport of acenaphthene was simulated with both models, describing kinetic sorption as intraparticle diffusion. As the Lagrangian approach neglects the heterogeneity of geochemical parameters, the aim of this chapter was to assess the influence of the geochemical heterogeneity on model predictions at field scale. Parameter values were taken from the 'Testfeld Süd', i.e. aquifer realizations generated according to the statistical properties of the facies observed in the field as well as measured values for hydraulic and geochemical properties were used.

First, homogeneous geochemical conditions were assumed to investigate whether both model approaches yield identical results for identically

defined scenarios. Therefore, scenarios considering homogeneous and heterogeneous hydraulic conditions were simulated, whereas geochemical parameters were assumed spatially constant. For both scenario types, the model results of the two approaches showed perfect agreement, if a pdf of travel times was used for SMART, that was obtained using the upstream finite difference solver of MT3D. Thus, numerical dispersion caused by hydraulic heterogeneity was considered in both model approaches.

Assuming both hydraulic and geochemical heterogeneity and looking at a single realization, SMART is expected to lead to erroneous results for small transport distances, i.e. distances less than the correlation length of the geochemical heterogeneity. This was confirmed by analysing breakthrough curves of both model approaches for a single realization. The difference of facies types experienced by the plume within the first 100 to 200 m using MT3D-IPD, compared to a spatially constant facies in SMART causes different results. With increasing transport distance and thus decreasing deviation between the facies proportions of both model approaches, the differences in the simulated breakthrough curves decrease.

If instead of a single realization the mean behaviour of plume migration is investigated by means of Monte Carlo simulations, the ensemble averages of both approaches agree well, especially for long transport distances. Also for short transport distances and travel times larger than nine years, the relative deviation between both approaches is below 2 %. Transport distances larger than 600 m reveal a slight increase in the deviation between the mean breakthrough curves of both approaches, probably caused by numerical dispersion due to geochemical heterogeneity that only MT3D-IPD is subject to. Furthermore, the variances of the breakthrough curves obtained by MT3D-IPD are higher compared to those of the SMART breakthrough

curves, due to the geochemical heterogeneity considered in MT3D-IPD.

To investigate the influence of the source size on the applicability of SMART, ergodicity of facies frequencies was analysed for different ensembles of realizations with different source widths. It was shown, that for source zones with a larger transverse extent ergodicity of facies frequencies, to which hydraulic and geochemical parameters are related to, prevails for shorter transport distances than for small source widths.

Based on these results, it can be stated, that SMART is applicable to predict the mean plume behaviour at field scale, even for geochemically heterogeneous conditions. The distance from which on SMART is applicable however depends on both the correlation length and the size of the source zone. Furthermore, the variance of the outcome, i.e. the uncertainty due to insufficient knowledge of the spatial parameter distribution (in this case facies types with corresponding hydraulic and geochemical parameters), will be underestimated by SMART as it neglects the geochemical heterogeneity.

SMART has several advantages compared to MT3D-IPD. It is free of numerical dispersion caused by hydraulic heterogeneity, if a particle tracking algorithm is used to generate the pdf of travel times and numerical dispersion caused by geochemical heterogeneity does not occur. “True” hydrodynamical dispersion can be implicitly accounted for via the pdf of travel times. Furthermore, the computational effort is significantly smaller for SMART than for MT3D-IPD, in the case of the simulations presented by a factor of eight to ten. Thus, it is unreasonable to use MT3D-IPD for simulations at field scale due to its enormous computational effort. Another advantage of SMART is that it requires less detailed site investigations, as its integral approach allows for integrally measured parameter values, e.g. mass flow rates across control planes or travel time distributions measured by tracer tests.

In the past, also other authors used streamtube model approaches to simulate contaminant transport and compared the results to Eulerian transport models. Cirpka & Kitanidis (2000a) applied a streamtube model approach to simulate multi-component reactive transport by using a corrected pdf of travel times that incorporates longitudinal dispersion and found good agreement with two-dimensional simulation results obtained from a Eulerian transport model. Also Ginn (2001) and Ginn et al. (2001) compared a streamtube model that accounts for intra-streamtube dispersion, i.e. longitudinal dispersion, to a high-resolution Eulerian model by simulating the reactive multi-component transport of a column experiment. They found that both model approaches were capable to reproduce the reactive transport behaviour observed in the experiment.

Future work with the aim to consolidate the applicability of SMART might comprise the following aspects: firstly, further scenarios might be performed in comparison to MT3D-IPD, testing e.g. the influence of different correlation lengths of the geochemical heterogeneity as well as the influence of the third (vertical) dimension. Three-dimensional scenarios as well as scenarios with different correlation lengths could not be performed within this thesis, as computational times would have been in the order of several months for a single realization. Within the next couple of years, computational facilities might improve sufficiently so that these scenarios as well as the simulation of a larger number of realizations become reasonable.

Secondly, efforts might have to be made with respect to the representation of dispersion within SMART. So far, SMART explicitly accounts for macro-dispersion caused by different flow velocities by a non-uniform pdf of travel times. Local-scale dispersion can be accounted for by externally simulating advective-dispersive transport of a conservative tracer, from which the pdf of travel times is then

obtained. However, further dispersion due to reactive processes and transverse dispersion cannot be accounted for in SMART. Other authors also focused on the problem of representing dispersion within streamtube models. As mentioned before, Cirpka & Kitanidis (2000a) and Ginn (2001) implemented longitudinal dispersion into their streamtube models however neglected transverse dispersion, i.e. dispersion between streamtubes. Mishra & Gutjahr (1999) introduced longitudinal and transverse dispersion into a Lagrangian framework by describing the probability of a particle to remain or to move to the adjacent streamline, depending on the defined transverse dispersion. Also Fiori & Dagan (2000) considered local-scale (longitudinal and transverse) dispersion within a Lagrangian framework and determined concentration fluctuations (i.e. concentration variance) influenced by local-scale dispersion by applying a first-order approximation.

Similar further developments of SMART would improve the model predictions with respect to plume spreading, however requiring a streamtube ensemble instead of a single streamtube to allow for a high enough resolution of the transverse dispersion. This would enormously increase the computational effort, decreasing the advantage of SMART compared to Eulerian approaches like MT3D-IPD. Thus, the applicability of SMART as it is might be justified for cases where the mean plume behaviour has to be predicted based on the simulation of physically founded processes within a reasonable amount of computation time.

8 Modelling natural attenuation at the 'Testfeld Süd'

8.1 Introduction

In the present chapter the application of the developed combined measuring and modelling approach is presented for the 'Testfeld Süd'. Therefore, two field campaigns were carried out to measure integral mass flow rates at two control planes at the 'Testfeld Süd', resulting in mean concentrations and mass flow rates across the control planes for BTEX, PAH and inorganic compounds (Holder, 1999; Bockelmann et al., 2001; Bockelmann, subm.). For a third control plane, contaminant mass flow rates are estimated using point concentration data and the relevant hydraulic parameter values.

With the information of the measured mass flow rate at the upgradient control plane as boundary condition, the mean plume development of two target compounds is simulated by a Monte Carlo approach using the streamtube model SMART.

In Section 8.2 the acenaphthene plume at the 'Testfeld Süd' is simulated accounting for kinetic sorption. As the initial conditions as well as the contamination time are not known at the site, both are inversely estimated by comparing simulated mass flow rates at the downgradient control planes to the measured ones.

In Section 8.3 plume migration of p-xylene is modelled under consideration of kinetic sorption and biodegradation. Biodegradation rates are inversely determined also by comparing simulated mass flow rates at the downgradient control planes to the measured ones.

8.2 Modelling the fate of acenaphthene

At the 'Testfeld Süd' acenaphthene represents one of the most recalcitrant compounds as it forms the longest plume observed at the site. In the most downgradient well (NT01) with a distance of approximately 230 m from the presumed source, acenaphthene concentrations of $180 \mu\text{g L}^{-1}$ are found. Besides acenaphthene, also heterocyclic aromatic hydrocarbons are found in considerable concentrations at these distances ($66 \mu\text{g L}^{-1}$ sum of heterocycles found, Zamfirescu, 2000), whereas the concentrations of BTEX compounds are below $0.5 \mu\text{g L}^{-1}$.

Little is known about the degradation potential of acenaphthene. Zamfirescu (2000) assumes that acenaphthene reveals a limited degradability at the 'Testfeld Süd' in the presence of naphthalene. A cometabolic degradation process might occur between the two compounds, as stated by Selifonov et al. (1998). In the absence of naphthalene however, acenaphthene seems to be recalcitrant. These statements are confirmed by observations at the 'Testfeld Süd' where decreasing concentrations of acenaphthene are found only in the presence of naphthalene. Where naphthalene has been depleted, degradation of acenaphthene stops, i.e. only a slight decrease in concentration and mass flow rate is observed.

As the assumption of cometabolic degradation of acenaphthene in the presence of naphthalene is difficult to prove, acenaphthene plume mi-

gration is simulated downstream of control plane CP0 (Figure 8.1), where naphthalene is almost completely depleted (concentrations below $1 \mu\text{g L}^{-1}$) and thus degradation of acenaphthene can be neglected.

8.2.1 Model domain and model set-up

Plume development of acenaphthene is simulated starting with a pristine aquifer. The contaminant source is assumed to be located around B49, B55 and B56 (Figure 8.1). As mentioned before, the model domain starts at CP0, where naphthalene is depleted and cometabolic degradation of acenaphthene can be neglected.

For simulating the mean plume development, SMART is used within a Monte Carlo approach. A single, one-dimensional streamtube is used to represent the model domain along the flow paths from CP0 to the first and second control plane, CP1 and CP2.

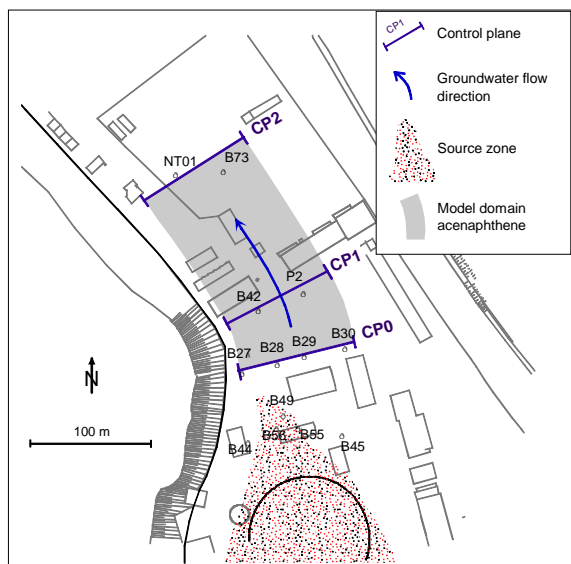


Figure 8.1 Field site ‘Testfeld Süd’ with model domain, control planes and wells where mass flow rates of acenaphthene are determined.

Based on the flow simulations of the eight realizations (see Section 6.3 and 6.4), two sets of pdfs of travel times were generated by simulating conservative transport with MT3D between CP0 and CP1 (50 m), and between CP0 and CP2 (180 m). These two sets of pdfs of travel time

are used in SMART to represent the heterogeneous hydraulic conditions observed at the site, according to the geostatistical characteristics of the facies, to which hydraulic properties are correlated (see Section 5.1.2).

Geochemical properties are described according to the summarized facies, that consists of the three facies identified at the site (Figure 7.4). Sorption parameters of the lithological components used are listed in Table 5.3.

Initial and boundary conditions for the transport simulations are difficult to determine. As initial condition, a pristine aquifer is chosen, assuming that the aquifer downstream of the contaminant source, located around B49, B55 and B56, was not affected by further contaminant sources. This is a crucial assumption which is hard to prove for the extremely complex contamination situation of the site (see also Chapter 2).

Hence, one goal of the simulation of this site is to estimate the contamination time assuming an emitting source of both acenaphthene and naphthalene near B49, B55 and B56. Only up to CP0, where naphthalene is depleted, degradation of acenaphthene is assumed to occur. Thus, a constant concentration boundary for acenaphthene is assumed at CP0, which is estimated from contemporary measured concentrations in the wells B27, B28, B29, and B30 (Ries, 1998). By estimating discharges for each well using the hydraulic gradient and the conductivities measured at the wells, a mean concentration at CP0 weighted by the proportionate discharges is determined to $265 \mu\text{g L}^{-1}$. Based on a total discharge of $1.18 \cdot 10^{-3} \text{ m}^3 \text{s}^{-1}$ (Holder, 1999), an acenaphthene mass flow rate of 27.0 g d^{-1} results (Table 8.1). To account for the uncertainty of this estimation of the boundary mass flow rate at CP0, two further scenarios are considered (Table 8.2 and Figure 8.2). To cover a broader range of mass flow rates, the mass flow rate at CP0 is additionally set to 31 g d^{-1} (scenario 2) and 36 g d^{-1} (scenario3), respectively. A variation below the mass flow rate of 27 g d^{-1} , as estimated from the measured con-

Table 8.1 Mean concentrations and mass flow rates of acenaphthene at the control planes.

Control plane	Distance from CP0 [m]	Mean concentration ¹ [$\mu\text{g L}^{-1}$]	Mass flow rate [g d^{-1}]
CP0	0	265 ²	27.0
CP1	50	255	26.0 ³
CP2	180	222	22.6 ⁴

¹ Based on a discharge of $Q=1.18 \cdot 10^{-3} \text{ m}^3 \text{ s}^{-1}$ (Holder, 1999).

² Estimated from point concentrations at B27, B28, B29, and B30 (Ries, 1998).

³ Holder (1999).

⁴ Bockelmann (submitted).

centra tions (scenario 1), does not seem reasonable, as the mass flow rate at CP1 is already 26 g d^{-1} (Table 8.1).

At CP1 and CP2, measured mass flow rate were provided from measurements using the integral mass flow rate approach (Holder, 1999; Bockelmann, subm.). In contrast to the studies of Holder (1999) and Bockelmann (subm.), both control planes are defined each by two instead of four wells (CP1: B42 and P2; CP2: NT01 and B73), as the plume is covered almost entirely ($> 97 \%$) by their capture zones which define the stream tube extent.

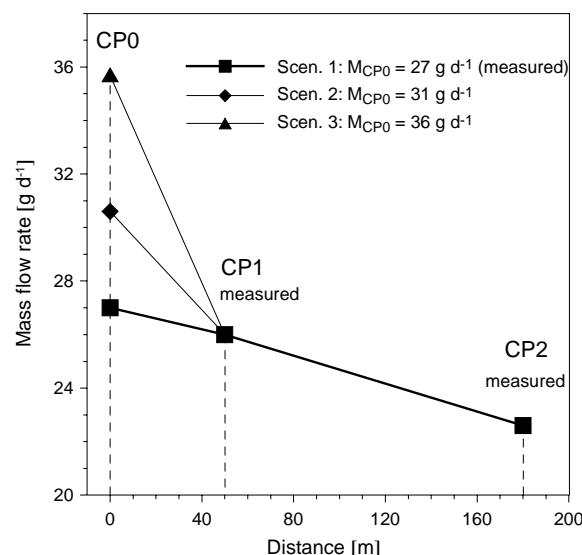


Figure 8.2 Scenarios for initial acenaphthene mass flow rate at CP0 and measured mass flow rates at CP1 and CP2.

Table 8.2 Absolute and relative mass flow rates at the control planes for the different scenarios of boundary mass flow rate.

	Scenario 1		Scenario 2		Scenario 3	
	M [g d^{-1}]	M/M_{CPO} [-]	M [g d^{-1}]	M/M_{CPO} [-]	M [g d^{-1}]	M/M_{CPO} [-]
CP0	27.0	1	31.0	1	36.0	1
CP1	26.0	0.96	26.0	0.84	26.0	0.72
CP2	22.6	0.84	22.6	0.73	22.6	0.63

Table 8.2 and Figure 8.2 depict the decrease of the measured mass flow rates from CP0 to CP2, considering the three different scenarios of boundary mass flow rates at CP0.

8.2.2 Model results and discussion

Transport of acenaphthene was simulated for eight realizations during 45 years, considering kinetic sorption and the above mentioned initial and boundary conditions. Mean breakthrough curves at CP1 and CP2 were determined by averaging all breakthrough curves of the realization ensemble. The simulated temporal development of mean mass flow rates and their standard deviations at the two control planes relative to the boundary mass flow rate at CP0 is shown in Figure 8.3.

Steady state conditions have not been reached after 45 years, indicating the great impact of slow sorption kinetics of acenaphthene on the plume development. The standard deviation of the realization ensemble is relatively small, with largest values for early times and a decreasing tendency (8 % of the mean relative mass flow rate for $t = 2 \text{ a}$ and 0.4 % for $t = 45 \text{ a}$ at CP1; 5.4 % for $t = 2 \text{ a}$ and 0.6 % for $t = 45 \text{ a}$ at CP2). As explained in Chapter 7, the standard deviation of the breakthrough curves is expected to be higher, if geochemical heterogeneity was accounted for in SMART.

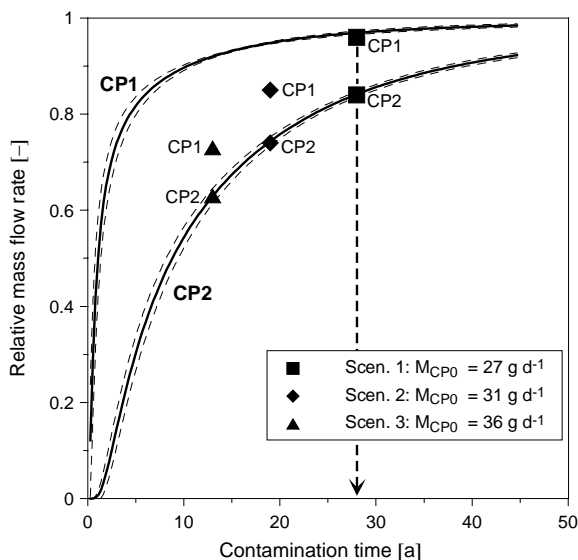


Figure 8.3 Simulated relative mass flow rates over time at CP1 and CP2 (solid line: ensemble average; dashed line: ensemble average \pm standard deviation), compared to measured mass flow rates at CP1 and CP2 considering different scenarios of mass flow rates at CP0.

To estimate the contamination time of the observed acenaphthene plume, the measured relative mass flow rates of the three different scenarios are compared to the simulated relative mass flow rates at both control planes. As the mass flow rates were measured nearly at the same time, compared to the contamination history, both measurements of a scenario must have equal contamination times. Because the ratio of relative mass flow rates is fixed for each scenario, only the contamination time can be varied for each scenario. Therefore, in Figure 8.3, each pair of measured mass flow rates is moved horizontally to obtain a fit with the simulated relative mass flow rates.

The measured mass flow rates at CP1 and CP2 do not fit with the simulated ones for any contamination time, if boundary mass flow rates of 31 g d^{-1} or 36 g d^{-1} (scenarios 2 and 3) are considered. Either the measured and simulated mass flow rates equal at CP1 (for $t \approx 7 \text{ a}$ for scenario 2 and for $t \approx 3 \text{ a}$ for scenario 3) or they equal at CP2 (for $t \approx 19 \text{ a}$ for scenario 2 and for $t \approx 13 \text{ a}$ for scenario 3; depicted in Figure 8.3). Comparing Figure 8.3 to Figure 7.7, where the variability of the realization ensemble also due

to geochemical heterogeneity is included, shows, that this result would also be true if the geochemical heterogeneity was accounted for.

If a boundary mass flow rate of 27 g d^{-1} is assumed (scenario 1), relative mass flow rates at CP1 and CP2 fit the simulated mass flow rates for a contamination time of approximately 28 a. Thus, a consistent contamination time at which measured mass flow rates agree with the simulated ones at both control planes only exists, if the boundary mass flow rate at CP0 is 27 g d^{-1} , which was estimated from concentration measurements. Model simulations and measurements are thus in good agreement.

It has to be emphasized that this estimation of contamination time was performed under the assumption of a constant mass flow rate of acenaphthene at CP0. This is a crucial assumption, as mass flow rates at CP0 had probably been time dependent, because the emitting source is about 50 m upgradient. Consequently, the downstream aquifer was not pristine any more, when the mass flow rate at CP0 became constant with time. The simulated contamination time is therefore a minimum estimate as the time that was needed to achieve a constant concentration at CP0 is neglected. Furthermore, also a constant mass flow rate at the source is a critical assumption, as saturation concentrations of acenaphthene being dissolved from a NAPL source vary with the changing composition of the NAPL according to Raoult's Law (Schwarzenbach et al., 1993). Although tar oil was found at B55 and thus the actual composition of the NAPL is known (Zamfirescu, 2000), the original composition of the NAPL and its dissolution changes are unknown. The complexity of the contamination situation shows clearly that the presented simulations of the acenaphthene plume migration serve as an estimation and should not be overinterpreted.

The simulations reveal the great impact of kinetic sorption on the transport of acenaphthene. Even after 45 years equilibrium conditions have not been reached at a distance of

180 m. An actual retardation factor, that is obtained by the ratio of reactive and conservative travel time for 50 % of the breakthrough, is determined to 43.6. Although acenaphthene is strongly retarded, natural attenuation processes do not lead to an effective reduction of mass in the area considered. Monitored natural attenuation is therefore not suited as remediation strategy at the 'Testfeld Süd' with respect to acenaphthene.

8.3 Inverse determination of degradation rates of p-xylene

In this section, the development of the p-xylene plume is studied. Transport of p-xylene is influenced by kinetic sorption and biodegradation. In contrast to acenaphthene, p-xylene has a higher solubility of 198 mg L^{-1} at 25°C (Schwarzenbach et al., 1993). Hence, sorption is of minor importance compared to the highly sorptive PAH acenaphthene. With respect to biodegradation, p-xylene is expected to degrade well, even under anaerobic conditions (Edwards et al., 1992; Evans et al., 1991; Hutchins et al., 1991). As degradation rates given in the literature vary considerably for the BTEX compounds (Howard et al., 1991; Edwards & Grbic-Galic, 1992; Davis et al., 1999; Schirmer et al., 1999; Wiedemeier et al., 1999), the aim of this section is to estimate degradation rates of p-xylene at the 'Testfeld Süd' by inverse modelling. Therefore, the integrally measured mass flow rates and the stochastic framework outlined in Chapter 4 are employed (Peter et al., 2001). Biodegradation rates are determined by minimizing the objective function defined as the difference between the simulated ensemble averaged mass flow rates and the measured mass flow rates at the control planes (see also Section 4.2.2 for the definition of the objective function). As degradation of p-xylene under anaerobic conditions at the 'Testfeld Süd' is sufficiently slow, p-xylene is still found at larger distances from the source. Therefore, a determination of degradation rates based on mass flow rates measured at several control planes is possible.

8.3.1 Model domain and model set-up

An initially pristine aquifer is assumed for the simulation of the plume development of p-xylene. The contaminant source of p-xylene is again assumed to be located around B49, B55 and B56 (Zamfirescu, 2000). The model domain for p-xylene starts at a source control plane across the wells B55, B56 and reaches up to the second control plane CP2 (Figure 8.4). Again, a single streamtube is used in SMART to represent the flow paths between the source and the second control plane. Flow in the heterogeneous domain is characterized by three sets of pdfs of travel times obtained from eight realizations. The domains for which each of the three sets of pdfs is valid, start at the source and reach CP0, CP1 and CP2, respectively.

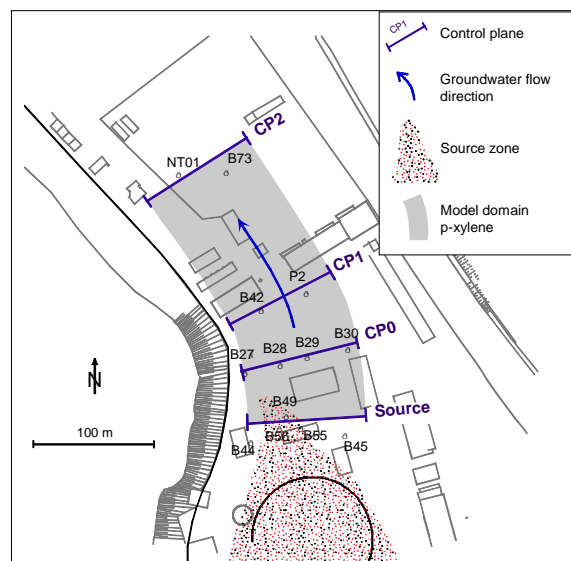


Figure 8.4 Field site 'Testfeld Süd' with model domain for p-xylene and control planes where mass flow rates of p-xylene are determined.

The lithological composition of the aquifer material is chosen according to the summarized facies, shown in Figure 7.4. However, as sorption parameters of p-xylene have not been measured for the lithological material found in

the 'Testfeld Süd', isotherm parameters were estimated according to Grathwohl & Peschik (1997). They postulated a linear relationship between the logarithms of K_d (at a concentration of 10 % of the solubility) and the solubility of the compound. Using the measured isotherms of acenaphthene, phenanthrene and TCE for each lithological component of the 'Testfeld Süd', a linear regression is obtained, from which isotherm parameters for p-xylene are estimated (Table 8.3).

Table 8.3 Estimated sorption parameters for p-xylene and the lithological components of the 'Testfeld Süd' (according to Grathwohl & Peschik, 1997).

Lithological component	K_{fr} [$L \cdot kg^{-1}$] ¹	$1/n_{fr}$ [-]
G_eff	0.20	0.8
Limestone	0.32	0.81
Quartz	0.003	1

¹ K_{fr} determined for concentrations in $mg \cdot L^{-1}$.

In the following simulations, biodegradation is described as an effective process following an n^{th} -order decay (see Section 3.4). Simkins & Alexander (1984) and Alexander (1999) postulate that if the relation of the initial bacterial population to the initial substrate concentration is high, the assumption of a first-order decay is appropriate to describe microbial activity. As in the present case the time scale of contamination and plume development is much larger than the time scale of bacterial growth, the initial bacterial concentration is assumed to be adapted to the contaminant concentration. Thus bacterial growth with time can be neglected.

As boundary condition, a constant concentration boundary is set at the inflow of the model domain, representing the source zone around B49, B55 and B56. Therefore, a mean concentration and mass flow rate at the source control plane (Table 8.4) is estimated using point concentration measurements and hydraulic information at the wells (Schettler, 1998). At CP0, the mean concentration and mass flow rate are also estimated by point concentration measurements

Table 8.4 Mean concentrations and mass flow rates of p-xylene measured at the source control plane, CP0, CP1 and CP2.

Control plane	Distance from source [m]	Mean concentration ¹ [$\mu g \cdot L^{-1}$]	Mass flow rate [$g \cdot d^{-1}$]
Source	0	220 ²	22.4
CP0	50	0.8 ³	0.08
CP1	100	0.4	0.04 ⁴
CP2	230	0.1	0.01 ⁵

¹ Based on a discharge of $Q=1.18 \cdot 10^{-3} m^3 \cdot s^{-1}$ (Holder, 1999).

² Estimated from point concentrations at B44, B56, B49, B55 and B45 (Schettler, 1998).

³ Estimated from point concentrations at B27, B28, B29, and B30 (Ries, 1998).

⁴ Holder (1999).

⁵ Bockelmann (submitted).

(Ries, 1998). Together with the measured mass flow rates at CP1 and CP2 (Holder, 1999; Bockelmann, subm.), these mass flow rates serve as conditioning data for the inverse determination of p-xylene degradation rates.

8.3.2 Model results and discussion

The inverse reactive transport modelling is carried out within a Monte Carlo approach. A degradation rate constant is estimated a priori and reactive transport modelling is performed for all realizations considering kinetic sorption based on the measured parameters and considering biodegradation based on the estimated degradation rate constant. As sorption kinetics of p-xylene are very fast, steady state conditions of the plume are reached within 5 to 10 years for the distances regarded here. The p-xylene plume has therefore reached steady state conditions and mass flow rates at the control planes are time independent. The mean degradation rate constant is then determined by minimizing the difference of the ensemble averaged mass flow rates and the measured mass flow rates. For a detailed description of the inverse stochastic modelling procedure see Section 4.2.2. and especially Figure 4.2.

First, biodegradation rate constants are determined assuming first-order decay (equation 3.18). The mean simulated relative mass flow rates of the realization ensemble at the different control planes are shown in Figure 8.5 in comparison to the measured mass flow rates. As expected, it is not possible to determine a unique degradation rate constant for the overall distance from the source to CP2. Rather, a subsequent modelling for two transport sections, from the source to CP0 and from CP0 to CP2, is carried out.

Assuming a half-life of 1 and 2 days for the first section between the source and CP0, the observed mass flow rate at CP0 is between the simulated mean mass flow rates. As degradation is very high in this section, differences in the travel time distribution of the individual realizations become intensified, especially for short travel distances. The results of the eight realizations therefore differ considerably, causing a high standard deviation of mass flow rates (error bars in Figure 8.5). This finding might indicate, that the variance would be even higher, if the heterogeneity of sorption properties was not neglected.

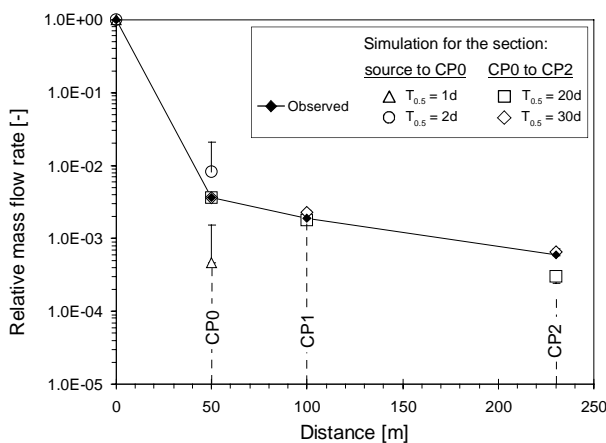


Figure 8.5 Measured and simulated mean mass flow rates of p-xylene at control planes CP0, CP1 and CP2 using a first-order decay. The degradation rate constant was subsequently determined for the sections from the source to CP0 and from CP0 to CP2. Error bars indicate one standard deviation from the ensemble mean of realizations (Peter et al., 2001).

The second section starting at CP0 is best simulated at CP1 with a half-life of 20 days and at CP2 with a half-life of 30 days. The standard deviation of the realization ensemble is now small (not visible in the resolution of Figure 8.5). Thus, the uncertainty of the model predictions at CP1 and CP2 is considerably smaller than at CP0.

Comparing both transport sections, an increase in half-life or a decrease in biodegradation activity with increasing distance from the source is observed. This effect was also reported by Borden et al. (1997), Davis et al. (1999) and Lahvis et al. (1999). As the calibrated half-lives are only valid for the travel distance at which they were determined, reliable predictions cannot be made for other locations between the considered control planes or further downgradient.

Wiedemeier et al. (1999) also discuss the applicability of the first-order concept to describe biodegradation. They note that a first-order decay neglects the rapid consumption of contaminants and electron acceptors, often observed in nature. This may explain, among other things, the great variability of half-lives reported in the literature. Wiedemeier et al. (1999) alternatively suggest an electron-acceptor-limited model, that accounts for a complete depletion of either electron acceptors or donors within the source zone.

A reliable quantification of electron acceptors is difficult in the 'Testfeld Süd', due to widespread ascents of sulphate-rich groundwater from the Gipskeuper (see Chapter 2). Thus, an alternative approach is necessary to describe degradation at the 'Testfeld Süd' considering a strong degradation activity near the source but without the necessity of knowing the amount of electron acceptors.

Hence, a second-order decay concept is used to describe the decreasing microbial activity with increasing transport distance from the source. In the second-order decay concept, the half-life becomes time and space dependent and increases with both (equation 3.22).

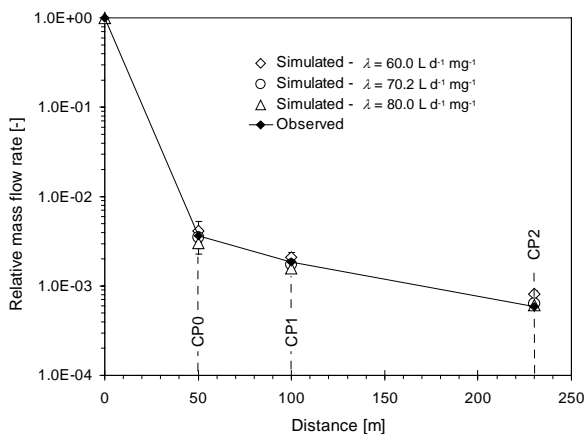


Figure 8.6 Measured and simulated mean mass flow rates of p-xylene at control planes CP0, CP1 and CP2 using a second-order decay. The degradation rate constant was determined for the overall distance from the source to CP2. Error bars indicate one standard deviation from the ensemble mean of realizations (Peter et al., 2001).

Model results involving a second-order decay are shown in Figure 8.6. Obviously, the decrease of observed mass flow rates from the source to CP2 can be simulated very well by calibrating a single second-order degradation rate constant. Best results are obtained for a degradation rate constant of $\lambda = 70.2 \text{ L d}^{-1} \text{ mg}^{-1}$. In addition, even for short travel distances the variance of the realization ensemble is considerably small, which indicates a high prediction reliability.

As a single degradation rate constant describes appropriately the increase of half-life with increasing travel distance, a second-order decay allows for mass flow rate predictions beyond and between the distances at which degradation rates were fitted. However, it is emphasized that the concept of second-order decay cannot explain the microbial processes that occur at the site. Like the first-order approach it is just a mathematical description of the effects of the microbial processes, but not a characterization of the microbial processes themselves.

With the identified first- and second-order biodegradation rates, the natural attenuation processes contributing to the observed mass flow rate decrease can be quantified for p-xylene at

the 'Testfeld Süd'. Consistently for both degradation concepts, more than 99 % of the observed mass flow rate decrease between the source and CP2 is attributed to biodegradation and only about 1 % is caused by sorption. Thus, the decrease of p-xylene mass flow rates at the site is based on intrinsic bioremediation and not on reversible sorption processes.

8.4 Summary and conclusions

In this chapter, the integrated measuring and modelling approach, which was presented theoretically in Chapter 4, was applied at the field site 'Testfeld Süd'. Measured mass flow rates at the 'Testfeld Süd' served as input or conditioning data for the stochastic reactive transport modelling performed within a control plane based approach.

Fate and transport of two compounds was simulated: (a) acenaphthene, a PAH of relatively low solubility, hence with a high sorptivity, and that is considered to be recalcitrant in the absence of naphthalene. (b) p-xylene, a BTEX compound of high water solubility, that is attributed to weak sorption but which biodegrades even under anaerobic conditions.

In the case of acenaphthene, the reactive transport modelling was performed to estimate the mean contamination time and the mean boundary mass flow rate. Different boundary mass flow rates of acenaphthene were assumed at the outer edge of an extended source area, where naphthalene is depleted and thus degradation of acenaphthene does not occur. Within a Monte Carlo approach the uncertainty of hydraulic properties was considered and thus the mean transport behaviour of acenaphthene was determined accounting for kinetic sorption. It is found, that only a mass flow rate of approximately 27 g d^{-1} yields consistent contamination times by comparing measured and mean simulated mass flow rates at the two

downgradient control planes. A contamination time of at least 28 years was then estimated for acenaphthene. The Monte Carlo simulations showed, that for large simulation times (> 15 years), the uncertainty, i.e. the standard deviation of the realization ensemble, due to hydraulic heterogeneity is relatively small. Also considering the uncertainty of geochemical properties would reveal only a slightly higher prediction uncertainty as shown in Section 7.2.2 and Figure 7.7.

Simulations as well as observations of acenaphthene mass flow rates reveal, that steady state conditions of the plume have not been reached. Even after 45 years of simulation time, sorption has not reached equilibrium conditions, demonstrating the great influence of kinetic sorption processes on the development of the acenaphthene plume. Although the potential for retarding acenaphthene is demonstrated to be large, monitored natural attenuation as a remediation alternative does not seem reasonable, as sorption does not lead to an effective mass reduction.

Reactive transport modelling of p-xylene was performed to inversely estimate biodegradation rates at the field site. Biodegradation was represented by an effective process following an n^{th} -order decay. Within a Monte Carlo approach, degradation rate constants were inversely determined by minimizing the objective function defined as the difference of the ensemble averaged mass flow rates and measured mass flow rates at three downgradient control planes. If a first-order decay was chosen to represent microbial activity, a single degradation rate constant could not satisfactorily describe the observed mass flow rates along the whole transport distance. Rather, a subsequent transport modelling within two sections had to be performed, where half-lives of 1 to 2 days were determined for the up-gradient section and half-lives of 20 to 30 days were estimated for the second section. This increase in half-life with increasing distance from the source was also reported by other authors

(Borden et al., 1997; Davies et al., 1999; Lahvis et al., 1999) and lead in this thesis to the necessity of finding an alternative description of microbial activity. Therefore, a second-order decay concept was used to describe more appropriately the decreasing microbial activity, because then the half-life becomes time and space dependent. Model results assuming a second-order decay demonstrate, that a single degradation rate constant of $70.2 \text{ L d}^{-1} \text{ mg}^{-1}$ can excellently simulate the observed mass flow rates at all control planes. The uncertainty of model predictions, i.e. the standard deviation of the realization ensemble, is small along the whole transport distance, which indicates in contrast to the results of first-order decay a higher prediction reliability. However, just like the first-order decay concept, second-order decay does not provide a process based representation of the microbial processes, but is rather a mathematical description of the effects of microbial activity. Further studies at other field sites as well as microbial laboratory studies might bring insight if higher-order decay is an appropriate model concept in general or if the excellent results at the 'Testfeld Süd' are just coincidence.

The simulations of the plume development of p-xylene reveal, that biodegradation mainly contributes to the observed attenuation. More than 99 % of the mass loss observed is due to biodegradation and less than 1 % is caused by sorption processes. As intrinsic bioremediation is responsible for the mass flow rate reduction, (monitored) natural attenuation might be an alternative remediation strategy for p-xylene at the 'Testfeld Süd'.

Similar results for benzene were obtained by Davis et al. (1994) who investigated natural attenuation at a manufacturing facility. They simulated a benzene plume and concluded that degradation represents the dominant process for the observed natural attenuation and that sorption plays only a minor role. Also Borden et al. (1997) inversely estimated biodegradation rates of BTEX compounds. They determined

mass flow rates from point concentration measurements and fitted stepwise degradation rates between the control planes, finding increasing half-lives with increasing transport distance. Thornton et al. (2000) investigated the attenuation of benzene and toluene originating from landfill leachate in column experiments. They inversely fitted equilibrium sorption and degradation parameters to the measured breakthrough curves. Toluene was found to degrade strongly, while sorption did not play an important role for the observed concentration decrease.

The presented approach of combining integrally measured mass flow rates and control plane based stochastic modelling shows that the dominating processes and their parameters occurring at the 'Testfeld Süd' could be identified and quantified. Furthermore, by the means of Monte Carlo simulations, the prediction uncertainty caused by hydraulic heterogeneity could be assessed. The approach thus constitutes a tool to assess natural attenuation at field scale.

9 Combination of the Compound-Specific Isotope Analysis with the Integral Mass Flow Rate Approach and comparison to the Integral Modelling Approach

9.1 Introduction

In the previous chapter, the successful application of the integral measuring and modelling approach was presented. The processes contributing to natural attenuation were quantified by reactive transport modelling, based on reliable mass flow rate measurements and on a process oriented description of kinetic sorption. In this chapter, the developed approach is compared to an expanded compound-specific isotope analysis (CSIA), that allows for an *in situ* estimation of biodegradation.

The CSIA approach was first introduced by Hayes et al. (1990) to determine the isotopic composition of hydrocarbons in sedimentary rocks. Dempster et al. (1997) used CSIA in order to trace organic compounds in groundwater. By establishing a highly sensitive and reproducible analysis technique using gas chromatograph/combustion/isotope rate mass spectrometry (GC/C/IRMS), they investigated BTEX compounds from different manufacturers. They concluded that due to the observed different isotope ratios of the different BTEX products, source identification at contaminated field sites should be possible by tracing isotope ratios in the plume. Further studies expanded the applicability of CSIA to prove the occurrence of biode-

gradation (e.g. Meckenstock et al., 1999; Hunkeler et al., 1999b; Ahad et al., 2000; Bloom et al., 2000; Slater et al., 2001; Hunkeler et al., 2001a; Hunkeler et al., 2001b), as microbial degradation of organic compounds leads to an enrichment of the ^{13}C isotope in the residual contaminant fraction, because bonds formed by the lighter isotope ^{12}C are weaker than bonds formed by the heavier isotope ^{13}C (Hunkeler et al., 1999b). Especially chlorinated hydrocarbons exhibit a strong fractionation of $^{13}\text{C}/^{12}\text{C}$ isotopes during biodegradation, that increases with each step of dechlorination from PCE \rightarrow TCE \rightarrow cis-DCE \rightarrow VC \rightarrow ethene (Hunkeler et al., 1999b; Bloom et al., 2000; Slater et al., 2001). Carbon isotope fractionation of monoaromatic hydrocarbons (BTEX compounds) was investigated by Meckenstock et al. (1999), Ahad et al. (2000) and Hunkeler et al. (2001b). Significant fractionation of toluene (Meckenstock et al., 1999; Ahad et al., 2000) and benzene (Hunkeler et al., 2001b) was found, however being much smaller than the carbon isotope fractionation of chlorinated carbons. Besides carbon isotope fractionation, Ward et al. (2000) and Hunkeler et al. (2001b) also examined $^2\text{H}/^1\text{H}$ fractionation of BTEX compounds. They showed that hydrogen fractionation is much larger compared to carbon fractionation (more than one order of magnitude (Ward et al., 2001); 3.2 to 8.8 times larger

(Hunkeler et al., 2001b)). However, the uncertainty associated with the analytical method as well as the detection limit are higher for hydrogen than for carbon, which reduces the advantage of stronger hydrogen fractionation. Other elements and their respective isotopes that are used for proving the occurrence of biodegradation are e.g. sulphur $^{34}\text{S}/^{32}\text{S}$ (Schroth et al., 2001) and chlorine $^{37}\text{Cl}/^{35}\text{Cl}$ (Sturchio et al., 1998).

The relation between the isotopic shift of a compound caused by biodegradation and the decreased concentration at a time t is quantified by the Rayleigh equation (e.g. Mariotti et al., 1986; Clark & Fritz, 1997):

$$\ln\left(\frac{R_t^C}{R_0^C}\right) = (\alpha^C - 1) \ln\left(\frac{C_{w_t}}{C_{w_0}}\right) \quad (9.51)$$

where R_t^C and R_0^C are the carbon isotope ratios $^{13}\text{C}/^{12}\text{C}$ at the times t and t_0 , respectively. C_{w_t}/C_{w_0} denotes the fraction of the remaining compound and α^C is the carbon fractionation factor. The fractionation factor α^C is sometimes also defined by its reciprocal value, as for instance done by Meckenstock et al. (1999), Steinbach et al. (2000) and Vieth et al. (2001). Throughout this thesis, the fractionation factor α^C is used as defined in equation 9.51. Also often reported is the enrichment factor ε^C , defined as $(\alpha^C - 1) \cdot 1000$ (e.g. Clark & Fritz, 1997).

Two major prerequisites have to be fulfilled for the application of CSIA in the field as a means for demonstrating and quantifying biodegradation: (a) biodegradation has to be the only process that causes significant fractionation of the considered isotopes and (b) for quantifying biodegradation the fractionation factor α^C has to be known. Several studies revealed, that physico-chemical processes like volatilisation from both the aqueous and the organic phase as well as sorption do not produce significant isotopic effects for ^{13}C (Slater et al., 1999; Hunkeler & Aravena, 2000; Hunkeler et al., 2001a). Further-

more, Slater et al. (1999) and Hunkeler & Aravena (2000) demonstrated that also the analytical technique does not produce measurable isotopic changes. The knowledge of the fractionation factor is more difficult to satisfy. It implies firstly, that fractionation factors obtained in laboratory experiments can be transferred to the field and secondly, that the fractionation factor of a specific compound does not depend significantly on the microbial population that degrades the respective compound unless the microorganisms are identified at the site. Hunkeler et al. (1999b) investigated fractionation during dechlorination of PCE in both microcosms and field studies. Although they did not quantify the fractionation by the Rayleigh equation, fractionation patterns of PCE and its products correspond well, so that they conclude, that microcosm data can be used for the interpretation of isotope data obtained in the field. Sherwood Lollar et al. (2001) measured carbon isotope ratios of PCE and TCE at the Dover Air Force Base along two transects and observed an increase in the isotopic ratios, i.e. in heavy isotopes. By using fractionation factors from the literature, they quantified the degree of biodegradation of TCE according to the Rayleigh equation by 40.5 - 66.2 %. Concerning the second aforementioned implication, Meckenstock et al. (1999) as well as Slater et al. (2001) investigated the influence of the microbial consortia under different environmental conditions on the fractionation factors. Both showed, that fractionation factors are within the same range for different bacteria and different electron acceptors.

The review of the mentioned literature shows, that an application of CSIA at field sites in order to prove and to quantify biodegradation is generally possible. However, the few field studies that have been performed so far (Sturchio et al., 1998; Hunkeler et al., 1999b; Sherwood Lollar et al., 2001) always considered isotope ratios and concentrations along a single stream line. Thus, the assumption of a closed system, necessary for the application of the Rayleigh equation, is not justified. Rather, a

single flow path is highly affected by dilution. Furthermore, at field sites with a complex contamination situation, i.e. several not exactly known contamination sources, observations at single wells might lead to an erroneous interpretation of biodegradation by the use of the Rayleigh equation, if the wells do not lie on the same stream line, but sample stream lines that originate from different source zones.

Hence, the aim of this chapter is a combination of the compound-specific isotope analysis with the integral mass flow rate measurement approach (Figure 9.1), that prevents an erroneous interpretation of isotope measurements obtained at single points. Like contaminant mass flow rates (Schwarz et al., 1998; Teutsch et al., 2000), mass flow rates and mean concentrations of the respective isotopes of a contaminant are quantified by enlarging the sample volume that represents a control plane perpendicular to the groundwater flow and by the subsequent inversion of the measured isotope concentration time

series (see also Section 4.1). Visually, the flow path is thus expanded to a streamtube of considerable extent, that is defined by the thickness of the aquifer and the width of the control planes. All advantages of the integral mass flow rate measuring approach discussed in the previous sections apply also for the determination of mean isotope concentrations. Furthermore, the assumption of a closed system, that is necessary to apply the Rayleigh model, is much better justified than if a single flow path is considered. By the combination of CSIA with the mass flow rate approach it is believed by the author that biodegradation can be quantified more reliable by the Rayleigh model than done in previous studies. In a next step, results of the integrally applied CSIA approach are compared to model results that are performed based on measured contaminant mass flow rates according to the approach presented in Chapters 4 and 8 (Figure 9.1). The contributions of biodegradation to the observed mass flow rate reduction quantified by both methods are then compared and evaluated.

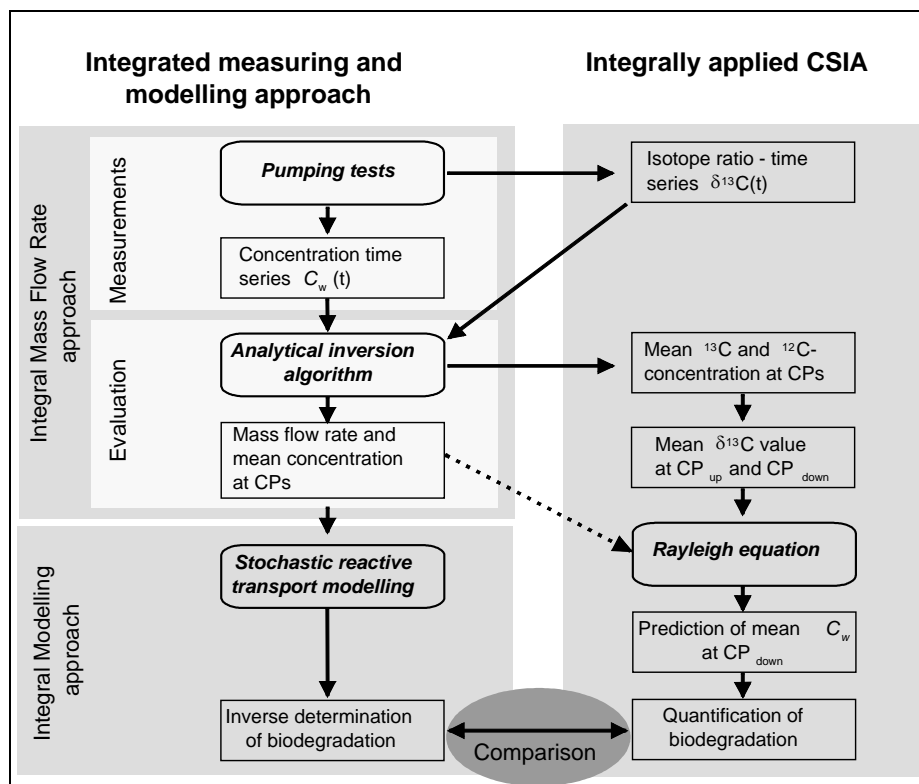


Figure 9.1 Combination of CSIA with the integral mass flow rate approach and comparison to the integral modelling approach. ($CP_{(up/down)}$: (upgradient/downgradient) control plane; C_w : solute concentration; the dotted arrow indicates, that only the mean concentration of the upgradient control plane served as input for the Rayleigh equation).

For this purpose, two additional integral mass flow rate measurements, i.e. integral pumping tests, were performed in collaboration with the University of Hamburg at the 'Testfeld Süd', during which contaminant concentrations and isotope ratios were measured simultaneously. In Section 9.2 the combined integral mass flow rate measurements and the primary hydraulic (9.2.2), chemical (0) and isotope results (9.2.4) are presented. In Section 9.2.5 the determination of contaminant mass flow rates and mean isotope ratios by applying the analytical inversion algorithm is shown. Section 9.3 describes the quantification of biodegradation by stochastic reactive transport modelling according to the previously presented approach. These results are then compared to the degradation potential quantified using the integrally measured carbon isotope ratios.

9.2 Combined integral mass flow rate measurements at the 'Testfeld Süd'

In collaboration with the University of Hamburg two combined integral mass flow rate measurements were performed at the 'Testfeld Süd' in March 2001. The research group of the University of Hamburg (W. Michaelis, A. Steinbach) was responsible for the carbon isotope analysis, while the University of Tübingen lead the campaign, including the administrative organization, the design and implementation of the pumping tests, the chemical analysis and the evaluation and interpretation of the results.

9.2.1 Location of pumping wells and pumping test set-up

The integral mass flow rate measurements were performed at two control planes along a transect in groundwater flow direction. Due to limited financial and time resources, each of the two control planes was defined by only one pumping

well. The wells are located in such a way, that the capture zone of the downgradient well should cover all streamlines that are covered by the capture zone of the upgradient well. Furthermore, the wells had to be situated neither too close to the source, to avoid contamination of the equipment by NAPL, nor too far downgradient, as concentrations rapidly drop below the isotope detection limit. Therefore, a new well (B85) was drilled approximately 25 m downgradient of well B47 (Figure 9.2). Both wells are fully screened within the quaternary aquifer, i.e. the screened intervals are between 4.5 and 7.2 m below ground surface and 4.3 and 7.3 m below ground surface for B47 and B85, respectively.

Both wells were subsequently pumped, approximately two days each, with a mean pumping rate of 3.97 L s^{-1} . To cause a minimum disturbance of the plume, the downgradient well B85 was pumped first. After finishing the test at B85 and two days of recovery, the pumping at B47 was started. Sampling intervals were determined in a way, that with each increase of 2 m of the isochrone radius a sample for both concentration and isotope measurements was taken. The maximum isochrone radius of approximately 20 m was reached after 36h 45min and 36h 55min of pumping at B47 and B85, respectively.

During pumping, the drawdown was automatically measured within the pumped well and at two observation wells. Furthermore, standard parameters like temperature, pH, redox potential, electrical conductivity and oxygen concentration of the pumped water were automatically monitored during the whole experiments (the complete data sets are listed in the appendix A.1).

Analysed contaminants include BTEX compounds, 16 EPA-PAHs, and inorganic ions. Carbon isotope ratios were determined for BTEX and PAH compounds. Measurements of dissolved hydrogen were performed two times at each well to determine the redox potential of the pumped water.

9.2.2 Hydraulic results

Before pumping, groundwater levels were measured at the pumping and observation wells. They served to determine the dominant groundwater flow direction in this sub-domain as well as the hydraulic gradient. Accordingly, the mean groundwater flow direction is approximately from south-southwest to north-northeast (see Figure 9.2). This flow direction as well as the results from the tracer tests (Bösel, 1999; Herfort, 2000) give evidence, that the stream lines passing the upgradient control plane are covered by the downgradient control plane.

A mean hydraulic gradient of 5‰ between B47 and B42 was determined. This locally very steep gradient was confirmed by all previously mea-

sured groundwater levels in the years before (Herfort et al., 1998; Bösel, 1999; Herfort, 2000).

Transmissivities and hydraulic conductivities were evaluated using the drawdown time series at the pumping wells according to the Cooper-Jacob method (Kruseman & de Ridder, 1990). Maximum drawdowns at the pumping wells were 1.29 and 0.6 m at B47 and B85, respectively. The hydraulic conductivity is thus higher at B85 ($2.9 \cdot 10^{-3} \text{ m s}^{-1}$) than at B47 ($1.7 \cdot 10^{-3} \text{ m s}^{-1}$).

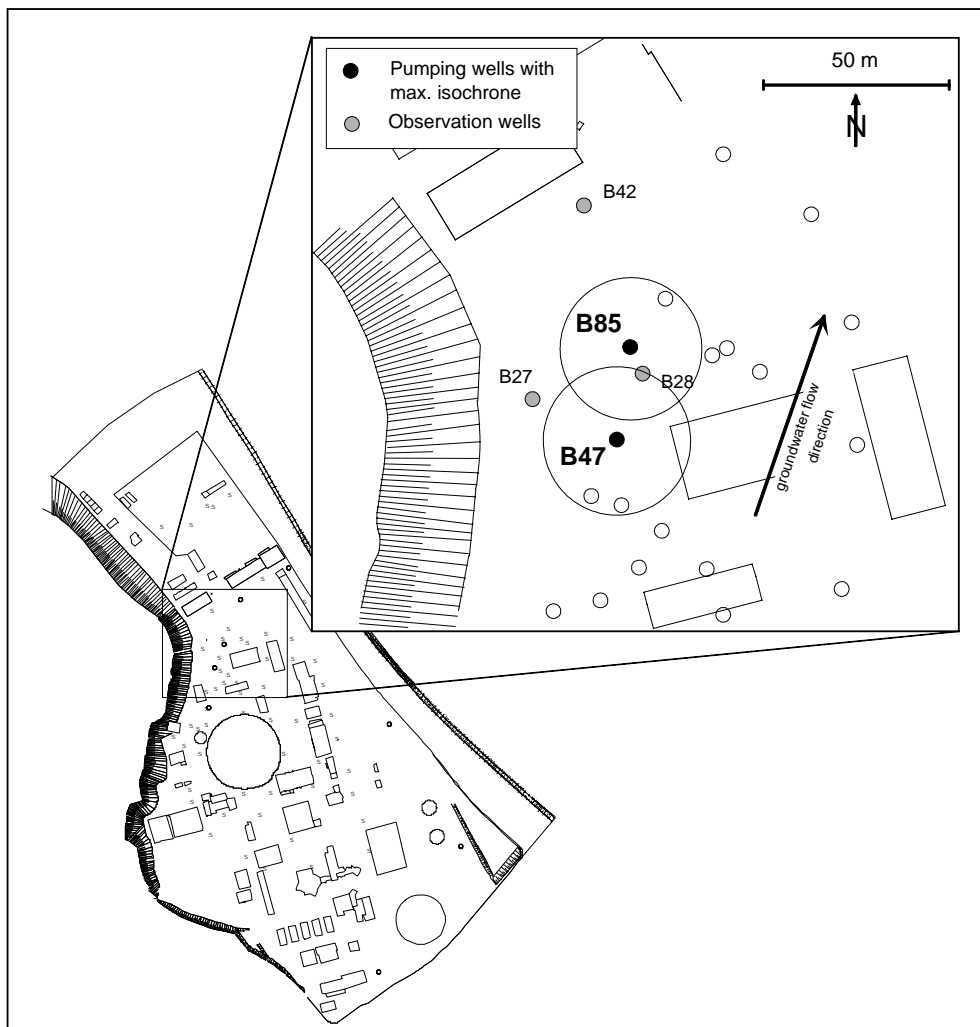


Figure 9.2 Location of the pumping wells used for the integral mass flow rate measurements combined with compound-specific isotope analysis. The maximum isochrones are shown for both pumping wells under the assumption of homogeneous conditions and no hydraulic gradient.

Using the hydraulic gradient and an averaged hydraulic conductivity of B47 and B85, the local mean groundwater flow velocity is estimated to 7.6 m d^{-1} . This value is very high compared to the average groundwater velocity at the 'Testfeld Süd' (approximately 2 m d^{-1}). However, previous groundwater potential surfaces in combination with pumping tests also suggest very high flow velocities in this part of the site (Herfort, 2000). Furthermore, tracer tests revealed highest measured groundwater flow velocities in this sub-domain (Bösel, 1999; Herfort, 2000).

9.2.3 Chemical results and plume composition

Ten samples were taken during each pumping test and analysed for BTEX, PAHs, and ions. BTEX compounds were analysed using the purge-and-trap method, while PAHs were determined with the GC/MS. The detection limit for BTEX and PAH compounds is $0.02 \mu\text{g L}^{-1}$ and $0.025 \mu\text{g L}^{-1}$, respectively. Accuracy is approximately 10 %. Ions except iron and manganese were analysed using ion chromatography (IC), whereas iron and manganese analysis was done using AAS (atomic absorption spectroscopy). The detection limit for the ion analysis is 0.3 mg L^{-1} . For a detailed description of the analytical methods see Piepenbrink (in prep.) and Zamfirescu (2000).

Inorganic compounds were analysed at both wells in order to quantify potential electron acceptors for the degradation process of organic compounds. Oxygen is almost completely depleted in both wells, concentrations are below 0.1 mg L^{-1} during the whole pumping tests. Also nitrate is depleted, as in B47 it is below the detection limit of 0.3 mg L^{-1} , whereas in B85 it is found only in three out of ten samples in very low concentrations of $0.3 - 0.9 \text{ mg L}^{-1}$. Iron(II) as a product of iron(III) reduction is found in considerable amounts in both wells with an increasing tendency towards the downgradient

well: in B47 $0.45 - 0.53 \text{ mg L}^{-1}$ were detected, whereas in B85 $1.01 - 2.3 \text{ mg L}^{-1}$ were found. This indicates degradation activity between the two wells, as the reduced product of the electron acceptor Fe(III) increases. Sulphate concentrations range from 130 to 285 mg L^{-1} at B47, whereas in B85 concentrations vary between $230 - 360 \text{ mg L}^{-1}$. Due to widespread ascents of sulphate-rich groundwater from the underlying Gipskeuper aquifer (see also Chapter 2), it is not possible to quantify the sulphate mass balance.

Measurements of the redox potential confirm the strongly reducing conditions found: at B47, the redox potential varied between -300 and -350 mV . At B85, values of -200 to -275 mV were measured. As an interpretation of the redox measurements to identify the prevailing electron acceptors is not possible (Christensen et al., 2000), additional hydrogen measurements were performed twice at each well. At B47, hydrogen concentrations of 5.8 and 12.2 nmol L^{-1} were detected, whereas at B85 H_2 concentrations of 4.8 and 8.4 nmol L^{-1} were found. Christensen et al. (2000) as well as Appelo & Postma (1996) conclude from several studies, that hydrogen concentrations between $1 - 5 \text{ nmol L}^{-1}$ indicate sulphate-reducing conditions and above 5 nmol L^{-1} methanogenic redox conditions.

The temporal course of the concentrations at a well allows for conclusions of the spatial contaminant distribution, which is quantitatively evaluated by the analytical inversion algorithm for the mass flow rate determination (see Sections 4.1 and 9.2.5). However, insight can also be gained by the qualitative interpretation of the concentration time series (Holder, 1999). In the following, by the aid of three BTEX compounds (benzene, o-xylene and m,p-xylene), relative plume positions are discussed. These compounds will serve furthermore for a detailed evaluation of isotope ratios as they are expected to fractionate during biodegradation. Toluene, often investigated in other studies, was found to be below the isotope detection limit at B85 and

it is therefore not regarded in the following sections. Also the PAH compounds will not be discussed in detail, as they were found either to hardly degrade or not to fractionate during degradation at this site. Nevertheless, the complete results of all analysis are listed in Appendix A.2.

In Figure 9.3 concentration time series of benzene, o-xylene and m,p-xylene are depicted for both wells. Benzene is found in very high concentrations at a relatively constant level of $1000\text{--}1200 \mu\text{g L}^{-1}$ in the upgradient well B47, indicating that the well capture zone is located more or less within the plume (Figure 9.3a). In contrast to B47, the downgradient well B85 exhibits a decreasing tendency of concentrations with time. Thus, it can be assumed that B85 is situated inside the plume and the increasing capture zone begins to reach the margins of the plume. Concentrations at B85 are 3 to 20 times smaller than at B47.

The behaviour of o-xylene is different in both wells (Figure 9.3b). Concentrations in B47 increase with time from almost zero to $80 \mu\text{g L}^{-1}$, i.e. B47 lies outside the o-xylene plume and with increasing isochrones the plume is reached. In the downgradient well B85, o-xylene is nearly completely depleted, concentrations are below $1 \mu\text{g L}^{-1}$.

The temporal course of m,p-xylene in both wells is qualitatively similar like for o-xylene in B47 (Figure 9.3c). An increase in concentrations is observed, thus for both wells the aforementioned concept of attracting the plume applies. Concentrations at B85 however are approximately 100 times lower than at B47.

The concentration time series of these three exemplary compounds reflect the complex contamination situation at the site. It can be assumed that distinct source areas cause the several observed plumes, leading to different positions of the wells relative to the plumes. Furthermore, a very high microbial activity or, more general, natural attenuation activity can be postulated

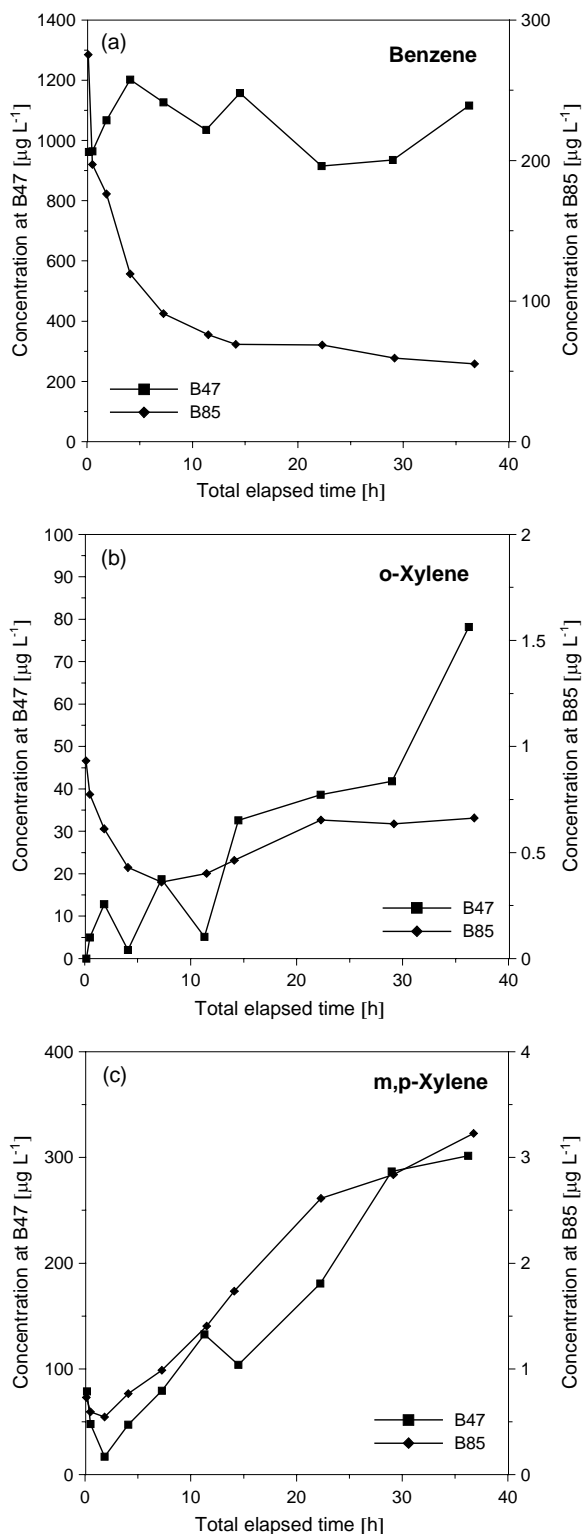


Figure 9.3 Measured concentration time series at both wells for (a) benzene, (b) o-xylene and (c) m,p-xylene.

between B47 and B85 as some compounds show a decrease by a factor of 100. However, benzene and also acenaphthene (not shown here) reveal a higher persistence.

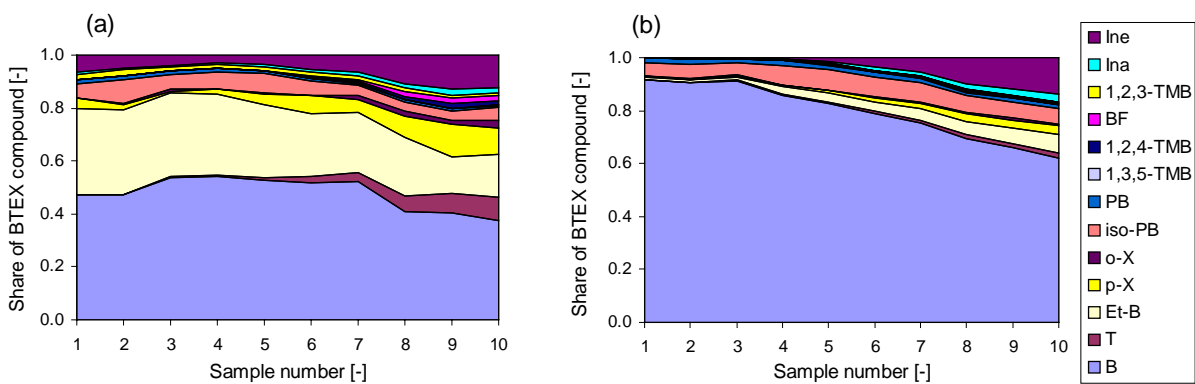


Figure 9.4 Plume composition of BTEX compounds (a) at B47 and (b) at B85.

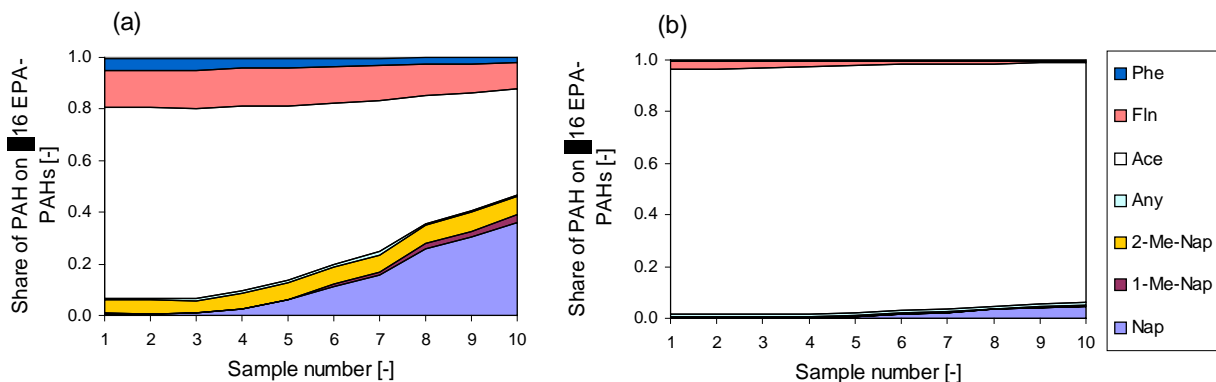


Figure 9.5 Plume composition of PAH compounds (a) at B47 and (b) at B85.

Valuable information about plume composition and possibly different sources can be gained by looking at the proportion of each compound relative to the sum of the compound group. In Figure 9.4 the share of each BTEX compound is plotted during the course of the pumping tests at both wells. In both wells, benzene constitutes the main BTEX contaminant with a proportion of 50 % and 60 - 90 % at B47 and B85, respectively. Besides ethyl-benzene (Et-B), which considerably contributes to the BTEX plume(s) at B47 but not at B85, the plume compositions are qualitatively similar at both wells.

Plume composition with respect to the PAH compounds is depicted in Figure 9.5. Here, acenaphthene dominates the PAH plume at both wells. At B47, it contributes with 40 to 80 % to the PAH plume, whereas at B85 acenaphthene is almost the only PAH found. At B47, besides acenaphthene also naphthalene is observed in considerable amounts with an increasing tendency with increasing time (or sample number).

Although almost completely depleted, naphthalene shows the same qualitative behaviour at B85. Naphthalene is assumed to be the best degradable PAH compounds (e.g. Starke et al., 1991; Mackenbrock et al., 1994; Selifonov et al., 1998), which might explain the strong relative decrease from B47 to B85. Fluorene is the third important PAH compound and shows the same qualitative behaviour at both wells, as naphthalene.

As the patterns of plume composition correspond fairly well at both wells for both groups of contaminants, it can be assumed that at both wells the same plumes were detected. This is a crucial assumption, which is essential for all following evaluations and will be discussed in the subsequent sections again by the aid of the isotope data.

9.2.4 Carbon isotope results

Stable carbon ^{13}C and ^{12}C isotope were analysed by the University of Hamburg for all BTEX and PAH compounds of each sample taken at B47 and B85. For a description of the analytical methods see Steinbach et al. (2000) and Steinbach et al. (in prep.). The isotope ratios $^{13}\text{C}/^{12}\text{C}$ are expressed in the δ -notation [%] normalized to the Vienna PeeDee Belemnite Standard VPDB (e.g. Clark & Fritz, 1997):

$$\delta^{13}\text{C} = \left(\frac{R_t^{\text{C}}}{R_{\text{VPDB}}} - 1 \right) \cdot 1000 \quad (9.52)$$

where R_t^{C} and R_{VPDB} ($R_{\text{VPDB}} = 0.0112372$) are the $^{13}\text{C}/^{12}\text{C}$ ratios of the sample and the standard, respectively.

The detection limit of the carbon isotope analysis is $0.5 - 1 \mu\text{g L}^{-1}$. Each sample was analysed at least six times and the standard deviation was calculated to prove and quantify the accuracy of the analytical method. For the compounds discussed here, the mean standard deviation of the samples is approximately 1 %. However, samples of low concentrations reveal standard deviations of up to 2.3 %.

Besides the determination of mean isotope ratios by applying the analytical inversion algorithm (see Section 9.2.5), the $\delta^{13}\text{C}$ time series at both wells also allow for a qualitative interpretation, whether an isotopic shift observed stems from biological degradation or from different contaminant sources with different isotopic signatures.

The $\delta^{13}\text{C}$ time series and the concentration time series for the exemplary compounds benzene, o-xylene and m,p-xylene are depicted in the following three figures (Figure 9.6 through Figure 9.8).

In Figure 9.6a,b $\delta^{13}\text{C}$ values and concentrations of benzene are plotted. Isotope ratios show a relatively constant behaviour in both wells, however on different levels: $\delta^{13}\text{C}$ values at B47 range from -23.4 ‰ to -24.9 ‰ , whereas B85

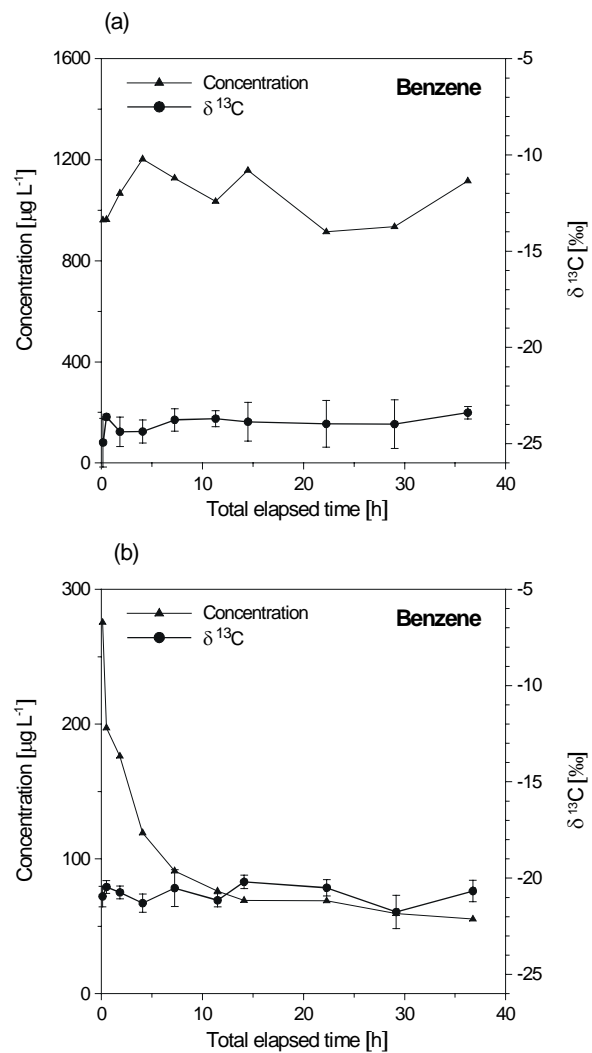


Figure 9.6 ^{13}C isotope signature with standard deviation and concentration of benzene at (a) well B47 and (b) well B85.

reveals heavier isotope signatures between -20.2 and -21.8 ‰ . Thus, the δ -shift between both wells varies between 1.6 ‰ and 4.7 ‰ . This significant enrichment of the heavy ^{13}C isotope in the downgradient well B85 is accompanied by a decrease of the benzene concentration by a factor of approximately 5 to 10. This might indicate biological degradation activity.

In B85 however (Figure 9.6b), decreasing benzene concentrations during pumping do not reflect a significant increase in isotope values. This effect might stem from the fact, that with increasing radius of the isochrone groundwater of different concentrations and thus different isotopic signatures from the up- and downgradient part of the isochrone is pumped.

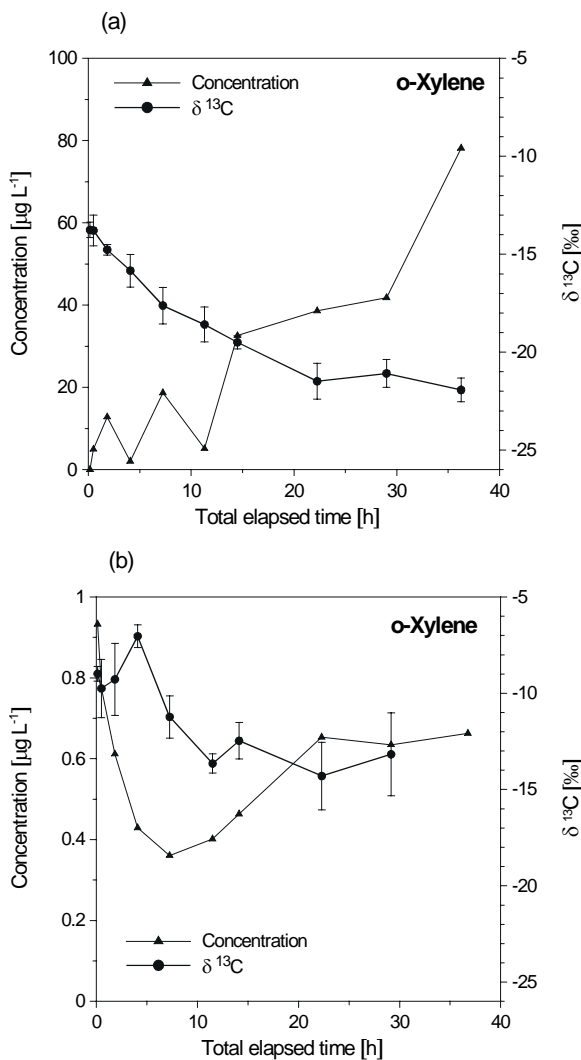


Figure 9.7 ^{13}C isotope signature with standard deviation and concentration of *o*-xylene at (a) well B47 and (b) well B85.

Mixing of water of high concentration and light isotopic value with water of low concentration and heavy isotopic value reveal a lighter isotopic value than the arithmetic average. In the following Section 9.2.5, the effect of linearly decreasing concentrations within a capture zone and the mixing of waters of different concentrations and isotope ratios is quantified.

The temporal course of *o*-xylene concentrations during pumping is depicted in Figure 9.7. In contrast to benzene, *o*-xylene shows an isotopic shift not only from the upgradient well to the downgradient well but also within the concentration time series. In the upgradient well B47 (Figure 9.7a) concentrations increase with time, indicating that the plume was reached with in-

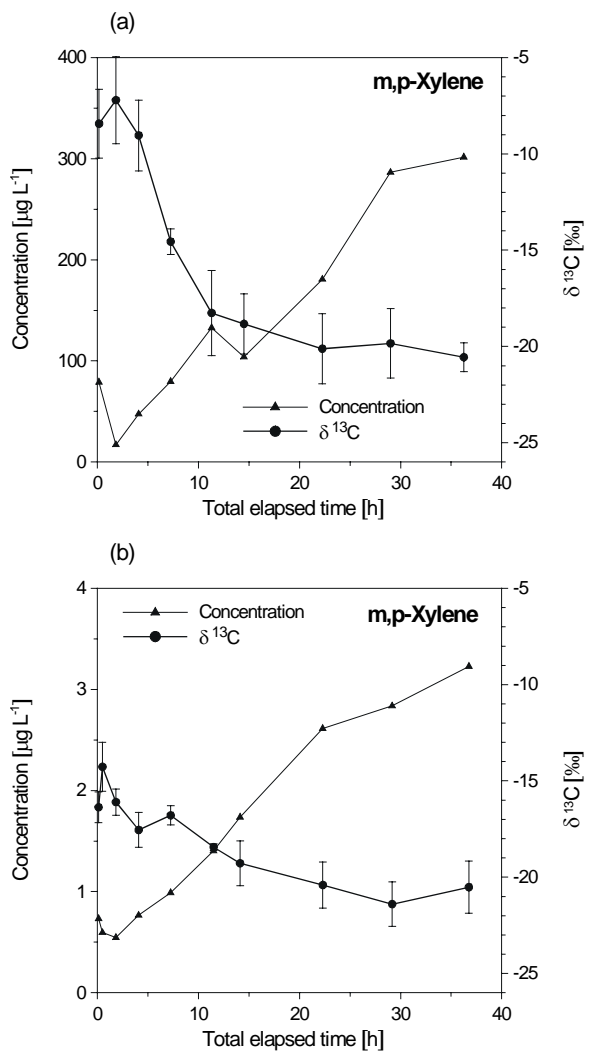


Figure 9.8 ^{13}C isotope signature with standard deviation and concentration of *m,p*-xylene at (a) well B47 and (b) well B85.

creasing pumping time (see Section 0). High concentrations, indicating the direction towards the plume centre, show light $^{13}\text{C}/^{12}\text{C}$ compositions, i.e. $\delta^{13}\text{C}$ values of -21.1 to -21.9 ‰. With decreasing concentrations towards the plume margins, $\delta^{13}\text{C}$ values increase up to -13.8 ‰, showing an enrichment of the heavy ^{13}C isotope in the remaining *o*-xylene fraction. This finding indicate an increased microbial activity at the plume edges compared to the centre of the plume. From the upgradient well B47 to the downgradient well B85, an isotopic shift in *o*-xylene is also observed (Figure 9.7b). Concentrations have fallen below 1 $\mu\text{g L}^{-1}$ and $\delta^{13}\text{C}$ values range from -14.3 ‰ to -7.0 ‰. Due to the very low concentrations, the standard deviations of these isotope values are higher than for

the other samples, reaching maximum values of 2.2 ‰. Nevertheless, the isotopic shifts observed between the wells as well as within each $\delta^{13}\text{C}(t)$ -curve are about 7 - 8 ‰. Both isotopic shifts might be explained by biodegradation as concentrations decrease approximately by a factor of 80 within the B47 $C_w(t)$ -curve and from B47 to B85.

In Figure 9.8 $\delta^{13}\text{C}$ values and concentrations of m,p-xylene are depicted. In both wells, concentrations increase with pumping time and an according shift towards light isotope ratios is observed. Isotope ratios range from -20.6 ‰ to -7.2 ‰ and from -21.4 ‰ to -14.3 ‰ at B47 and B85, respectively. The very heavy isotope values in B47 show high standard deviations with values up to 2.3 ‰. Although the $\delta^{13}\text{C}$ values vary within a similar range, concentrations vary considerably between both wells. In B47, concentrations increase from 17 to 300 $\mu\text{g L}^{-1}$, whereas in B85 concentrations start below 1 $\mu\text{g L}^{-1}$ and rise to 3 $\mu\text{g L}^{-1}$. As fractionation of m,p-xylene was found to occur at the 'Testfeld Süd' (Steinbach et al., in prep.), it is not clear up to now, why the decrease in concentration by a factor of 100 is not accompanied by an according isotopic shift between the two wells.

Summarizing, the isotopic shifts observed for benzene and o-xylene are probably caused by microbial degradation, as they are accompanied by a corresponding concentration change, either within the concentration time series and/or between the wells. In contrast to that, m,p-xylene does not reveal a clear isotope fractionation between the two wells. Compounds that are not expected to degrade significantly, i.e. acenaphthene, reveal the same range of isotope ratios at both wells (see Appendix A.3). This also indicates, that the same streamtubes are sampled in both wells.

9.2.5 Mass flow rate determination by analytical inversion

The measured concentration time series at the wells depend on the spatial distribution of the contaminant in the undisturbed aquifer. Under the assumption of a negligible hydraulic gradient and constant concentrations within a stream line, Schwarz et al. (1998) developed an analytical solution for the spatial distribution of the contaminant concentration, dependent on the concentration time series and aquifer properties. The solution allows for a determination of a mean concentration and a contaminant mass flow rate across the control plane. The theory of this inversion algorithm is given in detail in Section 4.1.

The inversion algorithm is applied to contaminant concentrations, i.e. of BTEX and PAH compounds, as well as to isotope concentrations of a specific compound, that are determined from the isotope ratios R_t^C and the compound concentration:

$$C_w[{}^{12}\text{C}] = \frac{C_w[\text{C}]}{1 + R_t^C} \quad (9.53)$$

and

$$C_w[{}^{13}\text{C}] = \frac{C_w[\text{C}]}{1 + \frac{1}{R_t^C}} \quad (9.54)$$

with

$$C_w[\text{C}] = C_w \cdot \beta \quad (9.55)$$

where $C_w[{}^{12}\text{C}]$ and $C_w[{}^{13}\text{C}]$ denote the concentrations of the isotopes ${}^{12}\text{C}$ and ${}^{13}\text{C}$ of the specific compound; $C_w[\text{C}]$ is the carbon concentration of the compound and β denotes the weight fraction of carbon to the total weight of the molecule.

The analytical inversion algorithm is based on the assumption of a constant concentration along a stream line. However, assuming a linear concentration profile yields identical results for the mean concentration and the mass flow rate,

as the assumed isochrones are circles and thus symmetrical to the control plane in up- and downgradient direction. Hence, assuming a constant concentration gradient is a valid assumption for the application of the analytical inversion algorithm. However, a linear concentration profile causes a non-linear $\delta^{13}\text{C}$ profile, if the fractionation follows the Rayleigh equation (9.51). By solving equation (9.51) for R_t and substituting the result into equation (9.52), the relation for $\delta^{13}\text{C}$ in dependence on the concentration C_w is obtained:

$$\delta^{13}\text{C}(C_w) = \left[\left(\frac{\delta_0}{1000} + 1 \right) \cdot \left(\frac{C_w}{C_{w0}} \right)^{(\alpha^c - 1)} - 1 \right] \cdot 1000 \quad (9.56)$$

where δ_0 is the $\delta^{13}\text{C}$ value of the compound at the initial concentration C_{w0} . If a linear concentration profile, i.e. a decay of zero-order, is assumed, equation (9.56) becomes dependent on the transport distance x :

$$\delta^{13}\text{C}(x) = \left[\left(\frac{\delta_0}{1000} + 1 \right) \cdot \left(1 - \lambda \frac{x}{v_x C_{w0}} \right)^{(\alpha^c - 1)} - 1 \right] \cdot 1000 \quad (9.57)$$

where λ denotes the zero-order degradation rate constant and v_x the x -component of the flow velocity vector. It can be seen in equation (9.57), that the linear concentration profile results in a power function for $\delta^{13}\text{C}(x)$. This non-linearity demands for a closer investigation of the interpretation of $\delta^{13}\text{C}$ values from samples taken during pumping tests.

In the following, a brief example as close as possible to the conditions found at the site is given to demonstrate the weak influence of the non-linearity of equation (9.57) on the measured $\delta^{13}\text{C}$ time series in a well during pumping. An isochrone at a pumping well with a maximum radius of 20 m is considered (Figure 9.9). The width of the contaminant plume is assumed to be larger than the diameter of the isochrone. The concentration of the pumped sample corres-

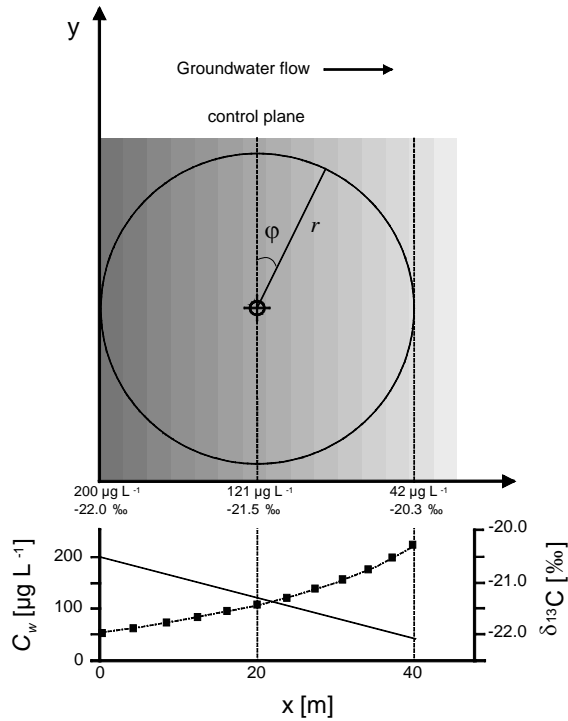


Figure 9.9 Schematic illustration of the undisturbed plume with linear concentration profile (solid line) and the corresponding $\delta^{13}\text{C}(x)$ profile (dashed line) along the transport distance. The isochrone, that is reached after maximum pumping time, is projected onto the undisturbed plume. For explanations, see text.

ponding to the considered isochrone represents the average contaminant concentration along the isochrone.

A linear concentration profile is assumed, defined by the following parameters: $\lambda = 30 \mu\text{g L}^{-1} \text{ d}^{-1}$, $v_x = 7.6 \text{ m d}^{-1}$ and $C_{w0} = 200 \mu\text{g L}^{-1}$. Thus, within the considered isochrone (i.e. $x = 40 \text{ m}$) concentrations decrease from $200 \mu\text{g L}^{-1}$ to $42 \mu\text{g L}^{-1}$ from the upgradient to the downgradient edge. Due to symmetrical reasons, the concentration of the sample, that corresponds to the isochrone, equals the concentration at the control plane that is defined as the diameter of the isochrone perpendicular to the groundwater flow direction at the well. Concerning the isotope ratios, the $\delta^{13}\text{C}$ values increase non-linearly with increasing distance according to equation (9.57). Assuming an initial $\delta^{13}\text{C}$ value of -22.0 ‰ at the distance $x = 0 \text{ m}$ and a fractionation factor α^c of 0.9989012 for o-xylene (Vieth et al., 2001), $\delta^{13}\text{C}$ increases to

-20.3 ‰ at $x = 40$ m. At the control plane (i.e. $x = 20$ m) a $\delta^{13}\text{C}$ value of -21.5 ‰ is determined. If the $\delta^{13}\text{C}$ profile were linear, the $\delta^{13}\text{C}$ value of the sample pumped at the well would reveal also a $\delta^{13}\text{C}$ value of -21.5 ‰. Thus, the deviation from this value gives evidence on the error caused by the non-linearity of the $\delta^{13}\text{C}$ profile. The contaminant concentration along the upgradient (-) and downgradient (+) half of the isochrone is given by:

$$C_w(\varphi) = C_{w0} - \lambda \cdot \frac{r \pm \sqrt{r^2 - (r \cdot \cos \varphi)^2}}{v_x} \quad (9.58)$$

where φ is the angle within the isochrone defining the deviation from the control plane (see Figure 9.9) and r is the isochrone radius. By discretising φ in equation (9.58) in 1° steps, average ^{13}C and ^{12}C concentrations are determined according to equations (9.53) through (9.55) and (9.58). The average ^{13}C and ^{12}C concentrations over the isochrone yield a $\delta^{13}\text{C}$ value of -21.6 ‰. Thus, the absolute difference between the $\delta^{13}\text{C}$ value at the control plane (-21.5 ‰) and the $\delta^{13}\text{C}$ value of the actual sample is 0.1 ‰, which is within the accuracy of the analytical method. Thus, it is shown, that the assumption of a linear concentration profile that results in a weak non-linear $\delta^{13}\text{C}$ profile is a justified assumption for the application of the inversion algorithm to isotope concentration data.

The application of the analytical inversion algorithm requires the knowledge of hydraulic parameters that describe the undisturbed aquifer, i.e. aquifer thickness, hydraulic conductivity, hydraulic gradient, and the effective porosity (see also Section 4.1). Furthermore, the pumping rate is a necessary input parameter in order to determine the isochrones in dependence on the elapsed pumping time. Mean hydraulic values between B47 and B85 are used for the application of the inversion algorithm, as the average represents best the area around both wells with their overlapping capture zones. The used input parameters are listed in Table 9.1. The application of the analytical inversion algorithm results

in the radius of the maximum isochrone on the one hand and in mean concentrations across the control plane on the other hand. The extent of the control plane is defined by the diameter of the maximum isochrone and the aquifer thickness. Thus, a discharge across the control plane within the undisturbed aquifer can be calculated (see Table 9.1). Slight differences in the maximum radius and thus discharges at the two wells stem from the slightly longer pumping period at B85 (10 min.). The mean concentration and the discharge yield the mass flow rate across the control plane.

Table 9.1 Input and output hydraulic parameters valid between B47 and B85, as used for the analytical inversion algorithm.

	B47	B85
Aquifer thickness [m]	3.15	3.15
Hydraulic conductivity [m s^{-1}]	$2.3 \cdot 10^{-3}$	$2.3 \cdot 10^{-3}$
Gradient [-]	$5.0 \cdot 10^{-3}$	$5.0 \cdot 10^{-3}$
Effective porosity [-]	0.13	0.13
Pumping rate [L s^{-1}]	3.97	3.97
Max. radius [m]	20.1	20.2
Discharge [L s^{-1}]	1.45	1.46
Flow velocity [m d^{-1}]	7.64	7.64

Mean concentrations and mass flow rates of BTEX and PAH compounds across the control planes of both wells are summarized in Table 9.2.

At the upgradient control plane B47 the contaminant mass flow rates are dominated by the BTEX compounds, which contribute 75 % to the total contaminant mass flow rate of approximately 420 g d^{-1} . Within the BTEX compounds, benzene dominates with 130 g d^{-1} compared to the total BTEX mass flow rate of 312 g d^{-1} . Concerning the PAH compounds, acenaphthene shows the highest mass flow rate of 52 g d^{-1} , which constitutes almost 50 % of the total PAH mass flow rate.

At the downgradient control plane B85, the BTEX compounds represent with 12.5 g d^{-1} only 30 % of the total contaminant mass flow rate, as the BTEX compounds are more rapidly attenuated between B47 and B85 than the PAH

compounds. However, within the BTEX compounds, the contributions of the single compounds do not change significantly, besides benzene, whose contribution increases from 42 % at B47 to more than 70 %. Within the PAH compounds, the share of acenaphthene increases drastically from 49 % at B47 to 94 % at B85.

When the mass flow rates of each compound at the downgradient control plane at B85 are normalized by the compound specific mass flow rates at the upgradient control plane at B47, relative mass flow rates result (Table 9.2, right column and Figure 9.10). The relative mass flow rates allow for an estimation of the overall natural attenuation potential of each compound.

Figure 9.10a reveals, that benzene and propylbenzene (PB) are the most recalcitrant contaminants among the BTEX compounds in the considered area, as their relative mass flow rates at B85 are highest. In contrast, toluene, ethyl-benzene and the xylenes experience a reduction between B47 and B85 to approximately 1 %.

In Figure 9.10b the relative mass flow rates at B85 of the PAH compounds are depicted. As already concluded from Table 9.2, acenaphthene reveals the highest relative mass flow rate, i.e. natural attenuation processes are only capable to reduce the mass flow rate to 53 %. Also acenaphthylene and pyrene show a high persistence,

Table 9.2 Mass flow rates and mean concentrations of BTEX and PAH compounds at the control planes of wells B47 and B85. The relative mass flow rate at B85 is normalized by the mass flow rate of the specific compound at the upgradient control plane B47.

Compound	B47		B85			Relative mass flow rate [%]
	Mass flow rate [g d ⁻¹]	Mean concentration [µg L ⁻¹]	Mass flow rate [g d ⁻¹]	Mean concentration [µg L ⁻¹]		
Benzene	130.92	1045.0	8.86	70.3		6.8
Toluene	20.11	160.6	0.16	1.3		0.8
Et-B	59.87	477.9	0.64	5.1		1.1
m,p-X	27.47	219.3	0.32	2.5		1.1
o-X	5.93	47.3	0.08	0.6		1.3
iso-PB	14.05	112.2	0.78	6.2		5.5
PB	2.46	19.6	0.18	1.4		7.3
1,3,5-TMB	0.86	6.9	0.03	0.2		3.2
1,2,4-TMB	3.55	28.3	0.04	0.3		1.0
BF	5.34	42.6	0.03	0.2		0.5
1,2,3-TMB	3.71	29.6	0.04	0.4		1.2
Ina	5.20	41.5	0.25	2.0		4.8
Ine	32.52	259.6	1.12	8.8		3.4
Σ BTEX	311.99	2490.4	12.52	99.2		4.0
Nap	29.05	231.9	1.03	8.2		3.5
1-Me-Nap	2.16	17.2	0.01	0.1		0.4
2-Me-Nap	7.55	60.2	0.07	0.6		1.0
Any	0.92	7.3	0.34	2.7		37.1
Ace	51.91	414.3	27.62	219.0		53.2
Fln	12.39	98.9	0.33	2.7		2.7
Phe	2.59	20.7	0.03	0.2		1.0
Ant	0.17	1.4	0.04	0.3		23.9
Fth	0.06	0.5	0.01	0.1		23.1
Py	0.02	0.1	0.01	0.1		36.0
Σ PAK	106.82	852.6	29.49	233.8		27.6

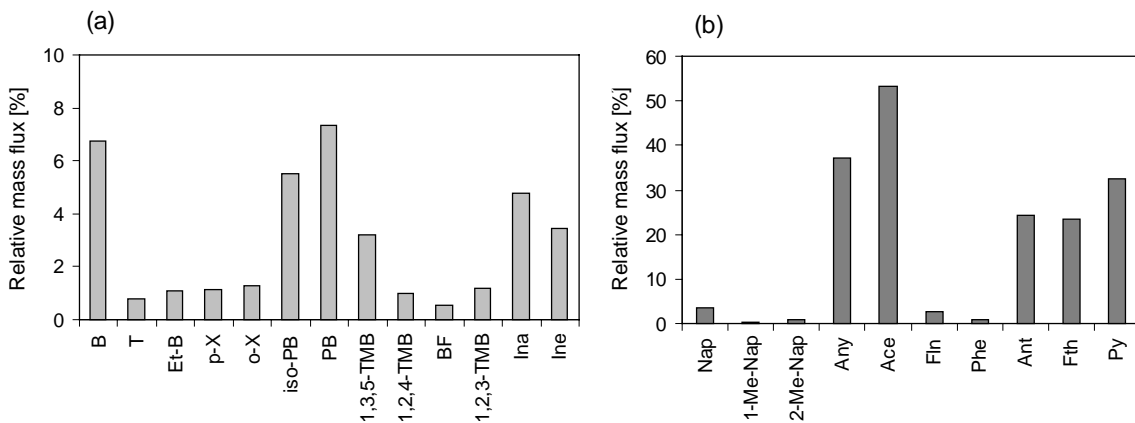


Figure 9.10 Mass flow rates at B85 relative to the compound specific mass flow rates at B47. (a) BTEX compounds, (b) PAH compounds.

as their mass flow rates at B85 decrease only to 37 % and 36 %, respectively.

Anthracene and fluoranthene mass flow rates reduce from B47 to B85 to approximately 25 %, whereas all other PAH compounds either reveal relative mass flow rates below 4 % or are below the detection limit at B85.

For the three exemplary compounds discussed already in Sections 0 and 9.2.4, mean compound specific carbon isotope concentrations were determined across the control planes using the analytical inversion algorithm (Table 9.3). The same hydraulic parameters were used as before (see Table 9.1). Based on the mean carbon

isotope concentrations at the control planes, mean $\delta^{13}\text{C}$ values were calculated applying equation (9.52).

By the aid of these spatially integrated $\delta^{13}\text{C}$ values, more reliable conclusions can be drawn on the degradation behaviour as could be done by isotope ratios obtained from point measurements. Both, the contaminant concentrations and the $\delta^{13}\text{C}$ values obtained by the application of the integral mass flow rate approach and its analytical inversion algorithm represent integrated values across the control planes. Thus, an effective degradation behaviour within the streamtube which is defined by the two control planes and the corresponding streamlines can be inferred. For benzene, a mean isotope shift of approximately 3 ‰ is observed between the two control planes which is accompanied by a 93 % reduction of benzene. In contrast to benzene, m,p-xylene does not show a clear enrichment of heavy ^{13}C isotopes, as the difference of the mean $\delta^{13}\text{C}$ values of both control planes is below the accuracy of the isotope method of 1 ‰. o-xylene reveals the largest isotopic shift of more than 5 ‰ between the two control planes which is accompanied by a mass flow rate reduction of almost 99 %.

In the following, a quantification of the biological degradation by applying the Rayleigh equation (equation 9.51) is performed as also

Table 9.3 Mean compound specific carbon isotope concentrations and mean $\delta^{13}\text{C}$ values (a) at control plane B47 and (b) at control plane B85.

(a)	B47		
	$C_w [^{13}\text{C}]$ [ng/l]	$C_w [^{12}\text{C}]$ [ng/l]	$\delta^{13}\text{C}$ [%]
Compound			
Benzene	10467.7	954170.5	-23.74
m,p-Xylene	2163.6	196440.2	-19.87
o-Xylene	466.3	42405.5	-21.36

(b)	B85		
	$C_w [^{13}\text{C}]$ [ng/l]	$C_w [^{12}\text{C}]$ [ng/l]	$\delta^{13}\text{C}$ [%]
Compound			
Benzene	705.8	64149.7	-20.87
m,p-Xylene	24.7	2240.4	-20.51
o-Xylene	5.9	533.7	-16.13

$$R_{\text{VPDB}} = 0.0112372$$

done by Sherwood Lollar et al. (2001). This can only be done for o-xylene, as fractionation factors for benzene have not been measured under anaerobic conditions so far and m,p-xylene does not reveal a significant fractionation between the two control planes.

By the use of the mean isotope ratios at the two control planes and the mean concentration of the upgradient control plane as input, the mean concentration at the downgradient control plane can be predicted using the Rayleigh equation and a corresponding fractionation factor. The ratio of the predicted concentration at the downgradient control plane and the concentration at the upgradient control plane allows a quantification of microbial degradation occurring between the considered control planes. If the predicted concentration at the downgradient control plane is higher than the actually observed concentration, further natural attenuation processes may contribute, e.g. sorption.

Vieth et al. (2001) determined a fractionation factor α^C for o-xylene under anaerobic conditions in laboratory experiments with 0.9989012 (i.e. $\alpha^C = 1/\alpha_{\text{Vieth}}^C = 1/1.0011$; see definition of α^C in equation 9.51). Applying the Rayleigh equation by using the mean $\delta^{13}\text{C}$ values at both control planes and the mean concentration of the upgradient control plane (Table 9.4) yields a predicted mean concentration at the downgradient control plane B47 of $0.4 \mu\text{g L}^{-1}$. This means that 99 % of the contaminant mass at B47 got biodegraded. The observed mean concentration at B47 is $0.6 \mu\text{g L}^{-1}$, indicating that the complete concentration and mass flow rate reduction observed between the two control planes is caused by biodegradation, because both concentrations are identical within the range of accuracy. A comparison to the model results that also quantify the contributions of the natural attenuation processes is presented in Section 9.4.

Table 9.4 Mean $\delta^{13}\text{C}$ values, mean observed and predicted concentrations ($C_w \text{ obs.}$ and $C_w \text{ pred.}$) of o-xylene at the two control planes B47 and B85 using the Rayleigh relation.

	B47	B85
$\delta^{13}\text{C} [\text{\textperthousand}]$	-21.36 ¹	-16.13 ¹
$C_w \text{ obs.} [\mu\text{g L}^{-1}]$	47.3	0.6
$C_w \text{ pred.} [\mu\text{g L}^{-1}]$	-	0.4

¹ used as input for the Rayleigh equation.

Unlike the estimations for biodegradation at field scale done in studies before (Sherwood Lollar et al., 2001; Sturchio et al., 1998), this estimation is based on a control plane based streamtube and not on a single streamline. Thus, effects of a concentration reduction due to dilution by dispersion is significantly reduced by the enlargement of the considered sampling domain. Therefore, when applying the integral CSIA method, the assumption of a closed system necessary for the application of the Rayleigh relation is much better justified than by considering a single streamline.

9.3 Quantification of biodegradation applying the modelling approach

In this section, biodegradation is quantified using the stochastic reactive transport modelling approach presented in the sections before. Using the control plane based streamtube model SMART, transport of o-xylene is simulated by considering kinetic sorption and biodegradation as reactive transport processes. As explained in Section 4.2.2 and Section 8.3, biodegradation rates are identified within a stochastic framework by minimizing the objective function, that is defined as the difference between the simulated ensemble averaged mass flow rate and the observed mass flow rate at the downgradient control plane.

Model results are then compared to the results of the integrally applied CSIA method.

9.3.1 Model domain and model set-up

Reactive transport of o-xylene is simulated within the sub-domain that is limited by the two control planes at B47 and B85 (Figure 9.2). It is assumed, that all streamlines starting out at the control plane B47 also reach the control plane B85. Like in the modelling studies performed before, flow in the heterogeneous domain is described by pdfs of travel time, that are obtained from eight realizations consisting of three facies types with different hydraulic properties. The hydraulic conditions are set corresponding to the parameters chosen for the application of the analytical inversion algorithm, as listed in Table 9.1.

The lithological composition of the aquifer material and the physical properties are set according to the summarized facies as explained in Section 7.2.2 and visualized in Figure 7.4. Sorption parameters for o-xylene are estimated according to the concept of Grathwohl & Peschik (1997), as performed earlier for p-xylene (Section 8.3.1), because no experimental data are available for the Neckar valley material and o-xylene. The estimated isotherm parameters are listed in Table 9.5.

Table 9.5 Estimated sorption parameters for o-xylene and the lithological components of the Testfeld Süd' (according to Grathwohl & Peschik, 1997).

Lithological component	K_{fr} [$L \cdot kg^{-1}$] ¹	$1/n_{fr}$ [-]
G_eff	0.21	0.8
Limestone	0.35	0.82
Quartz	0.0035	1

¹ K_{fr} determined for concentrations in $mg \cdot L^{-1}$.

As boundary condition, a constant input concentration of $47.3 \mu g \cdot L^{-1}$, i.e. a constant mass flow rate of $5.93 g \cdot d^{-1}$ is assumed at the upgradient control plane B47 (Table 9.2). Zero-, first- and second-order decay biodegradation rates are inversely estimated by minimizing the difference between simulated ensemble averaged mass

flow rates and the observed mass flow rates at the downgradient control plane at B85.

9.3.2 Model results

The simulations are performed for a period of five years, as steady state conditions are quickly achieved with respect to plume migration, because sorption kinetics of o-xylene is very fast. Thus, mass flow rates are time independent at the downgradient control plane after 5 a.

Assuming biodegradation to follow a zero-order decay, a mean degradation rate constant of $30.35 \mu g \cdot L^{-1} \cdot d^{-1}$ for the ensemble average is determined. This high degradation rate constant and the kinetic sorption cause a mass flow rate reduction from $5.93 g \cdot d^{-1}$ at the upgradient control plane B47 to $0.08 g \cdot d^{-1}$ in the ensemble average at the downgradient control plane (Table 9.6). Assuming first and second-order decay, mean degradation rate constants of $2.1 d^{-1}$ and $0.609 L \cdot d^{-1} \cdot \mu g^{-1}$, respectively, are identified. Unlike for the transport simulations for p-xylene presented in Section 8.3, it is impossible to identify the order of decay, as only one downgradient control plane exists to inversely estimate the degradation rate constant. Thus, it cannot be shown, whether in this case a higher-order decay is justified to simulate the transport of o-xylene.

Nevertheless, in all three cases, biodegradation contributes with more than 99 % to the mass flow rate reduction observed between the two control planes, whereas the sorbed mass of o-xylene is less than 1 %. These results correspond to the results of the transport modelling of p-xylene (Section 8.3), which revealed also a minor role of sorption processes to the overall natural attenuation processes. As the solubilities of both compounds are similar ($198 mg \cdot L^{-1}$ for p-xylene and $175 mg \cdot L^{-1}$ for o-xylene), the sorption behaviour is expected to be similar, i.e. very small in this case.

Table 9.6 Model results for o-xylene: mean degradation rate constants of zero, first and second-order decay and simulated ensemble averaged mass flow rates at control plane B85.

	Mean degradation rate constant ¹ [d ⁻¹ L ⁿ⁻¹ µg ¹⁻ⁿ]	Simulated ensemble averaged mass flow rate at CP B85 ² [g d ⁻¹]
0 order decay	30.35	0.08
1st order decay	2.1	0.08
2nd order decay	0.609	0.07

¹ with n order of decay.

² observed mass flow rate at control plane B85: 0.08 g d⁻¹.

The identified contribution of biodegradation to the observed o-xylene mass flow rate reduction by applying the stochastic modelling approach excellently agrees with the results obtained from the integrally applied CSIA method. As the predicted mean concentration at the downgradient control plane, using the Rayleigh equation, equalled the observed concentration, the complete mass flow rate reduction is attributed to biodegradation, according to the CSIA.

9.4 Summary and conclusions

Integral pumping tests were carried out at the 'Testfeld Süd' in order to quantify biodegradation by (a) a combination of compound-specific isotope analysis (CSIA) and the integral mass flow rate measurement approach and (b) by inverse stochastic transport modelling using measured contaminant mass flow rates as presented in the previous chapters. Instead of using point concentrations and point isotope ratios of wells along a single assumed streamline which might lead to an erroneous quantification of biodegradation, the combination of CSIA with the integral mass flow rate measurement approach enlarges the considered streamline to a streamtube with an extent defined by the maximum isochrones of the pumping tests, thus allowing

for a more reliable determination of the degradation behaviour.

Therefore, two pumping tests in collaboration with the University of Hamburg were performed, each well defining a control plane with the width of the maximum isochrone. Information on the hydraulic situation, including the tracer test results by Bösel (1999) and Herfort (2000) allow the inference, that the streamlines starting out at the upgradient control plane are covered for the most part by the downgradient control plane. Ten samples were taken during each pumping test and contaminant concentrations (BTEX and PAH; analysed by University of Tübingen) as well as their isotope ratios (determined by the University of Hamburg) were analysed.

Already from the qualitative evaluation of the concentration time series and isotope time series, conclusions could be drawn with respect to plume composition, relative plume position as well as to biodegradation of certain compounds. At both wells similar plume compositions are observed with a dominance of benzene and acenaphthene within the group of BTEX and PAH compounds, respectively. Several sources probably caused the observed plume(s), as the relative position of the wells to the plume varies for different compounds. For benzene, the upgradient well lies within the plume, as concentrations are relatively constant with pumping time, whereas concentrations of m,p-xylene increase in both wells, which indicates that both wells are positioned at the margin of the m,p-xylene plume. Generally, a strong decrease in concentrations is observed between the two wells, i.e. concentrations in the downgradient well are by a factor of 3 to 100 smaller than concentrations in the upgradient well. Together with the isotopic shifts observed for several BTEX compounds, this points to high microbial activity between the two wells. Both, benzene and o-xylene show isotopic shifts of 2 - 5 ‰ and 5 - 8 ‰ between the two wells, respectively.

A quantitative evaluation was performed by applying the analytical inversion algorithm to both concentration time series and for the first time to isotope concentration time series in order to determine mean contaminant and isotope concentrations and thus contaminant mass flow rates and mean $\delta^{13}\text{C}$ values across the two control planes. These results served for the quantification of biodegradation of o-xylene by applying the Rayleigh model as well as by inverse stochastic transport modelling. For the first method, mean isotope ratios at both control planes and the mean o-xylene concentration at the upgradient control plane together with a fractionation factor determined in laboratory experiments (Vieth et al., 2001) were used as input for the Rayleigh equation. A mean o-xylene concentration of $0.4 \mu\text{g L}^{-1}$ was thus predicted at the downgradient control plane, which corresponds to a biological reduction of the o-xylene mass by 99 %. The observed mean o-xylene concentration of $0.6 \mu\text{g L}^{-1}$ equals the predicted one within the range of accuracy. Thus, the complete reduction of o-xylene observed between the two wells can be attributed to biodegradation.

These results are excellently confirmed by the stochastic transport modelling which allowed for an inverse determination of biodegradation rate constants. As presented in the previous chapters (4 and 8), a mean biodegradation rate constant was inversely identified by minimizing the difference between the ensemble averaged mass flow rate and the observed mass flow rate at the downgradient control plane. As kinetic sorption is described by the physical process of intraparticle diffusion, the biodegradation rate constant was the only parameter to be identified within the inverse modelling procedure. For o-xylene mean zero-, first- and second-order degradation rate constants of $30.35 \mu\text{g L}^{-1} \text{d}^{-1}$, 2.1 d^{-1} and $0.609 \text{ L } \mu\text{g}^{-1} \text{ d}^{-1}$ were estimated, respectively. Unlike in the previous modelling scenario for p-xylene (see Section 8.3), the order of decay could not be identified reliably,

as information about further control planes was missing. Nevertheless, the estimated zero-, first- and second-order biodegradation rate constants reveal that more than 99 % of the observed mass flow rate reduction between the two control planes can be attributed to biodegradation, whereas sorption contributes less than 1 %. This is in very good agreement with the results of the integrally applied compound-specific isotope analysis and its quantification by the Rayleigh equation.

The significance of these findings is twofold: First, it was shown that an application of the integral mass flow rate approach with its analytical inversion algorithm can be applied to isotope concentrations to obtain mean isotope ratios across control planes. This enlarges the considered area from a single assumed streamline between two wells (e.g. Sherwood Lollar et al., 2001; Sturchio et al., 1998) to two control planes and a laterally extending streamtube in between. This significantly reduces the impact of dilution on the measured mean contaminant concentrations and isotope concentrations. Thus, the assumption of a closed system, necessary for the application of the Rayleigh equation is better justified, than if just a single streamline is considered.

Secondly, the very good agreement between the results obtained from the Rayleigh model and the inverse stochastic transport modelling might indicate that both approaches are useful to quantify biodegradation at field scale. The comparison of both approaches cannot serve as a mutual verification of each method, but they both might serve as a contribution to the “lines of evidence” called for by the US EPA (1999) in order to prove natural attenuation at field sites.

10 Summary and conclusions

The aim of this thesis was the quantification of natural attenuation processes at field scale, demonstrated for the former gasworks site 'Testfeld Süd'.

For the first time, the combined integral measuring and modelling approach was applied at the 'Testfeld Süd' to assess the impact of different natural attenuation processes. Both parts of this combined approach cope with uncertainty caused by subsurface heterogeneity. The integral measuring approach abandons the concept of single point measurements and introduces an integral concentration measurement by enlarging the sample volume. This leads to an integration and thus averaging of the concentration over the sampled volume. Thus, the heterogeneity of the considered volume is accounted for but not spatially resolved. The measured mean concentrations and derived mass flow rates obtained at several control planes then serve as input and conditioning data for the stochastic reactive transport modelling approach. For the first time, concentration and mass flow rate data are used to inversely estimate mean transport parameters within a stochastic framework. As sorption is modelled following the physically based concept of intraparticle diffusion using measured parameters, biodegradation rates can be inversely identified within a stochastic Monte Carlo approach.

To achieve this aim of identifying and quantifying the natural attenuation processes occurring at the 'Testfeld Süd', the following intermediate steps were pursued:

A **geostatistical analysis** was performed to describe and quantify the heterogeneity at the

'Testfeld Süd'. The spatial correlation of the categorical variable 'facies', that hydraulic and geochemical parameters are attributed to, was investigated by the means of indicator variogram analysis. Horizontal correlation lengths were determined to 38 to 60 m, depending on the facies and orientation. Based on these results, aquifer realizations were generated using the sequential indicator simulation algorithm. From 200 realizations, eight realizations were selected according to a selection criterion, that evaluates the quality of the reproduced statistics of each realization. Flow and conservative transport were calculated for each realization to provide the base for the subsequent reactive transport modelling. By analysing the temporal moments of the conservative breakthrough curves, macro-dispersivities were determined, yielding ensemble means of 20 to 33 m for transport distances of 50 to 800 m.

Based on the eight aquifer realizations, a **model comparison** was performed to investigate the applicability of the one-dimensional streamtube model SMART. The control plane based Lagrangian transport model SMART is a favourable tool to simulate natural attenuation, because integrally measured parameters, like contaminant mass flow rates, directly serve as model input. Furthermore, due to its one-dimensionality, computation times are relatively short. The main drawback of SMART is, that it does not account for spatially varying geochemical parameters. This simplification demanded for an investigation of the applicability of the streamtube model SMART for heterogeneous geochemical conditions by comparing it to the fully three-dimensional Eulerian transport model

MT3D-IPD. Different scenarios were performed to compare both model approaches by simulating the reactive transport of the sorbing compound acenaphthene. Sorption was considered in both approaches as intraparticle diffusion. Equally defined scenarios, i.e. assuming homogeneous geochemical conditions, revealed identical results for both model approaches. When heterogeneous geochemical conditions were assumed, SMART and MT3D-IPD results of the realization ensemble were in good agreement for travel distances larger than 100 m. The ensemble average of both approaches also corresponded well for short travel distances and travel times larger nine years. However, the ensemble variance is underestimated by SMART, as it does not account for the uncertainty due to geochemical heterogeneity. For long transport distances, deviations between both approaches were observed, probably caused by numerical dispersion that MT3D-IPD is subject to. It is concluded, that SMART is a useful tool to predict the mean plume behaviour even for heterogeneous geochemical conditions.

Thus, the streamtube model SMART could be used to **model natural attenuation at the 'Testfeld Süd'**. Fate and transport of two compounds, acenaphthene and p-xylene, were simulated within a Monte Carlo approach accounting for the uncertainty due to hydraulic heterogeneity. For acenaphthene, the mean contamination time and boundary mass flow rate were inversely estimated. Different boundary mass flow rates were assumed at a control plane approximately 50 m downgradient of the source, i.e. after naphthalene is depleted and degradation of acenaphthene does not occur. It was found, that only a boundary mass flow rate of approximately 27 g d^{-1} , as it was estimated from point concentration measurements, yields a consistent contamination time of at least 28 years at both downgradient control planes. This value represents a minimum contamination time, as it was determined under the assumption of a constant boundary mass flow rate 50 m downgra-

dient the source. Thus, the time needed until this mass flow rate became constant with time was not accounted for in the simulations. The great impact of kinetic sorption on the transport behaviour of acenaphthene is demonstrated by the simulations. It is shown, that even after 45 years of transport, equilibrium conditions with respect to sorption have not been reached at a distance of 180 m. Thus, kinetic sorption leads to a significant retardation of acenaphthene. However, as degradation of acenaphthene in the absence of naphthalene does not occur and because sorption does not reduce the contaminant mass, natural attenuation cannot be recommended as a remediation alternative for acenaphthene at the 'Testfeld Süd'.

Reactive transport of p-xylene was simulated at the 'Testfeld Süd' accounting for kinetic sorption and biodegradation. Degradation rates were inversely estimated within the Monte Carlo approach representing the uncertainty of hydraulic parameters. The integrally measured mass flow rates were used as conditioning data to minimize the objective function of the inverse problem. Inversely estimated first-order degradation rate constants did not yield satisfactory results for the whole transport distance, if a constant degradation rate constant was assumed. An increase of half-lives from 2 d to 30 d with increasing transport distance was observed. Second-order decay excellently described the observed mass flow rate reduction, assuming a single degradation rate constant of $70.2 \text{ L d}^{-1} \text{ mg}^{-1}$. Thus, the natural attenuation processes, contributing to the observed mass flow rate reduction, could be quantified. Accordingly, biodegradation contributes with more than 99 % to the observed reduction, whereas only 1 % is attributed to sorption. As within a transport distance of 50 m the p-xylene mass flow rate decreases to 0.4 % of the boundary mass flow rate, which is, as mentioned before, mainly caused by biodegradation, natural attenuation could be a remediation alternative at the 'Testfeld Süd' with respect to p-xylene.

The **integral measuring approach was combined with the compound-specific isotope analysis** (CSIA) and compared to results of the modelling approach. The CSIA method allows for an *in situ* quantification of biodegradation by analysing the isotopic shift of contaminants during degradation. By enlarging the considered domain in which degradation is quantified *in situ*, the reliability of CSIA can be increased, as effects of dilution are reduced and furthermore the probability of sampling contaminants, that originate from the same source, is increased. This was realized for the first time by combining CSIA with the integral measuring approach. Results of the integrally applied CSIA method were then compared to results of the modelling approach.

Therefore, two combined integral mass flow rate measurements were performed at the 'Testfeld Süd' in collaboration with the University of Hamburg. Contaminant concentrations as well as isotope ratios of the contaminants were analysed at two control planes along a transect. By the aid of the analytical inversion algorithm, mass flow rates of contaminants and for the first time mean isotope concentrations were determined at both control planes. O-xylene showed a mean isotope shift between the control planes of 5 ‰, which was accompanied by a strong concentration decrease. Applying the Rayleigh equation, it is found, that biodegradation causes a decrease of the upgradient concentration of 99 %. As the thus predicted concentration at the downgradient control plane equals the observed concentration, no further natural attenuation processes contribute to the observed mass flow rate reduction. These results excellently agree with the results obtained from the stochastic reactive transport modelling performed for o-xylene in the considered sub-domain. Zero-, first- and second-order degradation rate constants were inversely identified. All revealed, that 99 % of the simulated mass flow rate reduction is attributed to biodegradation and only 1 % is caused by sorption.

This very good agreement shows, that both approaches, the integrally applied compound-specific isotope analysis as well as the combined integral measuring and modelling approach, are useful tools to assess natural attenuation at field scale.

References

- Acton, D.W. and Barker, J.F., 1992. In situ biodegradation potential of aromatic hydrocarbons in anaerobic aquifers. *Journal of Contaminant Hydrology*, 9: 325-352.
- Ahad, J., Sherwood Lollar, B., Edwards, E., Slater, G. and Sleep, B., 2000. Carbon Isotope Fractionation during Anaerobic Biodegradation of Toluene: Implications for Intrinsic Bioremediation. *Environmental Sciences and Technology*, 34: 892-896.
- Alexander, M., 1999. Biodegradation and Bioremediation. Academic Press, San Diego, 453 pp.
- Allen-King, R.M., Halket, R.M. and Gaylord, D.R., 1998. Characterizing the heterogeneity and correlation of perchloroethene sorption and hydraulic conductivity using a facies-based approach. *Water Resources Research*, 34(3): 385-396.
- Alvarez, P.J. and Vogel, T.M., 1991. Substrate interactions of benzene, toluene, and para-xylene during microbial degradation by pure cultures and mixed culture aquifer slurries. *Applied and Environmental Microbiology*, 57: 2981-2985.
- Anderson, M.P., 1989. Hydrogeologic facies models to delineate large-scale spatial trends in glacial and glaciofluvial sediments. *Geological Society of America Bulletin*, 101: 501-511.
- Appelo, C.A.J. and Postma, D., 1996. Geochemistry, groundwater and pollution. Balkema, Rotterdam, 536 pp.
- Ball, W.P. and Roberts, P.V., 1991. Long-term sorption of halogenated organic chemicals by aquifer material. 2. Intraparticle diffusion. *Environmental Sciences and Technology*, 25: 1237-1249.
- Barber, L.B., Thurman, E.M. and Runnels, D.D., 1992. Geochemical heterogeneity in a sand and gravel aquifer; effect of sediment mineralogy and particle size on the sorption of chlorobenzenes. *Journal of Contaminant Hydrology*, 9: 35-54.
- Beller, H.R., Grbic-Galic, D. and Reinhard, M., 1992. Microbial Degradation of Toluene under Sulfate-Reducing Conditions and the Influence of Iron on the Process. *Applied and Environmental Microbiology*, 58(3): 786-793.
- Berry, D.F., Francis, A.J. and Bollag, J.M., 1987. Microbial metabolism of homocyclic and heterocyclic aromatic compounds under anaerobic conditions. *Microbiological Reviews*, 51(1): 43-59.
- Bloom, Y., Aravena, R., Hunkeler, D., Edwards, E. and Frape, S.K., 2000. Carbon isotope fractionation during microbial dechlorination of trichloroethene, cis-1,2-dichloroethene, and vinyl chloride: implications for assessment of natural attenuation. *Environmental Sciences and Technology*, 34(13): 2768-2772.
- Bockelmann, A., Ptak, T. and Teutsch, G., 2001. An analytical quantification of mass fluxes and natural attenuation rate constants at a former gasworks site. *Journal of Contaminant Hydrology*, 53(3-4): 407-427.
- Bockelmann, A., submitted. Natural attenuation of organic contaminants in heterogeneous porous media: Integral mass flux quantification and reactive transport modelling. *Tübinger Geowissenschaftliche Arbeiten* (TGA), Reihe C.
- Borden, C.R., Daniel, R.A., LeBrun, L.E. and Davis, C.W., 1997. Intrinsic biodegradation of MTBE and BTEX. *Water Resources Research*, 33(5): 1105-1115.
- Bosma, W.J.P. and Van der Zee, S.E.A.T.M., 1993. Transport of Reacting Solute in a One-Dimensional, Chemically Heterogeneous Porous Medium. *Water Resources Research*, 29(1): 117-131.
- Bösel, D., 1999. Entwicklung eines Strömungs- und Transportmodells für das Testfeld Süd (Neckartal bei Stuttgart) - Felderkundung und Tiefenkartierung. Diplomarbeit, Universität Tübingen. 102 pp.
- Brady, P., Brady, M. and Borns, D., 1998. Natural Attenuation - CERCLA, RBCA's, and the Future of Environmental Remediation. Lewis Publishers, New York, 245 pp.

- Burr, D.T., Sudicky, E.A. and Naff, R.L., 1994. Nonreactive and reactive solute transport in three-dimensional heterogeneous porous media: Mean displacement, plume spreading and uncertainty. *Water Resources Research*, 30(3): 791-815.
- Capilla, J.E., Gómez-Hernández, J.J. and Sahuquillo, A., 1998. Stochastic simulation of transmissivity fields conditional to both transmissivity and piezometric head data - 3. Application to the Culebra Formation at the Waste Isolation Pilot Plan (WIPP), New Mexico, USA. *Journal of Hydrology*, 207: 254-269.
- Chapelle, F.H., 1993. Ground water microbiology and geochemistry. Wiley, New York, 424 pp.
- Christensen, T. H., Bjerg, P. L., Banwart, S. A., Jakobsen, R., Heron, G. and Albrechtsen, H. J., 2000. Characterization of redox conditions in groundwater contaminant plumes. *Journal of Contaminant Hydrology*, 45: 165-241.
- Cirpka, O.A. and Kitanidis, P.K., 2000a. An advective-dispersive stream tube approach for the transfer of conservative-tracer data to reactive transport. *Water Resources Research*, 36(5): 1209-1220.
- Cirpka, O.A. and Kitanidis, P.K., 2000b. Characterization of mixing and dilution in heterogeneous aquifers by means of local temporal moments. *Water Resources Research*, 36(5): 1221-1236.
- Clark, I. and Fritz, P., 1997. Environmental Isotopes in Hydrogeology. Lewis Publishers, New York, 328 pp.
- Cpty, N. and Rubin, Y., 1995. A stochastic approach to the characterization of lithofacies from surface seismic and well data. *Water Resources Research*, 31: 1673-1686.
- Cvetkovic, V. and Dagan, G., 1994. Transport of kinetically sorbing solute by steady random velocity in heterogeneous porous formations. *Journal of Fluid Mechanics*, 265: 189-215.
- Dagan, G., 1984. Solute transport in heterogeneous porous formations. *Journal of Fluid Mechanics*, 145: 151-177.
- Dagan, G., 1986. Statistical Theory of Groundwater Flow and Transport: Pore to Laboratory, Laboratory to Formation, and Formation to Regional Scale. *Water Resources Research*, 22(9): 120S-134S.
- Dagan, G., 1988. Time-Dependent Macrodispersion for Solute Transport in Anisotropic Heterogeneous Aquifers. *Water Resources Research*, 24(9): 1491-1500.
- Dagan, G. and Rubin, Y., 1988. Stochastic Identification of Recharge, Transmissivity, and Storativity in Aquifer Transient Flow: A Quasi-Steady Approach. *Water Resources Research*, 24(10): 1698-1710.
- Dagan, G., 1989. Flow and Transport in Porous Formations. Springer-Verlag, Berlin, 465 pp.
- Dagan, G., 1990. Transport in Heterogeneous Porous Formations: Spatial Moments, Ergodicity and Effective Dispersion. *Water Resources Research*, 26(6): 1281-1290.
- Dagan, G., 1991. Dispersion of a passive solute in non-ergodic transport by steady velocity fields in heterogeneous formations. *Journal of Fluid Mechanics*, 233: 197-210.
- Dagan, G. and Cvetkovic, V., 1996. Reactive transport and immiscible flow in geological media. I. General theory. *Proceedings of the Royal Society of London*, A452: 285-301.
- Dagan, G., 1997. Stochastic modeling of flow and transport: the broad perspective. In: G. Dagan and S.P. Neuman (Editors), *Subsurface Flow and Transport: A Stochastic Approach*. International Hydrology Series. Cambridge University Press, Cambridge, pp. 3-19.
- Dagan, G. and Neuman, S.P. (Editors), 1997. *Subsurface Flow and Transport: A Stochastic Approach*. International Hydrology Series. Cambridge University Press, Cambridge, 241 pp.
- Davis, J.M., Lohmann, R.C., Phillips, F.M., Wilson, J.L. and Love, D.W., 1993. Architecture of the Sierra Ladrones Formation, Central New Mexico: Depositional controls on the permeability correlation structure. *Geological Society of America Bulletin*, 105: 998-1007.
- Davis, J.W., Klier, N.J. and Carpenter, C.L., 1994. Natural biological attenuation of benzene in ground water beneath a manufacturing facility. *Ground Water*, 32(4): 215-226.
- Davis, G. B., Barber, C., Power, T. R., Thierrin, J., Patterson, B. M., Rayner, J. L. and Wu, Q., 1999. The variability and intrinsic remediation of a BTEX plume in anaerobic sulphate-rich groundwater. *Journal of Contaminant Hydrology*, 36: 265-290.
- De Marsily, G., 1986. *Quantitative Hydrogeology - Groundwater Hydrology for Engineers*. Academic Press, San Diego, 440 pp.

- De Marsily, G., Delay, F., Teles, V. and Schafmeister, M.T., 1998. Some current methods to represent the heterogeneity of natural media in hydrogeology. *Hydrogeology Journal*, 6: 115-130.
- Dempster, H.S., Sherwood Lollar, B. and Feenstra, S., 1997. Tracing organic contaminants in groundwater: a new methodology using compound-specific isotopic analysis. *Environmental Sciences and Technology*, 31(11): 3193-3197.
- Desbarats, A.J. and Bachu, S., 1994. Geostatistical analysis of aquifer heterogeneity from the core scale to the basin scale: A case study. *Water Resources Research*, 30(3): 673-684.
- Deutsch, C.V. and Journel, A.G., 1992. *GSLIB - Geostatistical Software Library and User's Guide*. Oxford University Press, Oxford, 340 pp.
- Edwards, E. and Grbic-Galic, D., 1992. Complete Mineralization of Benzene by Aquifer Microorganisms under Strictly Anaerobic Conditions. *Applied and Environmental Microbiology*, 58(8): 2663-2666.
- Edwards, E.A., Wills, L.E., Reinhard, M. and Grbic-Galic, D., 1992. Anaerobic degradation of toluene and xylene by aquifer microorganisms under sulfate-reducing conditions. *Applied and Environmental Microbiology*, 58: 794-800.
- Evans, P.J., Mang, D.T. and Young, L.Y., 1991. Degradation of toluene and m-xylene and transformation of o-xylene by denitrifying enrichment cultures. *Applied and Environmental Microbiology*, 57: 450-454.
- Finkel, M., Liedl, R. and Teutsch, G., 1998. Modelling Surfactant Influenced PAH Migration. *Physics and Chemistry of the Earth*, 23(2): 245-250.
- Finkel, M., 1999. Quantitative Beschreibung des Transports von polzyklischen aromatischen Kohlenwasserstoffen (PAK) und Tensiden in porösen Medien. *Tübinger Geowissenschaftliche Arbeiten (TGA)*, C47, 96 pp.
- Fiori, A. and Bellin, A., 1999. Non-ergodic transport of kinetically sorbing solutes. *Journal of Contaminant Hydrology*, 40: 201-219.
- Fiori, A. and Dagan, G., 2000. Concentration fluctuations in aquifer transport: a rigorous first-order solution and applications. *Journal of Contaminant Hydrology*, 45: 139-163.
- Freeze, R.A., 1975. A stochastic conceptual analysis of one-dimensional flow in non-uniform homogeneous media. *Water Resources Research*, 11(5): 725-741.
- Gelhar, L.W. and Axness, C.L., 1983. Three-dimensional stochastic analysis of macrodispersion in aquifers. *Water Resources Research*, 19(1): 161-180.
- Gelhar, L.W., 1986. Stochastic Subsurface Hydrology - From Theory to Applications. *Water Resources Research*, 22(9): 135S-145S.
- Gelhar, L.W., 1993. Stochastic subsurface hydrology. Prentice-Hall, Englewood Cliffs, New Jersey, 390 pp.
- Gieg, L. M., Kolhatkar, R. V., McInerney, M. J., Tanner, R. S., Harris, S. H., Sublette, K. L. and Suflita, J. M., 1999. Intrinsic bioremediation of petroleum hydrocarbons in a gas condensate-contaminated aquifer. *Environmental Sciences and Technology*, 33: 2550-2560.
- Ginn, T.R., Simmons, C.S. and Wood, B.D., 1995. Stochastic-convective transport with nonlinear reaction: biodegradation with microbial growth. *Water Resources Research*, 31(11): 2689-2700.
- Ginn, T.R., Murphy, E.M., Chilakapati, A. and Seeboonruang, U., 2001. Stochastic-convective transport with nonlinear reaction and mixing: application to intermediate-scale experiments in aerobic biodegradation in saturated porous media. *Journal of Contaminant Hydrology*, 48(121-149).
- Ginn, T.R., 2001. Stochastic-convective transport with nonlinear reactions and mixing: finite streamtube ensemble formulation for multicomponent reaction systems with intra-streamtube dispersion. *Journal of Contaminant Hydrology*, 47: 1-28.
- GLA, 1989. Hydrogeologisches Gutachten zur Verunreinigung der Untergrundes und des Grundwassers durch Gaswerksrückstände im Bereich des Erdgasspeichers auf dem Gelände der Technischen Werke Stuttgart. *Geologisches Landesamt Baden-Württemberg*, Stuttgart.
- GLA, 1992. Hydrogeologisches Gutachten zur Grundwasser-Abstromüberwachung der kontaminierten Bereiche im ehemaligen Gaswerksgelände der Technischen Werke Stuttgart in der Neckar-Talaue. *Geologisches Landesamt Baden-Württemberg*, Stuttgart.

- GLA, 1993. Mathematisches Grundwassерmodell Gaswerk Gaisburg - Hydrogeologisches Gutachten zur Quantifizierung der Grundwassersituation im Bereich des Gaswerks Gaisburg und seiner Umgebung. Geologisches Landesamt Baden-Württemberg, Stuttgart.
- Grathwohl, P., 1990. Influence of Organic Matter from Soils and Sediments from Various Origins on the Sorption of Some Chlorinated Aliphatic Hydrocarbons: Implications on Koc Correlations. *Environmental Sciences and Technology*, 24: 1687-1693.
- Grathwohl, P. and Kleineidam, S., 1995. Impact of heterogeneous aquifer materials on sorption capacities and sorption dynamics of organic contaminants, *Groundwater Quality: Remediation and Protection*. IAHS Publication 225, Prague, pp. 79-86.
- Grathwohl, P. and Peschik, G., 1997. Permeable Sorptive Walls for Treatment of hydrophobic organic Contaminant Plumes in Groundwater, International Conference on Contaminant Technology, St. Petersburg, Florida.
- Grathwohl, P., 1998. Diffusion in Natural Porous Media: Contaminant Transport, Sorption, Desorption and Dissolution Kinetics. Kluwer Academic Publishers, Boston, 228 pp.
- Grbic-Galic, D. and Vogel, T.M., 1987. Transformation of Toluene and Benzene by Mixed Methanogenic Cultures. *Applied and Environmental Microbiology*, 53(2): 254-260.
- Hassan, A.E., Cushman, J.H. and Delleur, J.W., 1998. Significance of porosity variability to transport in heterogeneous porous media. *Water Resources Research*, 34(9): 2249-2259.
- Hayes, J.M., Freeman, K.H., Popp, B.N. and Hoham, C.H., 1990. Compound-specific isotopic analyses; a novel tool for reconstruction of ancient biogeochemical processes. *Organic Geochemistry*, 16: 1115-1128.
- Hendricks Franssen, H.J.W.M., Gómez-Hernández, J.J. and Sahuquillo, A., 2001. The worth of concentration data for aquifer characterisation, 26th General Assembly of the European Geophysical Society. EGS, Nice, France.
- Herfort, M., Ptak, T., Liedl, R. and Teutsch, G., 1999. A New Approach for the Investigation of Natural Attenuation at Field Scale. In: C.D. Johnston (Editor), *Contaminated Site Remediation: Challenges Posed by Urban and Industrial Contaminants*. Centre for Groundwater Studies, Fremantle, Australia, pp. 383-390.
- Herfort, M., 2000. Reactive Transport of Organic Compounds within a Heterogeneous Porous Aquifer. *Tübinger Geowissenschaftliche Arbeiten* (TGA), C54, 76 pp.
- Hess, K.M., Wolf, S.H. and Celia, M.A., 1992. Large-scale natural gradient tracer test in sand and gravel, Cape Cod, Massachusetts. 3. Hydraulic conductivity variability and calculated macrodispersivities. *Water Resources Research*, 28(8): 2011-2027.
- Hetterschijt, R.A.A., Te Stroet, C.B.M. and Bosma, T.N.P., 1999. Estimation of sequential degradation rates of perchloroethylene by "history matching". In: F. Stauffer, W. Kinzelbach, K. Kovar and E. Hoehn (Editors), *ModelCARE '99: Calibration and Reliability in Groundwater Modelling: Coping with Uncertainty*. IAHS Publication 265, pp. 468-473.
- Hoeksema, R.J. and Kitanidis, P.K., 1984. An Application of the Geostatistical Approach to the Inverse Problem in Two-Dimensional Groundwater Modeling. *Water Resources Research*, 20(7): 1003-1020.
- Holder, T., Teutsch, G., Ptak, T. and Schwarz, R., 1998. A new approach for source zone characterization: the Neckar Valley study. In: M. Herbert and K. Kovar (Editors), *GQ'98 Groundwater Quality: Remediation and Protection*. IAHS Publication 250, pp. 49-55.
- Holder, T., 1999. Orientierende Erkundung E1-2, Gaswerk der Neckarwerke Stuttgart AG, Talstr.117 – Analytische Auswertung der Immissionspumpversuche. Lehrstuhl für Angewandte Geologie, Universität Tübingen, 15 pp.
- Holder, T. and Teutsch, G., 2000. Standortmodell für das Gelände des ehemaligen Gaswerks, Talstr. 117, Stuttgart-Ost. Zentrum für Angewandte Geologie, Universität Tübingen, Tübingen.
- Howard, P.H., Boethling, R.S., Jarvis, W.F., Meylan, W.M. and Michalenko, E.M., 1991. *Handbook of environmental degradation rates*. Lewis Publishers, Chelsea, 725 pp.
- Hu, B.X. and Cushman, J.H., 1997. Comparison of nonlocal Eulerian to Lagrangian moments for transport in an anisotropic heterogeneous aquifer with deterministic linear nonequilibrium sorption. *Water Resources Research*, 33(4): 891-896.

- Hubbard, A.S., Rubin, Y. and Majer, E., 1999. Spatial correlation structure estimation using geophysical and hydrogeological data. *Water Resources Research*, 35(6): 1809-1825.
- Huggenberger, P. and Aigner, T., 1999. Introduction to the special issue on aquifer-sedimentology: problems, perspectives and modern approaches. *Sedimentary Geology*, 129: 179-186.
- Hunkeler, D., Höhener, P., Bernasconi, S. and Zeyer, J., 1999. Engineered in situ bioremediation of a petroleum hydrocarbon-contaminated aquifer: assessment of mineralization based on alkalinity, inorganic carbon and stable carbon isotope balances. *Journal of Contaminant Hydrology*, 37: 201-223.
- Hunkeler, D., Aravena, R. and Butler, B.J., 1999. Monitoring Microbial Dechlorination of Tetrachloroethene (PCE) in Groundwater Using Compound-Specific Stable Carbon Isotope Ratios: Microcosm and Field Studies. *Environmental Sciences and Technology*, 33: 2733-2738.
- Hunkeler, D. and Aravena, R., 2000. Determination of Compound-Specific Carbon Isotope Ratios of Chlorinated Methanes, Ethanes, and Ethenes in Aqueous Samples. *Environmental Sciences and Technology*, 34(13): 2839-2844.
- Hunkeler, D., Butler, B., Aravena, R. and Barker, J., 2001. Monitoring Biodegradation of Methyl tert-Butyl Ether (MTBE) Using Compound-Specific Carbon Isotope Analysis. *Environmental Sciences and Technology*, 35: 676-681.
- Hunkeler, D., Andersen, N., Aravena, R., Bernasconi, S.M. and Butler, B.J., 2001. Hydrogen and Carbon isotope fractionation during aerobic biodegradation of benzene. *Environmental Sciences and Technology*, 35: 3462-3467.
- Hutchins, S.R., Sewell, G.W., Kocav, D.A. and Smith, G.A., 1991. Biodegradation of aromatic hydrocarbons by aquifer microorganisms under denitrifying conditions. *Environmental Sciences and Technology*, 25: 68-76.
- Isaaks, E.H. and Srivastava, R.M., 1989. Applied Geostatistics. Oxford University Press, New York, 561 pp.
- Jäger, R., 1996. Modellierung nichtlinearer Intra-Partikel-Diffusion in heterogenem Aquifermaterial. Diplomarbeit, Universität Tübingen, 56 pp.
- Jäger, R. and Liedl, R., 2000. Prognose der Sorptionskinetik organischer Schadstoffe in heterogenem Aquifermaterial. *Grundwasser*, 2: 57-66.
- Journel, A. and Huijbregts, C., 1978. Mining geostatistics. Academic Press New York, 590 pp.
- Journel, A.G., 1983. Non-parametric estimation of spatial distributions. *Mathematical Geology*, 15(3): 445-468.
- Jungbauer + Partner, 1994. Historische Erkundung und Erhebung des Sachstandes auf dem Gaswerksgelände der TWS AG in Stuttgart-Gaisburg. Jungbauer + Partner, GmbH, Stuttgart.
- Jussel, P., Stauffer, F. and Dracos, T., 1994a. Transport modeling in heterogeneous aquifers: 1. Statistical description and numerical generation of gravel deposits. *Water Resources Research*, 30(6): 1803-1817.
- Jussel, P., Stauffer, F. and Dracos, T., 1994b. Transport modeling in heterogeneous aquifers: 2. Three-dimensional transport model and stochastic numerical tracer experiments. *Water Resources Research*, 30(6): 1819-1831.
- Karapanagioti, H.K., Kleineidam, S., Sabatini, D., Grathwohl, P. and Ligouis, B., 2000. Impacts of Heterogeneous Organic Matter on Phenanthrene Sorption: Equilibrium and Kinetic Studies with Aquifer Material. *Environmental Sciences and Technology*, 34: 406-414.
- Karickhoff, S.W., Brown, D.S. and Scott, T.A., 1979. Sorption of hydrophobic pollutants on natural sediments. *Water Research*, 13(3): 241-248.
- Karickhoff, S.W., 1984. Organic pollutant sorption in aquatic systems. *Journal of Hydraulic Engineering*, 10(6): 707-735.
- Kelly, W.R., Hornberger, G.M., Herman, J.S. and Mills, A.L., 1996. Kinetics of BTX biodegradation and mineralisation in batch and column systems. *Journal of Contaminant Hydrology*, 23: 113-132.
- Kinzelbach, W., 1992. Numerische Methoden zur Modellierung des Transports von Schadstoffen im Grundwasser. Schriftenreihe Wasser - Abwasser. Oldenbourg, München, 343 pp.
- Kitanidis, P.K. and Vomvoris, E.G., 1983. A geostatistical approach to the inverse problem in groundwater modeling (steady state) and one dimensional simulations. *Water Resources Research*, 19(3): 677-690.

- Kitanidis, P.K., 1988. Prediction by the method of moments of transport in a heterogeneous formation. *Journal of Hydrology*, 102(1-4): 453-473.
- Kitanidis, P.K., 1994. The concept of the dilution index. *Water Resources Research*, 30(7): 2011-2026.
- Kleineidam, S., Rügner, H. and Grathwohl, P., 1999. Impact of grain scale heterogeneity on slow sorption kinetics. *Environmental Toxicology and Chemistry*, 18(8): 1673-1678.
- Koltermann, C.E. and Gorelick, S.M., 1996. Heterogeneity in sedimentary deposits: A review of structure-imitating, process-imitating, and descriptive approaches. *Water Resources Research*, 32(9): 2617-2658.
- Kreft, A. and Zuber, A., 1978. On the physical meaning of the dispersion equation and its solution for different initial and boundary conditions. *Chemical Engineering Science*, 33: 1471-1480.
- Kremer, F.V., 1999. Applications of Monitored Natural Attenuation in the United States. In: NATO Special Session Monitored Natural Attenuation, Angers, France, pp. 24-27.
- Kruseman, G.P. and de Ridder, N.A., 1990. Analysis and Evaluation of Pumping Test Data. International Institute for Land Reclamation and Improvement Wageningen.
- Kuiper, A.K., 1986. A Comparison of Several Methods for the Solution of the Inverse Problem in Two-Dimensional Steady State Groundwater Flow Modeling. *Water Resources Research*, 22(5): 705-714.
- Lahvis, M.A., Baehr, A.L. and Baker, R.J., 1999. Quantification of aerobic biodegradation and volatilization rates of gasoline hydrocarbons near the water table under natural attenuation conditions. *Water Resources Research*, 35(3): 753-765.
- LfU, 1990. Erkundung ehemaliger Gaswerksstandorte. Materialien zur Altlastenbearbeitung, 1. Landesanstalt für Umweltschutz Baden-Württemberg, Karlsruhe.
- Liedl, R. and Bold, S., 2001. Reaktiver Transport in Technischen Reaktoren. SAFIRA - Teilprojekt B4.1, Zentrum für Angewandte Geowissenschaften, Tübingen.
- Liedl, R. and Ptak, T., submitted. Modelling of diffusion-limited retardation of contaminants in hydraulically and lithologically non-uniform aquifers. *Journal of Contaminant Hydrology*.
- Lovley, D.R., Woodward, J.C. and Chapelle, F.H., 1996. Rapid anaerobic benzene oxidation with a variety of chelated Fe(III) forms. *Applied and Environmental Microbiology*, 62: 288-291.
- Mackenbrock, U., Kopp-Holtwiesche, B. and Blank, W., 1994. Zur biologischen Abbaubarkeit von Industriechemikalien. *TerraTech*, 4: 41-51.
- Mariotti, A., 1986. La dénitification dans les eaux souterraines, principes et méthodes de son identification: une revue. *Journal of Hydrology*, 88: 1-23.
- Matheron, G., 1971. The theory of regionalized variables and its application. *Les Cahiers du Centre de Morphologie Mathématique de Fontainebleau*, 5: 211.
- McDonald, M.G. and Harbaugh, A.W., 1988. A modular three-dimensional finite-difference ground-water flow model. Open-File Report 83-875, U.S. Geological Survey, Washington.
- Meckenstock, R., Morasch, B., Warthmann, R., Schink, B., Annweiler, E., Michaellis, W. and Richnow, H., 1999. $^{13}\text{C}/^{12}\text{C}$ isotope fractionation of aromatic hydrocarbons during microbial degradation. *Environmental Microbiology*, 1(5): 409-414.
- Miall, A.D., 1992. Alluvial deposits. In: R. Walker and N. James (Editors), *Facies Models*. Geological Association of Canada., Ontario, pp. 119-142.
- Miall, A.D., 1996. *The Geology of Fluvial Deposits - Sedimentary Facies, Basin Analysis, and Petroleum Geology*. Springer-Verlag, Berlin, 582 pp.
- Miralles-Wilhelm, F., Gelhar, L.W. and Kapoor, V., 1997. Stochastic analysis of oxygen-limited biodegradation in three-dimensionally heterogeneous aquifers. *Water Resources Research*, 33(6): 1251-1263.
- Mishra, A.K. and Gutjahr, A., 1999. Transverse Dispersion of a Kinetically Sorbing Solute. *Mathematical Geology*, 31(7): 771-791.
- Mormile, M.R., Liu, S. and Sulfita, J.M., 1994. Anaerobic biodegradation of gasoline oxygenates: Extrapolation of information to multiple site and redox conditions. *Environmental Sciences and Technology*, 28(9): 1727-1732.

- NATO/CCMS, 1999. Evaluation of Demonstrated and Emerging Technologies for the Treatment of Contaminated Land and Groundwater (Phase III), Special Session on Monitored Natural Attenuation, Angers, France.
- NICOLE, 1998. Presented talks at the NICOLE network meeting held on 22.-23.10.1998 at EniTecnologie, Rome. NICOLE secretariat, Rome.
- Nielsen, P.H. and Christensen, T.H., 1994. Variability of biological degradation of aromatic hydrocarbons in an aerobic aquifer determined by laboratory batch experiments. *Journal of Contaminant Hydrology*, 15: 305-320.
- Peter, A., Liedl, R., Ptak, T. and Teutsch, G., 2001. Reactive transport modelling using a control plane based measuring and modelling approach, International Workshop "Prospects and Limits of Natural Attenuation at Tar Oil Contaminated Sites", Dresden, Germany.
- Peter, A., Liedl, R., Ptak, T. and Teutsch, G., in print. Comparing two approaches for modelling natural attenuation of organic compounds in heterogeneous porous media. In: H. Schulz and G. Teutsch (Editors), *Geochemical Processes - Concepts for Modelling Reactive Transport in Soils and Groundwater*. VCH Wiley.
- Piepenbrink, M., in preparation. Lab and field based partitioning and interfacial tracer tests (PITTs) for detection, estimation and dissolution performance assessment of non-aqueous phase liquids. *Tübinger Geowissenschaftliche Arbeiten (TGA)*, Reihe C.
- Pignatello, J.J., 1989. Sorption dynamics of organic compounds in soils and sediments. In: B.L. Sawney and K. Brown (Editors), *Reactions and movement of organic chemicals in soils*. Soil Science Society of America, Madison, Wisconsin, pp. 45-81.
- Ptak, T., 1993. Stofftransport in heterogenen Porenquiferen: Felduntersuchungen und stochastische Modellierung. Mitteilungen Institut für Wasserbau, Heft 80. Universität Stuttgart, 176 pp.
- Ptak, T., Schwarz, R., Holder, T. and Teutsch, G., 2000. Ein neues integrales Verfahren zur Quantifizierung der Grundwasserimmission, Teil II: Numerische Lösung und Anwendung in Eppelheim. *Grundwasser*, 4: 176-183.
- Ptak, T. and Teutsch, G., 2000. Development and application of an integral investigation method for the characterization of groundwater contamination, *ConSoil 2000 - Contaminated Soil*. Thomas Telford Publishing, Leipzig, Germany, pp. 198-205.
- Pyka, W., 1994. Freisetzung von Teerinhaltstoffen aus residualer Teerphase in das Grundwasser: Laboruntersuchungen zur Lösungsrate und Lösungsvermittlung. *Tübinger Geowissenschaftliche Arbeiten (TGA)*, C21, 76 pp.
- Rauber, M., Stauffer, F., Huggenberger, P. and Dracos, T., 1998. A numerical three-dimensional conditioned/unconditioned stochastic facies type model applied to a remediation well system. *Water Resources Research*, 34(9): 2225-2233.
- Rehfeldt, K.R., Boggs, J.M. and Gelhar, L.W., 1992. Field study of dispersion in a heterogeneous aquifer. 3. Geostatistical analysis of hydraulic conductivity. *Water Resources Research*, 28(12): 3309-3324.
- Reichle, R., Kinzelbach, W. and Kinzelbach, H., 1998. Effective parameters in heterogeneous and homogeneous transport models kinetic sorption. *Water Resources Research*, 34(4): 583-594.
- Rice, D. W., Dooher, B. P., Cullen, S. J., Everett, L. G., Kastenberg, W. E., Grose, R. D. and Marino, M. A., 1995. Recommendations to improve the cleanup process for California's leaking underground fuel tanks (LUFTs). UCRL-AR-121762, Lawrence Livermore National Laboratory, Environmental Protection Department.
- Ries, J., 1998. Beprobung gaswerkspezifischer Schadstoffe im Abstrom des "Testfeld Süd". Diplomarbeit, Universität Tübingen, 85 pp.
- Ritzi, R.W., Jayne, D.F., Zahradnik, A.J., Field, A.A. and Fogg, G.E., 1994. Geostatistical modeling of heterogeneity in glaciofluvial, buried-valley aquifers. *Ground Water*, 32(4): 666-674.
- Ritzi, R. W., Dominic, D. F., Brown, N. R., Kausch, K. W., McAlenney, P. J. and Basial, M. J., 1995. Hydrofacies distribution and correlation in the Miami Valley aquifer system. *Water Resources Research*, 31(12): 3271-3281.
- Ritzi, R.W., 2000. Behaviour of indicator variograms and transition probabilities in relation to the variance in lengths of hydrofacies. *Water Resources Research*, 36(11): 3375-3381.

- Robin, M.J.L., Sudicky, E.A., Gillham, R.W. and Kachanoski, R.G., 1991. Spatial Variability of Strontium Distribution Coefficients and Their Correlation With Hydraulic Conductivity in the Canadian Forces Base Borden Aquifer. *Water Resources Research*, 27(10): 2619-2632.
- Rubin, Y. and Dagan, G., 1987a. Stochastic identification of transmissivity and effective recharge in steady groundwater flow. 1. Theory. *Water Resources Research*, 23(7): 1185-1192.
- Rubin, Y. and Dagan, G., 1987b. Stochastic identification of transmissivity and effective recharge in steady groundwater flow. 2. Case study. *Water Resources Research*, 23(7): 1193-1200.
- Rubin, Y., Lobo-Ferreira, J.P., Rodrigues, J.D. and Dagan, G., 1990. Estimation of the hydraulic parameters of the Rio-Maior Aquifer in Portugal by using stochastic inverse modeling. *Journal of Hydrology*, 118(1-4): 257-279.
- Ruud, N.C., Harter, T., Weissmann, G.S. and Fogg, G.E., 2000. Conditional geostatistical modelling of an alluvial aquifer system characterized by poor-quality shallow groundwater. In: F. Stauffer, W. Kinzelbach, K. Kovar and E. Hoehn (Editors), *ModelCARE 99: Calibration and Reliability in Groundwater Modelling: Coping with Uncertainty*. IAHS Publication 265, pp. 360-366.
- Rügner, H., Kleineidam, S. and Grathwohl, P., 1997. Sorptionsverhalten organischer Schadstoffe in heterogenem Aquifermaterial am Beispiel des Phenanthrens. *Grundwasser*, 3: 133-138.
- Rügner, H., Kleineidam, S. and Grathwohl, P., 1999. Long Term Sorption Kinetics of Phenanthrene in Aquifer Materials. *Environmental Sciences and Technology*, 33: 1645-1651.
- Salanitro, J. P., Dorn, P. B., Huesemann, M. H., Moore, K. O., Rhodes, I. A., Jackson, L. M. R., Vipond, T. E., Western, M. M. and Wisniewski, H. L., 1997. Crude Oil Hydrocarbon Bioremediation and Soil Ecotoxicity Assessment. *Environmental Sciences and Technology*, 31(6): 1769-1776.
- Sánchez-Vila, X., Girardi, J.P. and Carrera, J., 1995. A synthesis of approaches to upscaling of hydraulic conductivity. *Water Resources Research*, 31(4): 867-882.
- Schad, H., 1993. Geostatistical analysis of hydraulic conductivity related data based on core samples from a heterogeneous fluvial aquifer. In: V. Capasso, G. Girone and D. Posa (Editors), *International workshop on statistics of spatial processes: Theory and Applications*, Bari, Italy, pp. 205-212.
- Schad, H., 1997. Variability of Hydraulic Parameters in Non-Uniform Porous Media: Experiments ad Stochastic Modelling at Different Scales. *Tübinger Geowissenschaftliche Arbeiten (TGA)*, C35, 233 pp.
- Schettler, I., 1998. Tiefenhorizontierte Schadstoffverteilung im Grundwasser eines Gaswerksstandortes (Testfeld Süd): Felderprobung von Multilevelpackersystemen und Laborversuche zur Eignung von Probenahmeschläuchen. Diplomarbeit, Universität Tübingen.
- Schiedek, T., Grathwohl, P. and Teutsch, G., 1997. Literaturstudie zum natürlichen Rückhalt/Abbau von Schadstoffen im Grundwasser. Lehrstuhl für Angewandte Geologie, Tübingen, 51 pp.
- Schirmer, M., Butler, B.J., Roy, J.W., Frind, E.O. and Barker, J.F., 1999. A relative-least-squares technique to determine unique Monod kinetic parameters of BTEX compounds using batch experiments. *Journal of Contaminant Hydrology*, 37: 69-86.
- Schroth, M.H., Kleikemper, J., Bolliger, C., Bernasconi, S.M. and Zeyer, J., 2001. In situ assessment of microbial sulfate reduction in a petroleum-contaminated aquifer using push-pull tests and stable sulfur isotope analyses. *Journal of Contaminant Hydrology*, 51: 179-195.
- Schüth, C. and Grathwohl, P., 1994. Nonequilibrium Transport of PAHs: A Comparison of Column and Batch Experiments. In: T. Dracos and F. Stauffer (Editors), *IAHR/AIRH International Symposium on Transport and Reactive Processes in Aquifers*. Balkema, Rotterdam, pp. 143-148.
- Schwarz, R., Ptak, T., Holder, T. and Teutsch, G., 1998. Groundwater risk assessment at contaminated sites: a new investigation approach. In: M. Herbert and K. Kovar (Editors), *GQ'98 Groundwater Quality: Remediation and Protection*. IAHS Publication 250, pp. 68-71.
- Schwarz, R., submitted. Grundwasser-Gefährdungsabschätzung durch Emmissions- und Immissionsmessungen an Deponien und Altlasten. *Tübinger Geowissenschaftliche Arbeiten (TGA)*, Reihe C.
- Schwarzenbach, R., Gschwend, P. and Imboden, D., 1993. Environmental organic chemistry. Wiley, New York, 681 pp.
- Selifonov, S. A., Chapman, P. J., Akkerman, S. B., Gurst, J. E., Bortiatynski, J. M., Nanny, M. A. and Hatcher, P. G., 1998. Use of ¹³C nuclear magnetic resonance to assess fossil fuel biodegradation: fate of

- [1-13C]acenaphthene in creosote polycyclic aromatic compound mixtures degraded by bacteria. *Applied and Environmental Microbiology*, 64(4): 1447-1453.
- Selroos, J. O. and Cvetkovic, V., 1994. Mass flux statistics of kinetically sorbing solute in heterogeneous aquifers: Analytical solution and comparison with simulations. *Water Resources Research*, 30(1): 63-69.
- Selroos, J.O., 1995. Temporal moments for nonergodic solute transport in heterogeneous aquifers. *Water Resources Research*, 31(7): 1705-1712.
- Sherwood Lollar, B., Slater, G. F., Sleep, B., Witt, M., Klecka, G. M., Harkness, M. and Spivack, J., 2001. Stable Carbon Isotope Evidence for Intrinsic Bioremediation of Tetrachloroethene and Trichloroethene at Area 6, Dover Air Force Base. *Environmental Sciences and Technology*, 2(35): 261-269.
- Simkins, S. and Alexander, M., 1984. Models for Mineralization Kinetics with the Variables of Substrate Concentration and Population Density. *Applied and Environmental Microbiology*, 47(6): 1299-1306.
- Simmons, C.S., Ginn, T.R. and Wood, B.D., 1995. Stochastic-convective transport with nonlinear reaction: mathematical framework. *Water Resources Research*, 31(11): 2675-2688.
- Slater, G.F., Dempster, H.S., Sherwood Lollar, B. and Ahad, J., 1999. Headspace Analysis: A New Application for Isotopic Characterization of Dissolved Organic Contaminants. *Environmental Sciences and Technology*, 33(1): 190-194.
- Slater, G.F., Sherwood Lollar, B., Sleep, B.E. and Edwards, E.A., 2001. Variability in carbon isotopic fractionation during biodegradation of chlorinated ethenes: implications for field applications. *Environmental Sciences and Technology*, 35(5): 901-907.
- Smith, L. and Freeze, R.A., 1979. Stochastic Analysis of Steady State Groundwater Flow in a Bounded Domain. 1. One-Dimensional Simulations. *Water Resources Research*, 15(3): 521-528.
- Sposito, G., Jury, W.A. and Gupta, V.K., 1986. Fundamental Problems in the Stochastic Convection-Dispersion Model of Solute Transport in Aquifers and Field Soils. *Water Resources Research*, 22(1): 77-88.
- Starke, U., Herbert, M. and Einsele, G., 1991. Polyzyklische aromatische Kohlenwasserstoffe (PAK) in Boden und Grundwasser. In: D. Rosenkranz, G. Einsele and H.-M. Harreß (Editors), *Bodenschutz - Ergänzbares Handbuch der Maßnahmen und Empfehlungen für Schutz, Pflege und Sanierung von Böden, Landschaft und Grundwasser*. Erich Schmidt Verlag, pp. 1680.1-1680.38.
- Steinbach, A., Annweiler, E., Meckenstock, R., Richnow, H.H. and Michaelis, W., 2000. Stabile Isotopen organischer Schadstoffe - Indikatoren für Natural Attenuation. In: G. Kreysa, T. Track, J. Michels and J. Wiesner (Editors), *Natural Attenuation - Neue Erkenntnisse, Konflikte, Anwendungen*. Dechema, Frankfurt.
- Steinbach, A., Annweiler, E. and Michaelis, W., in preparation. Hydrogen and carbon isotope fractionation during anaerobic biodegradation of aromatic hydrocarbons - a field study. *Environmental Sciences and Technology*.
- Sturchio, N. C., Clausen, J. L., Heraty, L. J., Huang, L., Holt, B. D. and Abrajano, T. A., 1998. Chlorine isotope investigation of natural attenuation of trichloroethene in an aerobic aquifer. *Environmental Sciences and Technology*, 32(20): 3037-3042.
- Suna, Y., Petersen, J.N. and Bearc, J., 2001. Successive identification of biodegradation rates for multiple sequentially reactive contaminants in groundwater. *Journal of Contaminant Hydrology*, 51: 83-95.
- Szelinski, B.A., 1999. Natural Attenuation in the Federal Republic of Germany - Background, Trends and Current Situation. In: NATO Special Session Monitored Natural Attenuation. Angers, France, pp. 34-38.
- Teutsch, G., Grathwohl, P. and Schiedek, T., 1997. Literaturstudie zum natürlichen Rückhalt/Abbau von Schadstoffen im Grundwasser. Band 35/97, Landesanstalt für Umweltschutz Baden-Württemberg, Karlsruhe.
- Teutsch, G. and Rügner, H., 1999. Quantifizierung von Natural Attenuation im Feldmaßstab - Möglichkeiten und Grenzen. In: G. Kreysa, T. Track, J. Michels and J. Wiesner (Editors), *Natural Attenuation - Möglichkeiten und Grenzen naturnaher Sanierungsstrategien*. Dechema, Frankfurt, pp. 43-58.
- Teutsch, G., Ptak, T., Schwarz, R. and Holder, T., 2000. Ein neues integrales Verfahren zur Quantifizierung der Grundwasserimmission, Teil I: Beschreibung der Grundlagen. *Grundwasser*, 4: 170-175.

- Teutsch, G., Rügner, H., Grathwohl, P. and Kohler, W., 2001. Entwicklung von Bewertungskriterien natürlicher Schadstoffabbauprozesse in Grundwasserleitern als Grundlage für Sanierungsentscheidungen bei Altstandorten. Landesanstalt für Umweltschutz Baden-Württemberg Karlsruhe und Zentrum für Angewandte Geologie der Universität Tübingen.
- Thoenes, H.W., 1999. Thesen zum Symposium Natural Attenuation 27./28.10.1999. In: G. Kreysa, T. Track, J. Michels and J. Wiesner (Editors), Natural Attenuation - Möglichkeiten und Grenzen naturnaher Sanierungsstrategien. Dechema, Frankfurt, pp. 19-21.
- Thornton, S.F., Bright, M.I., Lerner, D.N. and Tellam, J.H., 2000. Attenuation of landfill leachate by UK Triassic sandstone aquifer materials. 2. Sorption and degradation of organic pollutants in laboratory columns. *Journal of Contaminant Hydrology*, 43: 355-383.
- Track, T. and Michels, J., 1999. Resümee des 1. Symposiums "Natural Attenuation" - Möglichkeiten und Grenzen naturnaher Sanierungsstrategien. In: G. Kreysa, T. Track, J. Michels and J. Wiesner (Editors), Natural Attenuation - Möglichkeiten und Grenzen naturnaher Sanierungsstrategien. Dechema, Frankfurt, pp. 3-15.
- Troisi, S., Fallico, C., Straface, S. and Migliari, E., 2000. Application of kriging with external drift to estimate hydraulic conductivity from electrical-resistivity data in unconsolidated deposits near Montalto Uffugo, Italy. *Hydrogeology Journal*, 8(4): 356-367.
- Ufrecht, W. and Harlacher, C., 1998. Hydrogeologisches System-Modell Stuttgart. Amt für Umweltschutz, Stuttgart.
- Ufrecht, W., 1999. Geologie und Hydrogeologie des Neckartals zwischen Stuttgart-Münster und Stuttgart-Untertürkheim. Schriftenreihe des Amtes für Umweltschutz, Stuttgart, 4: 10-30.
- US EPA, 1999. Use of Monitored Natural Attenuation at Superfund, RCRA Corrective Action, and Underground Storage Tank Sites. Report 9200.4-17P, U.S. EPA - Office of Solid Waste and Emergency Response, Washington.
- Valocchi, A.J., 1985. Validity of the local equilibrium assumption for modeling sorbing solute transport through homogeneous soils. *Water Resources Research*, 21: 808-820.
- Vanderborght, J. and Vereecken, H., 2001. Analyses of locally measured bromide breakthrough curves from a natural gradient tracer experiment at Krauthausen. *Journal of Contaminant Hydrology*, 41(1-2): 23-43.
- Vassolo, S., Kinzelbach, W. and Schäfer, W., 1998. Determination of a well head protection zone by stochastic inverse modelling. *Journal of Hydrology*, 206(3-4): 268-280.
- Vereecken, H., Doering, U., Hardelauf, H., Jaekel, U., Hashagen, U., Neuendorf, O., Schwarze, H. and Seidemann, R., 2000. Analysis of solute transport in a heterogeneous aquifer; the Krauthausen field experiment. *Journal of Contaminant Hydrology*, 45(3-4): 329-358.
- Verschueren, K., 1983. Handbook of environmental data on organic chemicals. Van Nostrand Reinhold Company, New York, 1310 pp.
- Vert, M., Ptak, T., Biver, P. and Vittori, J., 1998. Geostatistical generation of three-dimensional aquifer realizations using the conditional SIS approach with direction trends imposed on variogram models. In: J. Gómez-Hernández and A. Soares (Editors), geoENV II - Geostatistics for environmental applications. Quantitative Geology and Geostatistics. Kluwer Academic Publishers, Valencia, pp. 343-356.
- Vieth, A., Kästner, M., Morasch, B., Meckenstock, R. and Richnow, H.H., 2001. Charakterisierung des biologischen Abbaus von BTEX im Grundwasser über Isotopenfraktionierung - Feldstudien. TerraTech, 5: 37-41.
- Wagner, S., Häfner, F., Boy, S. and Behr, A., 1999. Calibration and sensitivity analysis of the 3-D Cape Cod tracer test. In: F. Stauffer, W. Kinzelbach, K. Kovar and E. Hoehn (Editors), ModelCARE '99: Calibration and Reliability in Groundwater Modelling: Coping with Uncertainty. IAHS Publication 265, pp. 250-255.
- Wang, F. and Anderson, M., 1982. Introduction to Groundwater Modeling - Finite Difference and Finite Element Methods. Freeman and Company, San Francisco, 237 pp.
- Ward, J. A. M., Ahad, J. M. E., Lacrampe-Couloume, G., Slater, G. F., Edwards, E. A. and Sherwood Lollar, B., 2000. Hydrogen isotope fractionation during methanogenic degradation of toluene: potential for direct verification of bioremediation. *Environmental Sciences and Technology*, 34(21): 4577-4581.

- Weber, K., Eiswirth, M., Hötzl, H. and Reichert, B., 1999. Volatilisation von BTEX aus dem Grundwasser. In: G. Kreysa, T. Track, J. Michels and J. Wiesner (Editors), Natural Attenuation - Möglichkeiten und Grenzen naturnaher Sanierungsstrategien. Dechema, Frankfurt, pp. 236-237.
- Wiedemeier, T.H., Rifai, H.S., Newell, C.J. and Wilson, J.T., 1999. Natural Attenuation of Fuels and Chlorinated Solvents in the Subsurface. John Wiley and Sons, New York, 617 pp.
- Wu, S. and Gschwend, P.M., 1986. Sorption kinetics of hydrophobic organic compounds to natural sediments and soils. Environmental Sciences and Technology, 20: 717-725.
- Zamfirescu, D. and Grathwohl, P., 1998. Schadstoffemission durch Desorption und Lösung standortspezifischer organischer Verbindungen im Schadenszentrum, Testfeld Süd. Grundwasser, 4(3): 167-174.
- Zamfirescu, D., 2000. Release and Fate of Specific Organic Contaminants at a Former Gasworks Site. Tübinger Geowissenschaftliche Arbeiten (TGA), C53, 96 pp.
- Zechner, E., Genereux, D. and Saiers, J., 1999. The benefit of using data on canal seepage and tracer concentration in aquifer parameter estimation. In: F. Stauffer, W. Kinzelbach, K. Kovar and E. Hoehn (Editors), ModelCARE '99: Calibration and Reliability in Groundwater Modelling: Coping with Uncertainty. IAHS Publication 265, pp. 256-262.
- Zeyer, J., Kuhn, E.P. and Schwarzenbach, R.P., 1986. Rapid microbial mineralization of toluene and 1,3-dimethylbenzene in the absence of molecular oxygen. Applied and Environmental Microbiology, 52(4): 944-947.
- Zhang, Y.-K., Zhang, D. and Lin, J., 1996. Nonergodic solute transport in three-dimensional heterogeneous isotropic aquifers. Water Resources Research, 32(9): 2955-2963.
- Zhang, Y.-K., 1997. On the variance of second spatial moments of a ergodic plume in heterogeneous aquifers. Water Resources Research, 33(8): 1893-1900.
- Zheng, C., 1990. MT3D - A modular three-dimensional transport model for simulation of advection, dispersion and chemical reaction of contaminants in groundwater systems. - Program documentation. S.S. Papadopoulos & Associates, Inc.
- Zheng, C. and Wang, P.P., 1998. MT3DMS - A modular three-dimensional multispecies transport model for simulation of advection, dispersion and chemical reaction of contaminants in groundwater systems. - Documentation and User's Guide. Waterloo Hydrogeologic.
- Zhu, C. and Burden, D.S., 2001. Mineralogical compositions of aquifer matrix as necessary initial conditions in reactive contaminant transport models. Journal of Contaminant Hydrology, 51: 145-161.

Appendix

A.1 Standard parameters of pumping tests from March 2001

A.1.1 Standard parameters during pumping test at B47

A.1.2 Standard parameters during pumping test at B85

A.2 Chemical analysis of pumping tests from March 2001

A.2.1 Concentrations of BTEX compounds

A.2.2 Concentrations of PAH compounds

A.2.3 Concentrations of Ions

A.3 Isotope analysis of pumping tests from March 2001 (University of Hamburg)

A.3.1 Isotope ratios of BTEX compounds in $\delta^{13}\text{C}$ -notation

A.3.2 Isotope ratios of PAH compounds in $\delta^{13}\text{C}$ -notation

A.1 Standard parameters of pumping tests from March 2001

A.1.1 Standard parameters during pumping test at B47

Date / Time	Total elapsed time [h]	O ₂ [mg L ⁻¹]	Electrical conductivity [μS cm ⁻¹]	Temperature [°C]	pH [-]	Eh [mV]
12.03.01 10:09	0.2	0.31	1721.68	14.66	7.16	-322.27
12.03.01 11:03	1.1	0.09	1698.73	14.58	7.13	-324.22
12.03.01 12:04	2.1	0.03	1744.14	14.61	7.12	-335.94
12.03.01 13:02	3.0	0.04	1765.63	14.61	7.11	-334.47
12.03.01 14:01	4.0	0.04	1783.20	14.65	7.11	-336.91
12.03.01 15:00	5.0	0.09	1750.00	14.59	7.11	-309.57
12.03.01 15:59	6.0	0.12	1800.78	14.61	7.11	-317.87
12.03.01 17:00	7.0	0.29	1816.41	14.64	7.08	-350.10
12.03.01 17:59	8.0	0.06	1827.15	14.62	7.11	-328.61
12.03.01 19:00	9.0	0.09	1830.08	14.61	7.11	-320.31
12.03.01 20:00	10.0	0.06	1842.29	14.61	7.11	-329.59
12.03.01 20:59	11.0	0.06	1850.59	14.61	7.11	-335.94
12.03.01 21:59	12.0	0.04	1855.96	14.60	7.11	-336.91
12.03.01 22:59	13.0	0.06	1860.84	14.59	7.07	-350.59
12.03.01 23:59	14.0	0.07	1859.86	14.56	7.10	-323.24
13.03.01 00:59	15.0	0.22	1865.23	14.49	7.09	-337.89
13.03.01 01:59	16.0	0.19	1870.12	14.51	7.10	-338.38
13.03.01 02:59	17.0	0.04	1875.98	14.58	7.10	-340.33
13.03.01 03:59	18.0	0.04	1876.46	14.55	7.10	-341.31
13.03.01 05:04	19.1	0.04	1882.32	14.59	7.10	-334.47
13.03.01 06:00	20.0	0.04	1885.74	14.56	7.10	-339.36
13.03.01 07:01	21.0	0.06	1888.18	14.55	7.10	-335.94
13.03.01 08:00	22.0	0.06	1892.58	14.55	7.11	-338.38
13.03.01 09:01	23.0	0.06	1894.53	14.59	7.10	-339.36
13.03.01 10:00	24.0	0.06	1897.95	14.61	7.10	-340.82
13.03.01 11:01	25.0	0.06	1900.39	14.59	7.10	-338.87
13.03.01 12:00	26.0	0.06	1903.32	14.67	7.10	-344.24
13.03.01 13:01	27.0	0.06	1905.27	14.70	7.10	-336.91
13.03.01 14:00	28.0	0.07	1907.23	14.67	7.10	-332.03
13.03.01 15:01	29.0	0.06	1910.64	14.70	7.10	-343.26
13.03.01 16:00	30.0	0.06	1912.60	14.69	7.10	-342.29
13.03.01 17:01	31.0	0.06	1914.06	14.64	7.10	-343.26
13.03.01 18:00	32.0	0.06	1915.53	14.62	7.10	-340.33
13.03.01 19:01	33.0	0.07	1917.48	14.65	7.10	-340.33
13.03.01 20:00	34.0	0.06	1919.92	14.62	7.10	-339.36
13.03.01 21:01	35.0	0.04	1919.43	14.60	7.10	-340.33
13.03.01 22:00	36.0	0.06	1922.36	14.60	7.10	-339.84
13.03.01 22:43	36.7	0.07	1923.34	14.61	7.10	-340.33

A.1.2 Standard parameters during pumping test at B85

Date / Time	Total elapsed time [h]	O ₂ [mg L ⁻¹]	Electrical conductivity [μS cm ⁻¹]	Temperature [°C]	pH [-]	Eh [mV]
08.03.01 10:08	0.1	0.81	1775.88	14.31	7.01	-170.41
08.03.01 11:01	1.0	0.12	1788.09	14.54	7.01	-191.41
08.03.01 12:00	2.0	0.09	1800.78	14.61	7.02	-199.71
08.03.01 13:00	2.9	0.41	1808.11	14.56	7.02	-223.63
08.03.01 14:07	4.1	0.10	1825.68	14.73	7.02	-208.50
08.03.01 15:03	5.0	0.07	1836.43	14.75	7.02	-207.52
08.03.01 15:59	5.9	0.07	1844.73	14.75	7.01	-209.96
08.03.01 16:55	6.9	0.06	1854.00	14.76	7.02	-216.31
08.03.01 18:10	8.1	0.07	1862.79	14.77	7.02	-217.77
08.03.01 19:06	9.1	0.06	1870.12	14.77	7.02	-225.59
08.03.01 20:02	10.0	0.07	1875.49	14.78	7.02	-231.45
08.03.01 20:58	10.9	0.06	1881.84	14.79	7.03	-239.75
08.03.01 21:54	11.9	0.04	1886.23	14.75	7.01	-247.56
08.03.01 23:09	13.1	0.07	1893.55	14.79	7.03	-254.39
09.03.01 00:05	14.0	0.07	1897.46	14.77	7.02	-253.91
09.03.01 01:01	15.0	0.04	1901.37	14.77	7.02	-259.28
09.03.01 01:57	15.9	0.04	1906.74	14.36	7.02	-264.16
09.03.01 02:53	16.8	0.04	1911.13	14.78	7.02	-271.48
09.03.01 04:08	18.1	0.03	1915.53	14.78	7.01	-267.58
09.03.01 05:04	19.0	0.04	1919.43	14.78	7.02	-268.55
09.03.01 06:00	20.0	0.04	1921.88	14.78	7.01	-276.37
09.03.01 06:56	20.9	0.04	1924.32	14.78	7.01	-259.28
09.03.01 07:52	21.8	0.04	1928.71	14.78	7.01	-260.74
09.03.01 09:07	23.1	0.06	1933.59	14.78	7.01	-255.86
09.03.01 10:04	24.0	0.06	1936.04	14.81	7.02	-254.39
09.03.01 11:00	24.9	0.07	1938.48	14.84	7.02	-256.35
09.03.01 11:56	25.9	0.06	1941.41	14.89	7.02	-258.30
09.03.01 12:52	26.8	0.07	1943.85	14.90	7.01	-257.32
09.03.01 14:07	28.1	0.06	1947.75	14.90	7.01	-262.70
09.03.01 15:03	29.0	0.06	1950.68	14.90	7.01	-259.28
09.03.01 15:59	29.9	0.06	1952.64	14.90	7.02	-264.16
09.03.01 16:53	30.8	0.67	1953.61	14.89	7.02	-270.02
09.03.01 18:08	32.1	0.06	1957.03	14.88	7.01	-269.53
09.03.01 19:04	33.0	0.04	1957.52	14.86	7.01	-272.95
09.03.01 20:01	34.0	0.04	1959.96	14.87	7.01	-275.39
09.03.01 20:57	34.9	0.06	1962.89	14.87	7.01	-274.41
09.03.01 21:53	35.8	0.06	1963.87	14.86	7.01	-275.39
09.03.01 22:49	36.8	0.06	1965.82	14.82	7.01	-266.11

A.2 Chemical analysis of pumping tests from March 2001

A.2.1 Concentrations of BTEX compounds in $\mu\text{g L}^{-1}$

Date / Time	Sample number	Benzene	Toluene	Et-B	m,p-X	o-X	iso-PB	PB
12.03.01 10:10	B47-1	961.73	4.42	664.23	78.97	< 0.02	106.77	30.63
12.03.01 10:30	B47-2	963.35	4.25	n.d.	n.d.	4.96	183.85	31.06
12.03.01 11:50	B47-3	1066.89	3.92	623.79	17.00	12.82	113.04	27.03
12.03.01 14:05	B47-4	1202.31	9.89	680.71	47.39	2.04	140.47	25.16
12.03.01 17:15	B47-5	1126.69	21.06	595.18	79.52	18.70	149.41	22.86
12.03.01 21:18	B47-6	1034.75	53.52	480.63	132.81	5.13	104.98	21.02
13.03.01 00:30	B47-7	1157.57	80.08	508.18	103.95	32.60	86.69	20.96
13.03.01 08:15	B47-8	914.77	139.19	494.52	180.67	38.64	82.06	17.51
13.03.01 15:00	B47-9	935.02	172.40	320.20	286.61	41.82	72.59	23.33
13.03.01 22:15	B47-10	1115.96	256.44	480.06	301.59	78.18	146.10	15.97
08.03.01 10:07	B85-1	275.40	0.54	2.39	0.73	0.93	14.90	4.82
08.03.01 10:30	B85-2	197.22	0.38	1.97	0.59	0.77	11.50	4.80
08.03.01 11:50	B85-3	176.13	0.31	2.71	0.55	0.61	8.78	3.29
08.03.01 14:05	B85-4	119.28	0.30	4.20	0.77	0.43	10.32	2.37
08.03.01 17:15	B85-5	91.02	0.44	3.66	0.99	0.36	8.51	1.82
08.03.01 21:30	B85-6	76.12	0.69	3.63	1.40	0.40	7.22	1.62
09.03.01 00:07	B85-7	69.17	0.87	3.95	1.74	0.46	6.79	1.45
09.03.01 08:18	B85-8	68.84	1.37	5.08	2.61	0.65	6.28	1.21
09.03.01 15:10	B85-9	59.38	1.49	5.36	2.84	0.63	5.40	1.21
09.03.01 22:45	B85-10	55.28	1.65	6.06	3.23	0.66	5.03	1.20

Date / Time	Sample number	1,3,5-TMB	1,2,4-TMB	BF	1,2,3-TMB	Ina	Ine
12.03.01 10:10	B47-1	0.19	< 0.02	0.20	44.69	11.27	135.41
12.03.01 10:30	B47-2	0.27	< 0.02	0.22	42.48	10.84	103.93
12.03.01 11:50	B47-3	0.42	< 0.02	0.10	32.82	9.82	73.37
12.03.01 14:05	B47-4	0.91	< 0.02	1.48	30.08	14.43	66.69
12.03.01 17:15	B47-5	1.34	< 0.02	4.50	27.19	18.94	77.83
12.03.01 21:18	B47-6	2.22	4.93	12.60	26.20	24.41	106.51
13.03.01 00:30	B47-7	2.98	11.28	19.52	27.00	31.88	144.06
13.03.01 08:15	B47-8	5.57	22.88	39.85	27.78	40.53	240.98
13.03.01 15:00	B47-9	8.33	38.21	45.42	29.74	48.00	303.07
13.03.01 22:15	B47-10	10.57	43.97	67.94	31.13	53.53	365.91
08.03.01 10:07	B85-1	0.10	< 0.02	< 0.02	0.35	< 0.02	0.23
08.03.01 10:30	B85-2	0.10	< 0.02	< 0.02	0.34	< 0.02	0.21
08.03.01 11:50	B85-3	0.10	< 0.02	< 0.02	0.33	< 0.02	0.22
08.03.01 14:05	B85-4	0.09	0.19	0.10	0.39	0.27	0.40
08.03.01 17:15	B85-5	0.10	0.18	0.12	0.31	0.82	1.46
08.03.01 21:30	B85-6	0.12	0.24	0.13	0.30	1.21	3.39
09.03.01 00:07	B85-7	0.15	0.35	0.16	0.30	1.41	4.76
09.03.01 08:18	B85-8	0.19	0.41	0.21	0.35	2.21	9.58
09.03.01 15:10	B85-9	0.22	0.24	0.25	0.34	2.27	10.65
09.03.01 22:45	B85-10	0.31	0.29	0.29	0.39	2.49	12.23

n.d.: not determined

A.2.2 Concentrations of PAH compounds in $\mu\text{g L}^{-1}$

Date / Time	Sample number	Nap	1-Me-Nap	2-Me-Nap	Any	Ace	Fln	Phe	Ant	Fth
12.03.01 10:10	B47-1	2.98	0.24	22.37	2.49	308.27	59.09	20.52	0.93	0.44
12.03.01 10:30	B47-2	2.75	0.24	21.23	3.00	306.62	57.82	19.77	0.89	0.45
12.03.01 11:50	B47-3	5.17	0.30	26.00	5.93	413.73	83.32	25.65	1.39	0.56
12.03.01 14:05	B47-4	15.85	0.61	34.77	5.63	425.49	86.38	23.51	1.32	0.54
12.03.01 17:15	B47-5	38.86	1.53	42.25	6.30	441.71	98.01	23.77	1.41	0.57
12.03.01 21:18	B47-6	81.66	4.22	48.78	7.95	445.28	103.24	22.80	1.47	0.53
13.03.01 00:30	B47-7	112.98	6.61	50.95	7.52	424.40	97.80	20.84	1.38	0.47
13.03.01 08:15	B47-8	239.31	17.30	65.29	8.10	456.19	111.88	22.67	1.51	0.53
13.03.01 15:00	B47-9	294.17	22.35	71.42	7.89	442.32	107.99	21.37	1.46	0.49
13.03.01 22:15	B47-10	326.01	25.22	65.22	7.06	369.65	91.20	17.87	1.29	0.41
08.03.01 10:07	B85-1	0.21	0.09	0.57	2.57	200.57	7.07	0.30	0.34	0.12
08.03.01 10:30	B85-2	0.17	0.09	0.58	2.64	211.68	6.82	0.26	0.36	0.12
08.03.01 11:50	B85-3	0.16	0.07	0.57	2.65	220.00	5.95	0.24	0.37	0.12
08.03.01 14:05	B85-4	0.65	0.08	0.59	2.78	234.05	4.85	0.24	0.39	0.13
08.03.01 17:15	B85-5	1.52	0.06	0.51	2.48	211.02	3.59	0.20	0.35	0.11
08.03.01 21:30	B85-6	1.64	0.03	0.25	1.20	102.08	1.49	0.11	0.16	0.07
09.03.01 00:07	B85-7	1.92	0.02	0.21	1.00	84.51	1.11	0.09	0.13	0.05
09.03.01 08:18	B85-8	8.44	0.05	0.62	2.93	238.37	2.63	0.23	0.36	0.12
09.03.01 15:10	B85-9	10.27	0.06	0.64	2.88	233.63	2.32	0.19	0.35	0.11
09.03.01 22:45	B85-10	11.93	0.06	0.67	3.00	239.93	2.22	0.21	0.35	0.12

Date / Time	Sample number	Py	BaA	Chr	Bbf-BkF	BaP	Indeno	DahA	BghiP
12.03.01 10:10	B47-1	0.13	< 0.025	< 0.025	< 0.025	< 0.025	< 0.025	< 0.025	< 0.025
12.03.01 10:30	B47-2	0.13	< 0.025	< 0.025	< 0.025	< 0.025	< 0.025	< 0.025	< 0.025
12.03.01 11:50	B47-3	0.17	< 0.025	< 0.025	< 0.025	< 0.025	< 0.025	< 0.025	< 0.025
12.03.01 14:05	B47-4	0.16	< 0.025	< 0.025	< 0.025	< 0.025	< 0.025	< 0.025	< 0.025
12.03.01 17:15	B47-5	0.17	< 0.025	< 0.025	< 0.025	< 0.025	< 0.025	< 0.025	< 0.025
12.03.01 21:18	B47-6	0.16	< 0.025	< 0.025	< 0.025	< 0.025	< 0.025	< 0.025	< 0.025
13.03.01 00:30	B47-7	0.14	< 0.025	< 0.025	< 0.025	< 0.025	< 0.025	< 0.025	< 0.025
13.03.01 08:15	B47-8	0.16	< 0.025	< 0.025	< 0.025	< 0.025	< 0.025	< 0.025	< 0.025
13.03.01 15:00	B47-9	0.15	< 0.025	< 0.025	< 0.025	< 0.025	< 0.025	< 0.025	< 0.025
13.03.01 22:15	B47-10	0.12	< 0.025	< 0.025	< 0.025	< 0.025	< 0.025	< 0.025	< 0.025
08.03.01 10:07	B85-1	0.05	< 0.025	< 0.025	< 0.025	< 0.025	< 0.025	< 0.025	< 0.025
08.03.01 10:30	B85-2	0.05	< 0.025	< 0.025	< 0.025	< 0.025	< 0.025	< 0.025	< 0.025
08.03.01 11:50	B85-3	0.05	< 0.025	< 0.025	< 0.025	< 0.025	< 0.025	< 0.025	< 0.025
08.03.01 14:05	B85-4	0.05	< 0.025	< 0.025	< 0.025	< 0.025	< 0.025	< 0.025	< 0.025
08.03.01 17:15	B85-5	0.04	< 0.025	< 0.025	< 0.025	< 0.025	< 0.025	< 0.025	< 0.025
08.03.01 21:30	B85-6	< 0.025	< 0.025	< 0.025	< 0.025	< 0.025	< 0.025	< 0.025	< 0.025
09.03.01 00:07	B85-7	< 0.025	< 0.025	< 0.025	< 0.025	< 0.025	< 0.025	< 0.025	< 0.025
09.03.01 08:18	B85-8	0.05	< 0.025	< 0.025	< 0.025	< 0.025	< 0.025	< 0.025	< 0.025
09.03.01 15:10	B85-9	0.05	< 0.025	< 0.025	< 0.025	< 0.025	< 0.025	< 0.025	< 0.025
09.03.01 22:45	B85-10	0.05	< 0.025	< 0.025	< 0.025	< 0.025	< 0.025	< 0.025	< 0.025

A.2.3 Concentrations of Ions in mg L⁻¹

Date / Time	Sample number	F ⁻ [mg/l]	Cl ⁻ [mg/l]	NO ₂ ⁻ [mg/l]	Br ⁻ [mg/l]	NO ₃ ⁻ [mg/l]	PO ₄ ³⁻ [mg/l]	SO ₄ ²⁻ [mg/l]
12.03.01 10:10	B47-1	0.82	105.03	b.d.	b.d.	b.d.	b.d.	135.70
12.03.01 10:30	B47-2	0.78	100.28	b.d.	b.d.	b.d.	b.d.	123.54
12.03.01 11:50	B47-3	0.75	103.48	b.d.	b.d.	b.d.	b.d.	131.07
12.03.01 14:05	B47-4	0.79	108.66	b.d.	b.d.	b.d.	b.d.	163.45
12.03.01 17:15	B47-5	0.75	112.48	b.d.	b.d.	b.d.	b.d.	193.70
12.03.01 21:18	B47-6	0.76	114.09	b.d.	b.d.	b.d.	b.d.	215.96
13.03.01 00:30	B47-7	0.88	114.58	b.d.	b.d.	b.d.	b.d.	227.57
13.03.01 08:15	B47-8	0.79	116.85	b.d.	b.d.	b.d.	b.d.	254.04
13.03.01 15:00	B47-9	0.75	119.11	b.d.	b.d.	b.d.	b.d.	272.02
13.03.01 22:15	B47-10	0.77	119.11	b.d.	b.d.	b.d.	b.d.	284.64
08.03.01 10:07	B85-1	0.95	97.95	1.46	b.d.	b.d.	b.d.	255.90
08.03.01 10:30	B85-2	0.66	105.14	b.d.	b.d.	b.d.	b.d.	232.98
08.03.01 11:50	B85-3	0.73	101.48	b.d.	b.d.	b.d.	b.d.	240.74
08.03.01 14:05	B85-4	0.76	113.09	b.d.	b.d.	0.31	b.d.	257.18
08.03.01 17:15	B85-5	0.71	105.94	b.d.	b.d.	0.94	b.d.	278.52
08.03.01 21:30	B85-6	0.74	117.02	b.d.	b.d.	b.d.	b.d.	294.06
09.03.01 00:07	B85-7	0.79	118.68	b.d.	b.d.	b.d.	b.d.	307.69
09.03.01 08:18	B85-8	0.07	120.32	b.d.	b.d.	b.d.	b.d.	338.55
09.03.01 15:10	B85-9	0.85	121.28	b.d.	b.d.	0.43	b.d.	354.06
09.03.01 22:45	B85-10	0.74	120.66	b.d.	b.d.	b.d.	b.d.	361.85

Date / Time	Sample number	Na ⁺ [mg/l]	K ⁺ [mg/l]	Mg ²⁺ [mg/l]	Ca ²⁺ [mg/l]	NH ₄ ⁺ [mg/l]	Fe ²⁺ [mg/l]	Mn ²⁺ [mg/l]	TIC [mg/l]	TOC [mg/l]
12.03.01 10:10	B47-1	54.14	10.12	61.62	251.95	b.d.	0.525	0.19	129.97	6.79
12.03.01 10:30	B47-2	53.02	9.59	60.75	244.63	b.d.	0.449	0.20	126.06	4.73
12.03.01 11:50	B47-3	55.29	9.94	66.48	261.61	b.d.	0.359	0.19	130.18	4.64
12.03.01 14:05	B47-4	57.58	10.32	69.61	268.34	b.d.	0.317	0.20	131.54	4.71
12.03.01 17:15	B47-5	59.39	10.78	73.14	280.79	b.d.	0.322	0.11	122.14	4.86
12.03.01 21:18	B47-6	59.34	10.41	73.55	282.85	b.d.	0.324	0.14	121.86	4.69
13.03.01 00:30	B47-7	59.17	9.78	73.93	281.30	b.d.	0.339	0.15	121.06	4.47
13.03.01 08:15	B47-8	59.78	10.14	75.40	289.67	b.d.	0.406	0.16	124.22	4.32
13.03.01 15:00	B47-9	60.73	10.70	77.73	297.49	b.d.	0.453	0.10	122.60	4.61
13.03.01 22:15	B47-10	60.62	10.09	77.99	293.71	2.80	0.515	0.10	122.49	5.05
08.03.01 10:07	B85-1	56.55	13.76	20.37	293.57	b.d.	1.072	0.17	105.31	4.25
08.03.01 10:30	B85-2	51.88	8.01	32.00	198.92	b.d.	1.136	0.17	98.71	2.91
08.03.01 11:50	B85-3	52.95	8.28	41.88	268.95	b.d.	1.260	0.17	99.88	2.79
08.03.01 14:05	B85-4	55.12	8.54	47.52	270.23	b.d.	1.344	0.21	99.25	2.67
08.03.01 17:15	B85-5	56.27	8.91	51.14	273.64	b.d.	1.475	0.17	101.12	2.72
08.03.01 21:30	B85-6	59.95	9.73	57.45	290.99	b.d.	1.624	0.11	100.28	2.40
09.03.01 00:07	B85-7	60.83	10.22	60.77	296.95	b.d.	1.726	0.12	104.78	2.70
09.03.01 08:18	B85-8	61.71	9.53	64.73	303.99	b.d.	1.925	0.10	89.68	2.36
09.03.01 15:10	B85-9	62.49	10.27	65.72	303.68	b.d.	2.100	0.10	91.20	2.47
09.03.01 22:45	B85-10	62.00	9.63	67.17	304.66	2.20	2.232	0.12	80.10	2.59

b.d.: below detection limit

A.3 Isotope analysis of pumping tests from March 2001 (University of Hamburg)

A.3.1 Isotope ratios of BTEX compounds in $\delta^{13}\text{C}$ -notation [%]

Date / Time	Sample number	Benzene		Toluene		Et-B		m,p-X		o-X	
		$\delta^{13}\text{C}$	St.dev.								
12.03.01 10:10	B47-1	-24.94	1.26	b.d.	b.d.	-24.39	0.43	-8.43	1.79	-13.76	0.39
12.03.01 10:30	B47-2	-23.61	0.14	b.d.	b.d.	-24.31	0.33	-10.14	1.15	-13.79	0.78
12.03.01 11:50	B47-3	-24.38	0.77	b.d.	b.d.	-25.02	0.46	-7.21	2.26	-14.77	0.27
12.03.01 14:05	B47-4	-24.37	0.59	b.d.	b.d.	-25.03	0.67	-9.04	1.84	-15.84	0.83
12.03.01 17:15	B47-5	-23.76	0.58	-19.43	1.53	-24.30	1.02	-14.56	0.67	-17.62	0.93
12.03.01 21:18	B47-6	-23.70	0.42	-21.93	1.02	-23.46	0.88	-18.26	2.21	-18.59	0.89
13.03.01 00:30	B47-7	-23.86	1.00	-23.44	1.09	-23.84	0.79	-18.83	1.57	-19.50	0.34
13.03.01 08:15	B47-8	-23.97	1.22	-23.55	1.01	-24.45	0.90	-20.12	1.81	-21.49	0.92
13.03.01 15:00	B47-9	-23.98	1.26	-23.52	1.42	-24.25	1.12	-19.84	1.81	-21.09	0.71
13.03.01 22:15	B47-10	-23.39	0.32	-23.94	0.86	-24.96	0.54	-20.56	0.75	-21.93	0.60
08.03.01 10:07	B85-1	-20.95	0.53	b.d.	b.d.	-19.22	5.50	-16.37	0.79	-8.99	0.38
08.03.01 10:30	B85-2	-20.46	0.33	b.d.	b.d.	-14.41	1.79	-14.27	1.26	-9.75	1.51
08.03.01 11:50	B85-3	-20.74	0.34	b.d.	b.d.	-16.80	0.34	-16.10	0.68	-9.28	1.86
08.03.01 14:05	B85-4	-21.30	0.48	b.d.	b.d.	-18.87	2.58	-17.55	0.90	-7.04	0.59
08.03.01 17:15	B85-5	-20.52	0.96	b.d.	b.d.	-19.93	2.75	-16.79	0.50	-11.23	1.09
08.03.01 21:30	B85-6	-21.15	0.33	b.d.	b.d.	-20.28	2.56	-18.44	0.18	-13.65	0.50
09.03.01 00:07	B85-7	-20.19	0.35	b.d.	b.d.	-23.61	1.34	-19.28	1.17	-12.47	0.95
09.03.01 08:18	B85-8	-20.50	0.43	b.d.	b.d.	-21.01	2.61	-20.41	1.20	-14.30	1.76
09.03.01 15:10	B85-9	-21.76	0.87	b.d.	b.d.	-21.49	2.51	-21.40	1.15	-13.17	2.15
09.03.01 22:45	B85-10	-20.67	0.56	b.d.	b.d.	-20.99	1.72	-20.52	1.36	-21.56	1.02

Date / Time	Sample number	iso-PB		PB		Ina		Ine	
		$\delta^{13}\text{C}$	St.dev.	$\delta^{13}\text{C}$	St.dev.	$\delta^{13}\text{C}$	St.dev.	$\delta^{13}\text{C}$	St.dev.
12.03.01 10:10	B47-1	-22.98	0.24	-23.91	0.42	-19.77	0.79	-18.26	0.39
12.03.01 10:30	B47-2	-23.26	0.70	-23.95	0.42	-19.70	0.77	-17.59	0.28
12.03.01 11:50	B47-3	-23.07	0.42	-23.97	0.49	-19.91	0.48	-17.70	0.31
12.03.01 14:05	B47-4	-23.63	0.37	-24.19	0.41	-20.85	0.52	-17.92	0.57
12.03.01 17:15	B47-5	-23.90	0.66	-24.54	0.43	-22.42	1.37	-18.26	0.61
12.03.01 21:18	B47-6	-22.63	0.14	-23.39	0.28	-21.72	0.26	-20.38	0.43
13.03.01 00:30	B47-7	-23.11	0.37	-23.81	0.33	-22.61	0.34	-22.59	0.85
13.03.01 08:15	B47-8	-22.85	0.38	-23.04	0.45	-23.23	0.84	-21.66	1.13
13.03.01 15:00	B47-9	-22.84	0.82	-23.23	0.77	-23.09	0.80	-21.18	0.28
13.03.01 22:15	B47-10	-23.86	0.94	-24.75	1.08	-25.13	0.75	-23.93	2.18
08.03.01 10:07	B85-1	-22.82	0.99	-22.89	0.54	-20.17	0.84	-24.09	0.74
08.03.01 10:30	B85-2	-21.83	1.01	-21.69	1.06	-19.03	0.43	-23.54	0.01
08.03.01 11:50	B85-3	-22.40	1.56	-21.82	0.87	-19.48	1.32	-24.91	0.00
08.03.01 14:05	B85-4	-21.41	0.20	-20.32	1.05	-19.43	1.02	-24.83	1.64
08.03.01 17:15	B85-5	-23.17	2.70	-20.46	1.15	-20.01	1.94	-22.55	0.66
08.03.01 21:30	B85-6	-23.55	1.40	-20.48	1.06	-20.74	0.88	-21.92	0.73
09.03.01 00:07	B85-7	-21.94	0.52	-21.76	1.62	-21.45	0.77	-20.24	1.57
09.03.01 08:18	B85-8	-21.32	0.41	-19.52	0.83	-21.74	0.32	-21.36	1.25
09.03.01 15:10	B85-9	-22.36	0.84	b.d.	b.d.	-21.22	0.99	-18.77	1.43
09.03.01 22:45	B85-10	-21.58	0.94	-21.54	2.27	-23.14	1.87	-21.25	1.36

St.dev.: Standard deviation

b.d.: below detection limit

A.3.2 Isotope ratios of PAH compounds in $\delta^{13}\text{C}$ -notation [%]

Date / Time	Sample number	Nap		1-Me-Nap		2-Me-Nap	
		$\delta^{13}\text{C}$ [%]	St.dev. [%]	$\delta^{13}\text{C}$ [%]	St.dev. [%]	$\delta^{13}\text{C}$ [%]	St.dev. [%]
12.03.01 10:10	B47-1	b.d.	b.d.	-23.28	0.45	-21.12	0.16
12.03.01 10:30	B47-2	b.d.	b.d.	-22.76	0.49	b.d.	b.d.
12.03.01 11:50	B47-3	b.d.	b.d.	-22.82	0.46	-20.46	0.97
12.03.01 14:05	B47-4	-24.80	1.10	-23.75	0.33	-19.80	1.10
12.03.01 17:15	B47-5	-24.51	1.24	-23.45	0.57	-21.22	1.66
12.03.01 21:18	B47-6	-24.74	0.11	-23.75	0.25	-22.05	0.74
13.03.01 00:30	B47-7	-25.41	0.42	-23.81	0.22	-22.23	0.39
13.03.01 08:15	B47-8	-25.17	0.40	-23.86	0.28	-23.23	0.37
13.03.01 15:00	B47-9	-25.36	0.16	-23.74	0.34	-22.75	0.76
13.03.01 22:15	B47-10	-25.63	0.58	-23.92	0.55	-23.42	1.02
08.03.01 10:07	B85-1	b.d.	b.d.	-23.90	0.30	b.d.	b.d.
08.03.01 10:30	B85-2	b.d.	b.d.	b.d.	b.d.	b.d.	b.d.
08.03.01 11:50	B85-3	b.d.	b.d.	-24.53	0.67	b.d.	b.d.
08.03.01 14:05	B85-4	b.d.	b.d.	-24.00	0.47	b.d.	b.d.
08.03.01 17:15	B85-5	b.d.	b.d.	-24.74	0.26	b.d.	b.d.
08.03.01 21:30	B85-6	-22.71	0.55	-23.97	0.28	b.d.	b.d.
09.03.01 00:07	B85-7	-25.53	0.55	-24.29	0.19	b.d.	b.d.
09.03.01 08:18	B85-8	-24.40	0.41	-23.95	0.60	-20.74	0.35
09.03.01 15:10	B85-9	-23.89	0.42	-24.09	1.03	b.d.	b.d.
09.03.01 22:45	B85-10	-24.40	1.32	-23.60	0.77	-21.79	0.63

Date / Time	Sample number	Ace		Fln		Phe	
		$\delta^{13}\text{C}$ [%]	St.dev. [%]	$\delta^{13}\text{C}$ [%]	St.dev. [%]	$\delta^{13}\text{C}$ [%]	St.dev. [%]
12.03.01 10:10	B47-1	-23.55	0.24	-24.38	0.41	-24.86	0.85
12.03.01 10:30	B47-2	-23.61	0.26	-24.26	0.34	-24.52	0.64
12.03.01 11:50	B47-3	-23.94	0.07	-24.25	0.09	-24.13	1.04
12.03.01 14:05	B47-4	-23.72	1.08	-24.45	0.35	-24.45	0.68
12.03.01 17:15	B47-5	-23.58	0.34	-24.28	0.33	-24.81	0.67
12.03.01 21:18	B47-6	-24.15	0.09	-24.01	0.17	-24.93	0.44
13.03.01 00:30	B47-7	-24.20	0.09	-23.90	0.42	-24.53	0.30
13.03.01 08:15	B47-8	-23.75	0.61	-24.40	0.28	-25.05	1.00
13.03.01 15:00	B47-9	-24.11	0.11	-23.98	0.12	-24.99	0.67
13.03.01 22:15	B47-10	-24.28	0.34	-24.22	0.37	-23.32	0.64
08.03.01 10:07	B85-1	-23.63	0.26	-22.72	0.39	b.d.	b.d.
08.03.01 10:30	B85-2	-23.73	0.07	-21.86	0.59	b.d.	b.d.
08.03.01 11:50	B85-3	b.d.	b.d.	-22.13	0.64	b.d.	b.d.
08.03.01 14:05	B85-4	b.d.	b.d.	-22.29	0.80	b.d.	b.d.
08.03.01 17:15	B85-5	b.d.	b.d.	-22.00	0.33	b.d.	b.d.
08.03.01 21:30	B85-6	b.d.	b.d.	-22.68	0.28	b.d.	b.d.
09.03.01 00:07	B85-7	b.d.	b.d.	-21.74	1.14	b.d.	b.d.
09.03.01 08:18	B85-8	b.d.	b.d.	-22.54	0.94	b.d.	b.d.
09.03.01 15:10	B85-9	b.d.	b.d.	-21.81	0.76	b.d.	b.d.
09.03.01 22:45	B85-10	-23.38	0.38	-23.35	2.00	-24.45	n.d.

St.dev.: Standard deviation

b.d.: below detection limit

n.d.: not determined